

ABSTRACT

Title of Dissertation: ENERGY MANAGEMENT OF A
BATTERY-ULTRACAPACITOR
HYBRID ENERGY STORAGE SYSTEM
IN ELECTRIC VEHICLES

Junyi Shen, Doctor of Philosophy, 2016

Dissertation Directed By: Professor Alireza Khaligh
Department of Electrical and Computer
Engineering

Electric vehicle (EV) batteries tend to have accelerated degradation due to high peak power and harsh charging/discharging cycles during acceleration and deceleration periods, particularly in urban driving conditions. An oversized energy storage system (ESS) can meet the high power demands; however, it suffers from increased size, volume and cost. In order to reduce the overall ESS size and extend battery cycle life, a battery-ultracapacitor (UC) hybrid energy storage system (HESS) has been considered as an alternative solution. In this work, we investigate the

optimized configuration, design, and energy management of a battery-UC HESS. One of the major challenges in a HESS is to design an energy management controller for real-time implementation that can yield good power split performance. We present the methodologies and solutions to this problem in a battery-UC HESS with a DC-DC converter interfacing with the UC and the battery. In particular, a multi-objective optimization problem is formulated to optimize the power split in order to prolong the battery lifetime and to reduce the HESS power losses. This optimization problem is numerically solved for standard drive cycle datasets using Dynamic Programming (DP). Trained using the DP optimal results, an effective real-time implementation of the optimal power split is realized based on Neural Network (NN). This proposed online energy management controller is applied to a midsize EV model with a 360V/34kWh battery pack and a 270V/203Wh UC pack. The proposed online energy management controller effectively splits the load demand with high power efficiency and also effectively reduces the battery peak current. More importantly, a 38V-385Wh battery and a 16V-2.06Wh UC HESS hardware prototype and a real-time experiment platform has been developed. The real-time experiment results have successfully validated the real-time implementation feasibility and effectiveness of the real-time controller design for the battery-UC HESS. A battery State-of-Health (SoH) estimation model is developed as a performance metric to evaluate the battery cycle life extension effect. It is estimated that the proposed online energy management controller can extend the battery cycle life by over 60%.

ENERGY MANAGEMENT OF A BATTERY-ULTRACAPACITOR
HYBRID ENERGY STORAGE SYSTEM IN ELECTRIC VEHICLES

by

Junyi Shen

Dissertation submitted to the Faculty of the Graduate School of the
University of Maryland, College Park, in partial fulfillment
of the requirements for the degree of
Doctor of Philosophy
2016

Advisory Committee:
Professor Alireza Khaligh, Chair/Advisor
Professor Robert Newcomb
Professor Behtash Babadi
Professor Andre Tits
Professor Mark Austin, Dean's Representative

© Copyright by
Junyi Shen
2016

Acknowledgement

I would like to express my sincere gratitude to my Ph.D. advisor Professor Alireza Khaligh for his supervision throughout my research. He introduced me to the most interesting research topics in the field of electric vehicles and energy storage systems. With his insightful supervision, we worked closely together to establish the solid groundwork and basis of the research work that I built on afterwards, which targets to address one of the main challenges in electric vehicle energy storage system development. Professor Khaligh gave me invaluable support, encouragement, technical advices and guidance on this very interesting research topic. Professor Khaligh encouraged discussions, collaborations, internship and multidisciplinary projects to provide more opportunities and resources. This trust, support and the "freedom to create" he provided throughout my Ph.D. studies are very much appreciated.

In addition, I would like to thank Dr. Andre Tits, who helped a lot in my PhD research. I am very grateful to his kindness and all the help and discussions. I would also like to thank my committee members, Dr. Robert Newcomb, Dr. Behtash Babadi, and Dr. Mark Austin for their time and valuable comments. Thank you all for your expert knowledge and grand visions. I feel honored to have you on my dissertation committee.

I would also like to thank the research group of Maryland Power Electronics Laboratory (MPEL) for their discussions, help, support and friendship. I am grateful for all the good times we have shared together throughout the years.

My research work has been sponsored in part through the National Science Foundation award number 1307228 and the Genovation Cars Inc., which are gratefully acknowledged.

Table of Contents

List of Tables	viii
List of Figures	ix
List of Abbreviations	xii
Chapter 1: Introduction to Electric Vehicles and Energy Storage Systems.....	1
1.1 Background.....	1
1.2 EV Definitions.....	2
1.3 EV Configurations.....	2
1.4 EV Characteristics	4
1.5 Challenges in EV Development	4
1.6 EVs on Market.....	5
1.7 Batteries	6
1.7.1 Energy Density.	6
1.7.2 Current Rate (C-rate).....	7
1.7.3 State-of-Charge (SoC).....	7
1.7.4 Depth-of-Discharge (DoD).....	8
1.7.5 Power Density.	8
1.7.6 Lifetime.	8
1.8 Ultracapacitors.....	9
1.8.1 Energy.....	9
1.8.2 Power.....	10
1.8.3 State-of-Art of UC.....	10
1.9 Fuel Cells.....	11
1.10 Hybrid Energy Storage Systems.....	12
1.11 Sizing Problem in HESS	13
1.12 Energy Management Problems.....	14
1.13 Summary and Dissertation Overview.....	15
Chapter 2: Literature Review and State-of-the-Art	18
2.1 HESS Configurations	18

2.2 HESS Sizing Strategies	24
2.3 HESS Energy Management Strategies	27
2.3.1 Rule-Based Energy Management Methods	28
2.3.2 Fuzzy Logic-Based Energy Management Methods.....	30
2.3.3 Global Optimization Based Control Strategy.....	33
2.3.4 Stochastic Dynamic Programming Based Control Strategy.....	36
2.3.5 Model Predictive Control Based Control Strategy	41
2.3.6 Instantaneous Optimization Based Control Strategy.....	44
2.3.7 Neural Networks Based Control Strategy	46
2.4 Summary.....	50
Chapter 3: Optimal Sizing of a Battery-UC Hybrid Energy Storage System for EV applications	52
3.1 HESS Power Split Optimization	53
3.1.1 Problem Formulation for the Power Split Optimization	53
3.1.2 Convex Optimization.....	56
3.2 HESS Sizing Optimization and Analysis	56
3.2.1 Battery-only ESS Sizing Optimization.....	56
3.2.2 Battery-UC HESS Sizing Optimization	59
3.3 Summary.....	64
Chapter 4: A Supervisory Energy Management Control Strategy in a Battery-Ultracapacitor Hybrid Energy Storage System.....	66
4.1 HESS Model.....	67
4.1.1 Battery/UC Model	68
4.1.2 Bi-directional DC-DC Converter Model	69
4.1.3 Power Losses in HESS	75
4.2 HESS Energy Management Problem Formulation.....	78
4.2.1 Objective Functions.....	78
4.2.2 Problem Formulation.....	79
4.2.3 Dynamic Programming	80
4.2.4 DP Implementations and Optimization Results	82

4.2.5 Numerical Results	85
4.3 Real-Time HESS Energy Management.....	87
4.3.1 NN Training Data.....	87
4.3.2 NN Training.....	88
4.3.3 Intelligent Online Energy Management Controller	90
4.3.4 Test Results	91
4.4 Battery State-of-Health Evaluation	92
4.4.1 Battery State-of-Health Estimation Model.....	92
4.4.2 Results and Analysis.....	97
4.5 Summary.....	102
Chapter 5: Experiment Design and Real-Time Controller Implementation for a Battery-Ultracapacitor Hybrid Energy Storage System.....	104
5.1 Modeling and System Integration	105
5.1.1 Battery/UC Characteristics.....	105
5.1.2 Battery/UC Models.....	106
5.1.3 DC-DC Converter Model	108
5.2 Real-Time Simulation Setup	109
5.2.1 Target Computer.....	111
5.2.2 Ethernet Connection Setup between the Host computer and the Target Computer.....	111
5.3 Real-Time Experiment Platform Setup	113
5.4 Battery-UC Hybrid Energy Storage System Hardware Prototype Design ..	115
5.4.1 DC Electronic Load	116
5.4.2 DC-DC Converter Hardware.....	117
5.4.3 DC-DC Converter Control Technique.....	121
5.4.4 Interface between the Real-Time Controller and DC-DC Converter ...	125
5.4.5 Sensor Network and DAQ Configuration	127
5.4.5 Experiment Setup	128
5.5 Experiment Results.....	129
5.6 Summary.....	135

Chapter 6: Conclusions and Future Work.....	136
6.1 Conclusions	136
6.2 Future Work.....	138
Bibliography	141

List of Tables

Table 1.1 Specifications of some of the commercially available EVs in the market as of March 2016.....	5
Table 1.2 Summary of the performance characteristics of UC devices. [20]	10
Table 2.1 A Comparison of HESS topologies.	23
Table 2.2 Characteristics of energy management control strategies.....	49
Table 4.1 Battery and UC cell characteristics.....	69
Table 4.2 Parameters for DC-DC converter.	76
Table 4. 3 Parameter <i>B</i> with respect to current rates [112].....	94
Table 4.4 Bi-directional DC-DC converter operation efficiency in both propulsion mode and regenerative braking mode [%].	99
Table 4.5 Battery SoH estimation after different drive cycles.....	101
Table 4.6 Battery cycle life estimation result.	101
Table 5.1 The battery/UC specifications.	106
Table 5.2 DAQ components.	114
Table 5.3 DC-DC converter specifications.	117
Table 5.4 Power MOSFET specifications.	120
Table 5.5 The experiment test components.	128

List of Figures

Figure 1.1 Typical power architecture of an EV.....	3
Figure 2.1 Different HESS topologies.....	18
Figure 3.1 (a) High energy density battery-only ESS optimal sizing; (b) High power battery-only ESS optimal sizing.	58
Figure 3.2 (a) Values of $J_m(N_{bat}, N_{uc})$ and $f_0(P_{uc})$; (b) Pareto points.....	60
Figure 3.3 (a) EV Range vs. (N_{bat}, N_{uc}) ; (b) Acceleration time vs. (N_{bat}, N_{uc})	62
Figure 3.4 HESS optimal sizing at different range / acceleration time specifications.	63
Figure 3.5 (a) N_{bat} at optimal HESS sizing; (b) N_{uc} at optimal HESS sizing.....	64
Figure 4.1 Bi-directional DC-DC converter in the HESS.....	67
Figure 4.2 The model of (a) battery/UC; (b) inductor; (c) MOSFET; (d) body diode.	68
Figure 4.3 The DC-DC converter operation modes. (a) and (b) are in Boost mode, and (c) and (d) are in Buck mode. (a) S_2 is on and D_1 is off; (b) S_2 is off and D_1 is on; (c) S_1 is on and D_2 is off; (d) S_2 is on and D_2 is on.	70
Figure 4.4 Boost Mode. (a) S_2 is on and D_1 is off; (b) S_2 is off and D_1 is on.....	71
Figure 4.5 Buck Mode. (a) S_1 is on and D_2 is off; (b) S_2 is on and D_2 is on.....	73

Figure 4.6 (a) The efficiency map of the DC-DC converter in Boost mode; (b) the efficiency map of the DC-DC converter in Buck mode.	77
Figure 4.7 The flowchart of DP implementation.	84
Figure 4.8 Optimization results of DP algorithm under UDDS cycle.	86
Figure 4.9 The NN architecture for online energy management controller.	88
Figure 4.10 Performances of NN in output prediction. (a) Train data; (b) Test data.	90
Figure 4.11 Online energy management results vs. offline DP optimization results.	91
Figure 4.12 ΔSoH_{rate} as a function of battery current rate.	96
Figure 4.13 Normalized objective function value evaluated under different methodologies for four different drive cycles.	99
Figure 4.14 Battery peak current value $ I_b $ under different drive cycles [A].	100
Figure 5.1 The semi-active topology of the battery-UC HESS.	105
Figure 5.2 (a) Battery equivalent circuit model; (b) Battery discharge curve under 0.5C current rate.	107
Figure 5.3 UC equivalent circuit model.	108
Figure 5.4 DC-DC converter efficiency-map.	109
Figure 5.5 The Experiment Setup Diagram.	109
Figure 5.6 The closed-loop system model for testing.	110
Figure 5.7 Configuration between the host computer and target computer.	112
Figure 5.8 The DAQ system for target computer.	114
Figure 5.9 (a) The real-time experiment platform. (b) The battery-UC hybrid energy storage system for experiment test.	116

Figure 5.10 The DC-DC converter with current mode control.....	122
Figure 5.11 The input current monitor and regulation circuit in the controller [132].	123
Figure 5.12 The control interface between the target computer and the hardware prototype.	127
Figure 5.13 The test drive cycles. (a) ECE drive cycle; (b) New York City drive cycle; (c) HWFET drive cycle.	130
Figure 5.14 The demand current based on the test drive cycles. (a) ECE drive cycle; (b) New York City drive cycle; (c) HWFET drive cycle.....	131
Figure 5.15 The real-time experiment results under ECE drive cycle. The redline shows the load current.	132
Figure 5.16 The real-time experiment results under New York City drive cycle. The redline shows the load current.	133
Figure 5.17 The real-time experiment results under HWFET drive cycle. The redline shows the load current.	134
Figure 6.1 The potential EV powertrain architectures.....	140

List of Abbreviations

EV	electric vehicle
ESS	energy storage system
UC	ultracapacitor
HESS	hybrid energy storage system
DP	dynamic programming
NN	neural network
SoH	state of health
C-Rate	current rate
SoC	state of charge
HEV	hybrid electric vehicle
PHEV	plug-in hybrid electric vehicle
ICE	internal combustion engine
PEI	power electronics interface
EPA	environmental protection agency
DoD	depth of discharge
EOL	end of lifetime
FCHEV	fuel cell hybrid electric vehicle
SDP	stochastic dynamic programming
MPC	model predictive control
MSE	mean quadratic errors
OCV	open-circuit voltage
DAQ	data acquisition system

UDDS	urban dynamometer driving schedule
NEDC	new European driving cycle
HWFET	highway fuel economy test
EUDC	extra-urban driving cycle

Chapter 1: Introduction to Electric Vehicles and Energy Storage Systems

1.1 Background

The early electric vehicles (EVs) had low driving ranges and poor driving performances due to limited battery energy capacity and power density. During the last two decades, worldwide environmental concerns and lower efficiency of the petroleum-based transportation have renewed the interest in the transportation electrification.

The U.S. Department of Energy's Vehicle Technologies Office's initiatives to support development of innovative battery technologies, novel wide band gap semiconductor devices, enhancement of high-temperature DC capacitors, and advanced power electronics and electrical machines technologies have contributed to the advancement and adoption of EVs. This has created new opportunities for the electrified transportation. More recently, the Department of Energy's investment in battery research and development has helped to cut the EV battery costs by 50% over four years from 2011 to 2014 [1]. In addition to the EV battery cost reduction, the battery power performance, energy and durability have been improved, which in turn have increased the popularity of EVs. It is estimated that more than 415,458 plug-in electric vehicles (PEVs), which includes both EVs and plug-in hybrid electric vehicles (PHEVs), and 3.3 million hybrid electric vehicles (HEVs) are on the road in the U.S. today [2] [3].

1.2 EV Definitions

Pure EVs are powered entirely on electric energy, typically propelled by one or more electric motors with a large battery pack. The battery pack is charged by plugging the vehicle into the electric grid either at home or at a public charging station. EVs do not have an internal combustion engine (ICE) and therefore do not use petroleum.

PHEVs and HEVs rely on two energy sources, typically an ICE and an electric battery with an electric machine. The battery pack is charged through the ICE. Unlike EVs and PHEVs, HEVs are not plugged-in to charge the battery [4] [5] [6].

1.3 EV Configurations

The typical power architecture of an EV is shown in Fig. 1.1. In an EV, usually a high voltage and high energy battery pack is used as the energy storage system. In addition to the energy storage system, an EV is composed of various main power electronic interfaces (PEIs) as shown in the dashed blocks in Fig. 1.1.

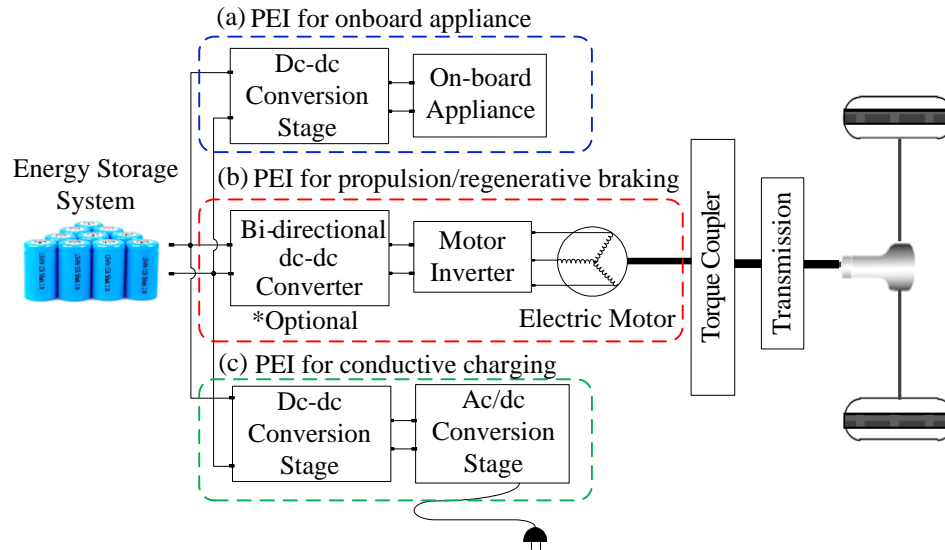


Figure 1.1 Typical Power Architecture of an EV.

These PEIs are used for (a) powering onboard appliances, (b) electric power propulsion and regenerative braking, and (c) onboard charging, respectively. The PEI for onboard appliances contains mainly a DC-DC conversion stage which steps down the high voltage battery pack voltage to 12V voltage to provide power to the onboard electric appliances, such as the air conditioning, headlights, car stereo systems, etc. Energy flow in this PEI is unidirectional. The PEI for electric power propulsion and regenerative braking mainly consists of a DC-DC converter and a motor inverter for the electric machine. The inverter controls the electric machine's operation during propulsion and regenerative braking. In propulsion mode, the power is transferred from the ESS to the electric machine. In regenerative braking mode, the electric machine works as a generator and transfers the regenerative braking power to the ESS. The bi-directional DC-DC converter is used to control battery charging and

discharging power [6]. The PEI for onboard charger is used to charge the battery pack from the electric grid.

1.4 EV Characteristics

EVs have several advantages over the conventional ICE vehicles [7]. First of all, EVs are more energy efficient. EVs can convert about 59% - 62% of the electrical energy from the grid to power at the wheels while the conventional ICE vehicles only convert about 17% - 21% of the energy stored in gasoline to the power at the wheels [7] [8] [9] [10]. Second, EVs are environmental friendly. There is zero tailpipe emission from EVs. Third, EVs show performance benefits as the electric machines can provide quiet and smooth operation with stronger vehicle accelerations. Electric machines also require less maintenance than ICEs.

1.5 Challenges in EV Development

EVs face various energy storage related challenges.

(1) Driving range: Most EVs have electric ranges of 50 - 200 miles before recharging while the conventional ICE vehicles can go over 300 miles without refueling.

(2) Weight, volume and cost: The battery pack is heavy and takes up considerable vehicle space. Furthermore, a large battery pack increases the vehicle cost [11].

(3) Lifetime: The average lifetime for batteries is less than 10 years under recommended operating conditions [12] [13]. For EV applications under daily drive, the battery lifetime span may be shortened due to frequent instantaneous high power

exchange between the electric machine and ESS during propulsion and regenerative braking. Thus, the battery could degrade in an accelerated way [14].

(4) Recharge time: It takes about 5 minutes to refuel the tank in a conventional ICE vehicle; however, depending on the available power and battery capacity, it might take much longer, to recharge the battery of an EV [15] [16].

1.6 EVs on Market

The specifications of some of the commercially available EVs in the market as of March 2016 are listed in Table 1.1.

Table 1.1 Specifications of some of the commercially available EVs in the market as of March 2016.

Model	ESS Energy [kWh]	Motor Power [kW]	Range [Mile]	Curb Weight [kg]
Tesla Model S P85D	85	515	253	2239
Nissan Leaf	24	80	84	1493
Mitsubishi i-MiEV	16	47	62	1080
Toyota Rav4 EV	41.8	114	95	1829
Ford Focus Electric	23	106	76	1651
Chevy Volt	18.4	111	53	1721
BMW i3	22	127	80	1315

Here, the electric range of EVs in Table 1.1 are the range test results based on the US Environmental Protection Agency (EPA) Federal Test Procedure, commonly known as FTP-75 for the city driving cycle. Another commonly used drive cycle for vehicle driving range test is the New European Driving Cycle (NEDC).

Among these EVs on market, the Tesla Model S, equipped with a 85 kWh battery pack containing 7,104 lithium-ion battery cells, can provide an electric range of 253 miles. However, the batteries take up considerable vehicle space, and increase the curb weight and cost of the vehicle.

1.7 Batteries

The future development and commercialization of EVs are highly dependent on the energy storage technologies in terms of the energy capacity, power performances, weight/size, lifetime, cost, etc. The proper assessment of these factors and parameters is a key consideration in determining the applicability of energy storage components [17] [18]. This section introduces these key parameters of the battery energy, power and lifetime.

1.7.1 Energy Density.

For EV applications, a battery pack is the main energy storage component. The energy storage capacity [kWh] of a battery pack directly determines the electric range of an EV and the battery mass. The ratio of the battery energy capacity to the total battery mass or volume is defined as the energy density [Wh/kg] or specific energy [Wh/L].

1.7.2 Current Rate (C-rate).

The battery current is often expressed as a C-rate in order to normalize against the battery capacity. A C-rate is a measure of the rate at which a battery is charged or discharged relative to its maximum capacity. This capacity refers to the coulometric capacity, which is the total Amp-hours [Ah] available when the battery is discharged at a certain discharge current from its nominal voltage at full capacity to the minimum allowable voltage. At 1C rate discharge current, the battery will entirely discharge in 1 hour.

1.7.3 State-of-Charge (SoC).

Battery SoC is an expression of the battery capacity as a percentage of maximum battery capacity. With this definition in place, the SoC of a battery cell can be expressed as a function of time. Suppose the initial SoC value of a battery cell is denoted as $SoC(0)$, nominal battery capacity is Q_b , the current of this battery cell is I_b , which is positive for discharge current and negative for charge current. The SoC value of a battery cell at time t can be expressed as [19],

$$SoC(t) = SoC(0) - \int_{\tau=0}^t \frac{I_b(\tau)}{Q_b} d\tau \quad (1.1)$$

The useable SoC window also determines the available battery energy capacity. For example, for a 40kWh battery with a SoC operation window from 90% to 30%, the actual available energy is 24kWh.

1.7.4 Depth-of-Discharge (DoD).

The DoD is referred to the percentage of battery capacity that has been discharged of its maximum capacity. A DoD of 80% or more is referred as a deep discharge [20].

1.7.5 Power Density.

The power density of a battery is defined as the maximum available power per unit mass or volume. The power density, in units of [W/kg] or [W/L], is a characteristic of the battery chemistry and packaging. Lithium-ion batteries are highly competitive among all kinds of alternatives, due to their comparatively high power density, high energy density, low self-discharging [21] [22]. The excellent characteristics make Lithium-ion batteries widely adopted for the current EV applications.

1.7.6 Lifetime.

U.S. Advanced Battery Consortium (USABC) has defined the battery end-of-life (EOL) as a condition reached when the device under test is no longer capable of meeting the applicable USABC goals [20]. A typical EOL refers to 20% degradation of the battery nominal capacity.

The calendar life is defined as the time required to reach the battery EOL at a reference temperature at open-circuit (corresponding to key-off/standby conditions in EV). The cycle life is defined as the number of discharge-charge cycles the battery can experience before it reaches the EOL at the reference temperature. Simply put, calendar life is the battery life at storage, and cycle life is the number of discharge and charge cycles the battery can survive [20] [23].

The calendar (storage) life is mainly affected by the battery temperature and storage time. The accelerated battery cycle life is strongly affected by battery DoD, temperature and the battery current rate during the discharge/charge cycles.

1.8 Ultracapacitors

UC are electrochemical energy storage devices, which are well known for their extremely high power density, very low internal resistances, high cycle lifetime and cycling efficiency. The UC stores energy by physically separating positive and negative charges. These charges are stored on two parallel plates divided by an insulator. Since there are no chemical variations on the electrodes, therefore, UCs have a long cycle life but low energy density [6].

An UC pack consists of cells in series and possibly also in parallel as is the case for batteries. In most cases, a number of cells are combined into modules for the assembling convenience for the EV applications.

1.8.1 Energy.

The total energy stored in an UC can be expressed as,

$$E_{uc} = \frac{1}{2} C V_{uc}^2 \cdot [\text{Ws}] \quad (1.2)$$

Here C refers to the UC capacitance and V_{uc} is the UC voltage. The minimum voltage of an UC is generally set by users to avoid deep discharge of the UC. A completely discharged UC may draw extremely high charging current during

recharge if not well controlled. By setting the minimum UC voltage, the available energy from UC is also constrained.

Typically, UC has much lower energy density in comparison to the energy density of the lithium-ion battery.

1.8.2 Power.

The key cell performance characteristic for determining the UC maximum pulse power is its internal resistance R_{uc} . Often the power capability of an UC cell is calculated from the relationship of $(V_{uc})^2/4R_{uc}$. This UC power capability is achieved with a power efficiency of 50% which results in high losses and high heat generation at this low power efficiency. Therefore, it is not desirable to operate or use UC at this high power level with low efficiency due to the loss and heat considerations. More practical UC usage for EV application is at efficiency of 75-80% and of 90-95% for hybrid vehicle operation [24].

1.8.3 State-of-Art of UC.

UC cells from various manufacturers are tested at the University of California, Davis with the test results summarized in Table 1.2 [21].

Table 1.2 Summary of the Performance Characteristics of UC Devices. [21]

Manufacturer	Rated voltage [V]	C [F]	R_{uc} [mOhm]	Energy Density [Wh/kg]	Power Density [W/kg]	Weight [kg]	Volume [L]
Maxwell	2.7	2885	0.375	4.2	994	0.55	0.414
Ness	2.7	1800	0.55	3.6	975	0.38	0.277
Panasonic	2.5	1200	1.0	2.3	514	0.34	0.245
EPCOS	2.7	3400	0.45	4.3	760	0.60	0.48
LS Cable	2.8	3200	0.45	4.3	760	0.60	0.48
BatScap	2.7	2680	0.20	4.2	2050	0.50	0.572
Fuji	3.8	1800	1.5	9.2	1025	0.232	0.143
ApowerCap	2.7	55	4	5.5	5695	0.009	---

Here the UC power density [W/kg] is measured with 95% efficiency. According to Table 1.2, the Fuji offers a UC cell with highest rated voltage and energy density. The ApowerCap offers a UC cell that achieves the maximum power density among the other manufacturers.

1.9 Fuel Cells

Fuel cells generate electricity from fuels. During the generation process, the reactant flows in, whereas the reaction products flow out. The fuel cell is able to generate electricity as long as the reactant flows are maintained. Different combinations of fuels and oxidants are possible fuels for fuel cells. Hydrogen is an ideal fuel for fuel cells as it has the highest energy density than any other fuel and its

reaction product is just water, which is nonpolluting. The advantages of the fuel cell include good energy conversion efficiency from fuel to electrical energy, quiet operation, zero or very low emission, waste heat recoverability, fuel flexibility, durability and reliability. Different from batteries, the fuel cell needs to be refilled with the reactants before they are used up. A specific fuel tank should be included on board for vehicular applications. With an energy density about 2.6kWh/L for liquid hydrogen (compared with 6kWh/L for petrol), a large fuel tank is required on board.

The disadvantages of fuel cells include relatively longer response time in comparison to that of the batteries and UCs. Another drawback is the high cost of fuel cells. Fuel cells cost about five times more than the traditional ICEs [6].

1.10 Hybrid Energy Storage Systems

Nowadays, the vehicle manufacturers use lithium-ion batteries as the only source to supply the energy and power to the vehicle. To provide longer driving range, high energy density batteries are preferred in EVs. In current and upcoming EVs, the batteries are oversized in order to deliver high power and avoid unwanted degradation due to acceleration and deceleration.

Topologies to hybridize different ESSs for EVs, HEVs, fuel cell hybrid vehicles and PHEVs have been proposed and developed in order to make advantages of their complementary advantages. The developed hybrid systems include the battery-UC, battery-fuel cell, UC-fuel cell and the battery-UC-fuel cell hybrid energy systems. In this work, we mainly focus on the design of battery-UC HESS.

The integration of a high energy density battery pack and an UC pack in the EV

powertrain creates a battery-UC HESS that combines the high energy density attribute of batteries and the high power density of UCs. With these complementary features, a battery-UC HESS can achieve high power capabilities and large energy storage at the same time with smaller size and weight in comparison to the high power battery-only ESS counterpart. Hybridization of UCs with batteries also enhances battery lifetime through peak power shaving, improved dynamic performance and thermal burden relief [12] [25] [26] [27] [28] [29] [30] [31].

1.11 Sizing Problem in HESS

An important aspect of the ESS design is its proper sizing. The ESS sizing is to calculate the size of different energy storage components that are required to satisfy the load demands at the minimum weight, volume and cost. The battery-UC HESS sizing problem is to find an optimal combination of the battery-UC cell number (N_{bat} , N_{uc}) in order to minimize the HESS weight, size or cost, and to fulfill all the EV specifications in terms of range, power requirement, acceleration time, etc.

The trade-offs between the ESS size/weight, battery lifetime, economic cost, overall vehicle efficiency and driving range have been studied partly in the literature, which are reviewed in Section 2.2, Chapter 2 of this dissertation. The design methodologies and the general sizing approaches are to determine the load requirements and size the energy storage components based on the transient power requirements and constraints imposed by the main energy source needs. One of the major challenges in the HESS sizing problem is that the existence of the interdependence between the HESS energy management problem and the HESS

sizing. With different numbers of the battery or UC cells, the HESS power split can be determined differently. Likewise, the HESS energy management techniques also provide insight on how to size the HESS in order to satisfy the transient power requirements and the energy sources needs. We investigated into the interdependence between HESS sizing and energy management problems.

1.12 Energy Management Problems

Energy management in vehicles is an important issue because it can significantly influence the vehicle performances. An optimal energy management strategy can provide substantial advantages such as reducing fuel consumption, decreasing emission, reducing pollution, and improving the vehicle driving performance.

In HEVs and PHEVs, a combination of an ICE and an electric machine is used to deliver the power demand. The energy management problem in these vehicles is to split the requested power between the ICE and electric machine. For HEV and PHEV applications, one main objective of energy management is to optimize the fuel consumption and reduce emissions.

In EV applications with a battery-UC HESS, the energy management problem is to decide the power split between the battery and UC. The main objective of the energy management problem includes improving the HESS operation efficiency and extending the battery lifetime.

Though this work will be mainly focused on the battery-UC HESS for EV applications, the proposed energy management control strategy and the design

methodology will be extendable to any hybrid system including the battery, UC, fuel cell, flywheel or any combination of various energy storage systems.

1.13 Summary and Dissertation Overview

A key consideration in EV development is the ESS design. The characteristics of different ESS are introduced and discussed with a focus on the battery and UC as they are promising energy storage components for EV applications.

It has been demonstrated that the integration of battery and UC would significantly reduce the maximum power output required from the battery and therefore can reduce the stress on the batteries. With an appropriate sizing design of the energy storage system, it would effectively reduce the system weight and cost. To maximum the benefit of the battery-UC HESS, an energy management control strategy is needed to split the power demand between the battery and UC.

This dissertation consists of six chapters.

Chapter 1 gives the introduction to EV and ESS. The ESS sizing problem and the energy management problem are outlined in this chapter.

Chapter 2 provides the detailed overview of the state of art of the HESS configurations, the HESS sizing problem and the HESS energy management problems. A comprehensive review and comparisons of the HESS energy management control strategies are presented and discussed.

Chapter 3 presents the HESS sizing problem. The HESS sizing problem and a convex optimization-based power split problem are combined to investigate the interdependence between the sizing problem and the energy management problem. A

systematic approach to optimize the HESS sizing is proposed to evaluate the HESS sizing and the power split objectives simultaneously. With different optimization objectives, vehicle models, HESS energy management strategies and design variables, this HESS sizing approach can be adapted.

Chapter 4 presents the development of a real-time implementable HESS energy management controller. A multi-objective optimization problem is formulated with the objectives to reduce the HESS losses and extend the battery cycle life. This nonlinear multi-objective optimization problem is solved offline using DP algorithm to obtain the global optimal power split results. The obtained DP results are used as the training sets to a NN, which will be implemented online for the real-time HESS energy management. To evaluate the proposed energy management controller, a battery SoH estimation model is developed as the performance metric. The simulation results are presented. It is estimated that the proposed online energy management controller can extend the battery life by over 60%.

Chapter 5 presents the development of the 38V-385Wh battery module and a 16V-2.06Wh UC HESS hardware prototype and a real-time experiment platform. The performance of the real-time energy management strategy is tested using standard drive cycles, which validated the effectiveness of the real-time energy management controller design and implementations.

Finally, we conclude in Chapter 6 with a summary of the main contributions of the dissertation work and considering potential future prospects in this research area.

The major contributions in this work are listed as follows.

- Developed a new battery state-of-health estimation model under realistic drive cycles.
- Formulated the multi-objective energy management optimization problem.
- Implemented an offline energy management control strategy for EVs with hybrid battery-UC storage systems.
- Proposed an innovative real-time implementable energy management control strategy for hybrid energy storage systems, which demonstrated $> 95\%$ efficiency and 60% battery lifetime extension.
- Developed a novel real-time experimental platform to validate the design of real-time controllers.

Chapter 2: Literature Review and State-of-the-Art

2.1 HESS Configurations

Different HESS configurations have been discussed in the literature [6] [32] [33]

[34]. The general topologies of HESS are shown in Fig. 2.1.

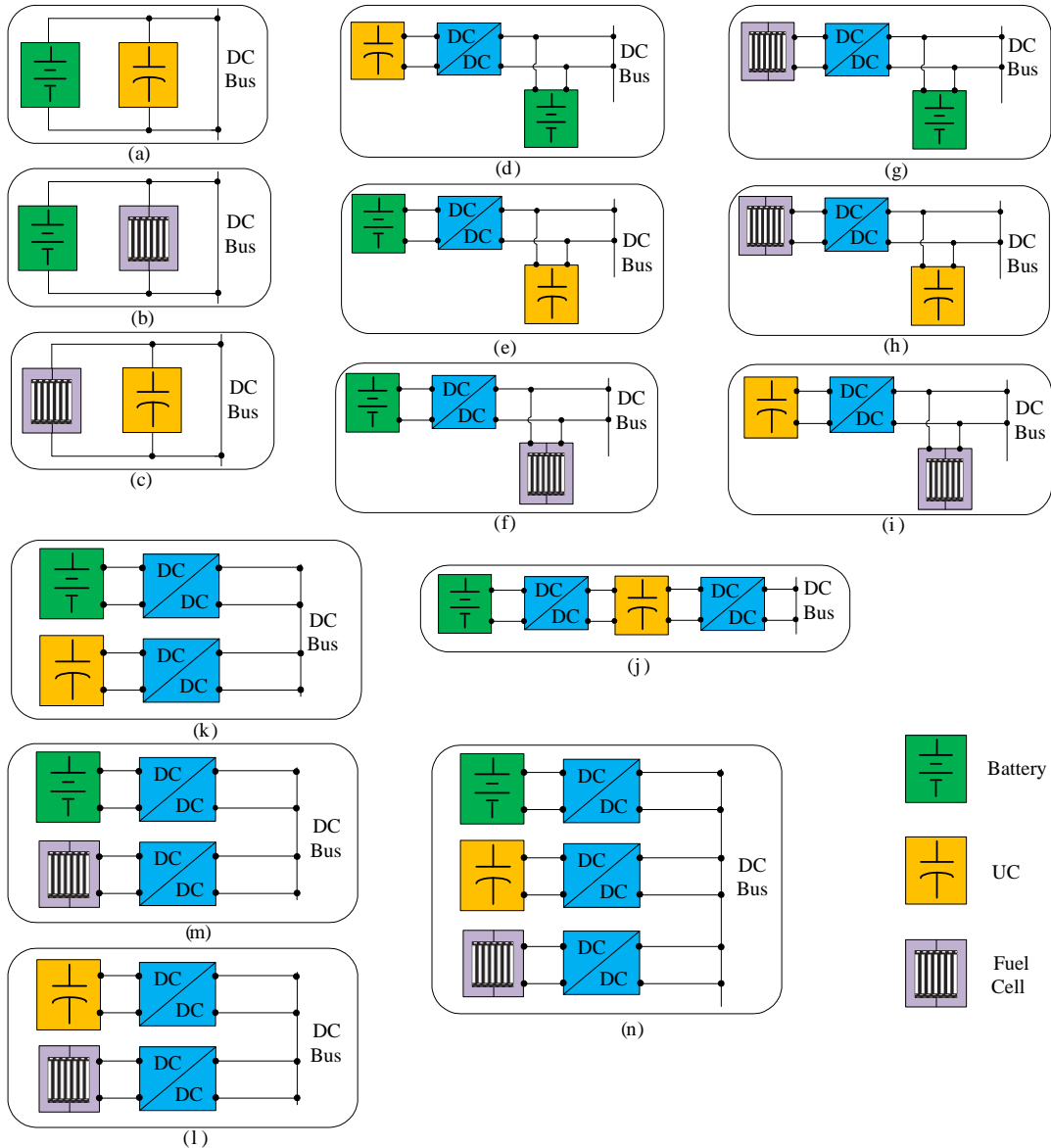


Figure 2.1 Different HESS topologies.

The topologies in Fig. 2.1(a)-Fig. 2.1(c) are called passive parallel connection. Researchers [35] [36] [37] [38] have considered direct parallel connection of the two energy storage components as the simplest way to connect the battery and the UC and/or the fuel cell to the DC bus. The advantage of this topology is the simplicity of implementation and relatively low cost; however, it has two major drawbacks. First, the battery and the UC and/or the fuel cell cannot be separately controlled. It is not possible to control or determine which energy storage component to use because both energy storage devices are charged and discharged concurrently. Second, the UC utilization is low. The UC voltage experiences very small and slow variation as the UC voltage is clamped to the battery terminals or the fuel cell terminals.

The passive parallel connection topology of the battery and the UC pack in Fig. 2.1(a) can be improved by adding a DC-DC converter between the battery pack and the UC pack as shown in Fig. 2.1(d) and Fig. 2.1(e) [39] [40].

In a battery-UC HESS, a DC-DC converter is used to interface the battery and/or the UC with the DC bus. In the topology in Fig. 2.1(e), the battery is decoupled from the DC bus through a unidirectional or a bi-directional DC-DC converter. With a unidirectional DC-DC converter, the battery voltage can be boosted to a higher level; thus a smaller sized battery could be selected to reduce cost. However, the battery can neither be charged by the regenerative braking energy nor by the UC due to the unidirectional boost converter [6]. With a bi-directional DC-DC converter, both the battery power input and output can be controlled through the control of the bi-directional DC-DC converter. Thus, the battery current or power can be more efficiently controlled in comparison with the passive parallel connection.

One advantage of this topology in Fig. 2.1(e) is that energy management control strategies can be implemented to split the power demand for both the battery and the UC pack. The drawback of this topology is that a high voltage UC pack is required in order to drive the motor inverter. In addition, the UC voltage swing is limited by the inverter input voltage range. Hence, the UC utilization may be limited.

To improve the operation range of UC, another bi-directional DC-DC converter is added between the UC and the DC bus. This forms a cascaded converter topology as shown in Fig. 2.1(j). In this topology, two DC-DC converters are used. The DC-DC converter between battery and UC is used to control the current input or output of the battery, while the UC supplies the remaining power to the load. The other DC-DC converter decouples the UC from the DC bus.

By swapping the position of the battery and UC in the battery/UC topology as shown in Fig. 2.1(e), the UC/battery topology is obtained as shown in Fig. 2.1(d) [41] [42] [43].

As shown in Fig. 2.1(d), the UC is decoupled from the DC bus. Thus, the UC voltage can be used in a wide range. The UC power can be controlled through the control of the DC-DC converter. In this topology, the power rating of the DC-DC converter is determined by the UC power. In addition, the nominal voltage of the UC can be lower, which may reduce the UC size and cost. The battery is connected directly to the DC bus; as a result, the DC bus voltage is maintained around the battery nominal voltage and will not be varied much.

Both the topologies in Fig. 2.1(d) and Fig. 2.1(e) are called partially decoupled configurations or semi-active topologies because either the battery or the UC is

decoupled from the DC bus via a DC-DC converter. Although the DC-DC converter adds additional cost and weight to the system, it offers the major advantage that allows separate control of the battery and the UC, which cannot be achieved in the topology as shown in Fig. 2.1(a) with passive parallel connections.

Instead of the cascaded connection of the two converters given in Fig. 2.1(j), the multiple converters parallel the output of the two DC-DC converters as shown in Fig. 2.1(k) - Fig. 2.1(n) [44] [45] [46] [47]. The topology in Fig. 2.1(k) is called a full active battery-UC system or a fully decoupled configuration as both the battery and the UC are decoupled from the DC bus. The battery and UC are connected to the DC bus in parallel and interfaced by two different DC-DC converters. In this topology, both the battery and UC present a lower voltage level than the DC bus voltages. The voltages of the battery and the UC will be leveled up when there is a power demand from the drive train and will be stepped down for regenerative braking conditions. This topology offers the highest flexibility and full control on the operation of the battery and the UC. However, the system is expected to be heavier, larger, more complex to control and more expensive than other topologies with the two integrated DC-DC converters [6]. Besides, the system may have increasing energy losses due to a larger number of power electronics devices and passive components.

Instead of the topology with two full-size DC-DC converters, the multiple inputs converter topology is proposed in [48] [49]. The circuit diagram of a multiple inputs DC-DC converter is shown in Fig. 2.2.

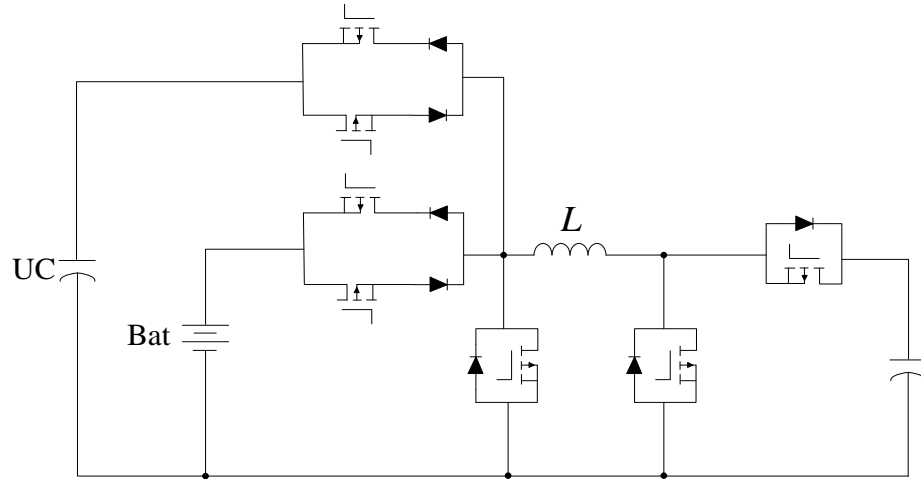


Fig. 2.2 Multiple Inputs DC-DC converter in [44].

In this multiple input DC-DC converter, both the battery and UC are connected to one common inductor by anti-parallel switches. Each switch is paired with a diode, which is designed to avoid short circuit between the battery and the UC. The power flow between multiple inputs and the load is managed by controlling the multiple inputs DC-DC converter. In this topology only one inductor is needed even if more inputs are added into the system. This will reduce the size and cost of the system in comparison to the topology in Fig. 2.1(k). However, the energy management strategy and the power flow management of the multiple inputs DC-DC converter are more complicated [6]. In addition, it is not practical to charge the battery and UC simultaneously.

The characteristics of these three main types of HESS topologies are summarized in Table 2.1.

Table 2.1 A Comparison of HESS Topologies.

Topology	Advantages	Disadvantages
Passive	<ul style="list-style-type: none"> (1) Simplicity (2) High reliability (3) Low cost 	<ul style="list-style-type: none"> (1) Cannot be actively controlled (2) Has limited utilization of energy storage components
Semi-Active	<ul style="list-style-type: none"> (1) Can implement semi-active control strategies (2) Can expand the operation range of the actively controlled energy storage components to enhance HESS performance (3) Provides partial flexibility to reduce size/voltage of some of the actively controlled energy storage components 	<ul style="list-style-type: none"> (1) As batteries are preferred to interface with the DC bus to provide stable voltage, they may expose to load fluctuations if active controls are not well implemented.
Full-Active	<ul style="list-style-type: none"> (1) Highest flexibility and full active control on all the energy storage components (2) Can expand the operation range of all energy storage components thus enhancing HESS power performance (3) Has potential to reduce size/voltage of all the energy storage components 	<ul style="list-style-type: none"> (1) Large system size/weight and high cost due to need for more DC-DC converters (2) High power losses due to more power electronics

2.2 HESS Sizing Strategies

Researchers have proposed different solutions to HESS sizing problem. The HESS sizing problems with different ESS combinations have been studied, such as the battery-fuel cell [50] [51], the battery-UC [25] [52] [53] [54] [55] [56] [57], the UC-fuel cell [50], and the battery-UC-fuel cell combinations [50]. Though different combinations of ESSs have been designed, the sizing design methodologies can be generalized and adopted for all these different combinations.

In [54], the influence of the battery-UC HESS sizing on battery lifetime has been investigated for a fuel cell hybrid electric vehicle (FCHEV). The main purposes of the energy storage components in a FCHEV are to provide power to the load during the heating up of the fuel cell stack, or to supply peak power to the load to reduce the required power rating of the fuel cell stack, and to capture the braking energy. Sizing the battery based on its energy usage does not prevent it from deep discharges, which might reduce the battery lifetime. Thus, in this application, a sufficient sizing of the battery and the UC is an important issue in order to obtain an appropriate tradeoff between the system volume, mass and the battery lifetime.

As a starting point of the sizing problem, a base maximum power and energy rating for both the battery and UC are predefined as $P_{bat,max,base} = 5.4kW$, $P_{uc,max,base} = 16.8kW$, $E_{bat,max,base} = 770Wh$, $E_{uc,max,base} = 13.5Wh$ respectively, based on the system model and design experience [54]. With these values, the power and energy requirements of the battery and UC can both be satisfied when the UC provides the transient peak power and the battery delivers the slower average load

power. The goal of this sizing problem is to investigate how the system volume, mass and the battery lifetime will be affected if either the battery or UC is oversized. A set of oversize/overrate factor is defined as $\alpha_{or,bat} = \{1, 2, 3, 4, 5\}$ relative to the base values of the maximum power and energy. Thus, the power and energy rating of the battery are given by,

$$P_{bat,max} = \alpha_{or,bat} P_{bat,max,base} \quad (2.1)$$

$$E_{bat,max} = \alpha_{or,bat} E_{bat,max,base} \quad (2.2)$$

Obviously, if the battery is oversized, it will experience less deep discharge cycles in tradeoff between the increased system mass and volume.

Similarly, an oversize factor is defined for UC with $\alpha_{or,uc} = \{1, 2, 4, 6, 8, 10\}$.

With a set of comprehensive simulation and case studies, it is concluded that it is not advantageous to overrate the UC more than a factor of $\alpha_{or,uc} = 2$, since better tradeoff between system size and the battery lifetime can be achieved by overrating the batteries instead of the UCs.

This work investigates the sizing influence on the battery lifetime. The provided analysis also gives recommendations on the design of the battery and UC energy storage systems for the FCHEV.

[25] also provides a sizing methodology that considers the battery lifetime. In this work, the battery-UC HESS is sized for a HEV application. In this sizing problem, the authors assume that a life requirement should be satisfied with an energy throughput of the total ESS module of 25MWh over 10 years and 100k mile. To

sustain this energy throughput requirement within 10 years, the battery would have a 3% or less DoD for every 50Wh discharge-charge event according to a rough estimation model in [25]. The UC is sized in a separate way to ensure it can operate at an average 85% efficiency based on a UC power efficiency model.

This work provides the sizing considerations, however, the results are obtained based on coarse estimation models.

Instead of these coarse sizing methodologies, [57] uses simple control strategies and proposes a sizing methodology by setting the size of the primary source based on the mean power of drive cycles. This sizing methodology can provide a general good choice but the sizing results can be improved with a specific drive cycle [51].

In [51], a new sizing methodology is proposed by combining the sizing and energy management problem. The study finds the best sizing for the fuel cell and the battery, assuming that an optimal power split is implemented for a specific drive cycle. Two interlinked optimization loops are built to run simultaneously. A first optimization is run on sizing by choosing various combinations of the fuel cell rated power and the battery capacity. Each combination is then used as an input to the energy management problem in the second optimization loop, which determines the optimal power split strategy that can achieve a minimization of the fuel consumption. The proposed two interlinked optimization loops can return the best sizing and the corresponding optimal energy management results based on the design optimization algorithms .

For the battery-UC HESS sizing problem, [52] [56] have investigated the interdependence between the energy management strategy and the sizing. The HESS

is designed by assuming that the power split between the sources is performed with a frequency-based strategy, i.e., UC is used to handle the high frequency peak power while the battery provides the low frequency power or the average power demands. With the power demand split among the energy sources, the total energy storage and power requirement for each energy source can be estimated. Therefore, the optimal sizing can be determined based on these energy demands and power requirements.

2.3 HESS Energy Management Strategies

Effectively splitting the load demand between the battery and UC is a major challenge. To optimally split the power between batteries and UCs, it is difficult to develop a deterministic control equation or strategy as many factors and parameters are involved, such as the trip length, the driver command, the electric motor/generator speed, and the UC SoC, etc. The effects of these factors become even more complex with uncertainties. For real-time driving, the future driving trend and the trip length are not available. Without these data and information, one may make shortsighted control for the power split problem.

The main objectives in the HESS power split problem is to meet the load demand, sustain the battery and UC charge, improve the HESS efficiency and extend the battery lifetime. A good energy management strategy should provide a good tradeoff among these objectives.

Different energy management strategies have been proposed in literature for power split in HEVs, PHEVs or hybrid energy storage systems in EVs. Majority of the prior work is proposed for power decoupling between ICEs and electric machines

or power decoupling between fuel cell systems with UC and/or batteries. Similar energy management techniques can be adopted for battery/UC hybridization. Mainly, the energy management strategies can be categorized into two types, (i) rule-based methods and (ii) optimization-based strategies. This section extensively discusses the main proposed energy management strategies. The advantages and disadvantages of each method are explained.

2.3.1 Rule-Based Energy Management Methods

Strategies that are based on heuristics or empiric experience can be easily implemented by rule-based control algorithms [58] [59] [60] [61] [52] [62]. In these rule-based control algorithms, the heuristics or empiric experience are utilized to design deterministic rules, generally implemented via if-then rule expressions or look-up tables. According to these rules, the power demand is split between different energy storage components or power sources.

Rule-based control algorithms have been applied to the power split problem in HEVs [58] and PHEVs [59]. For HEV and PHEV power split problems, the energy management problem is employed to split the power demand between the ICE and the battery such that these power sources are operated at high efficiency. In [58], the energy management rules are designed based on the values of selected variables including the power demand, the driver's acceleration command and the battery SoC. Given the status or value of the power demand, the acceleration command and the battery SoC, the if-then rules are designed to split the power and assign to the ICE, to the battery, or to a combination of both.

A rule-based control strategy is described in [63] for the power split problem in a hybrid electric truck. Based on the engine efficiency map [63], a predefined “engine on” power line P_{e_on} and a “motor assist” power line P_{m_a} , are chosen to avoid engine operation in inefficient areas with $P_{e_on} < P_{m_a}$. If the power demand is less than the “engine on” power level, the electric machine with the battery will supply the demand power while the engine is not working. This avoids the engine operating in low efficiency region. Above the “engine on” power level, the engine replaces the electric machine to provide the total demand power. Once the demand power exceeds the defined “motor assist” power, it means that the engine cannot efficiently generate the total demand power by its own. The engine provides the “motor assist” power P_{m_a} and the electric machine is activated to supply the additional power to satisfy the demand.

A similar rule-based control strategy is proposed in [60] for a battery-UC HESS power split problem. In this control strategy, a pre-selected reference battery power with the value of P_{min} is used. The rule-based control strategy is set up based on the following rules. (1) If the load demand power P_{dmd} is below 0 (i.e. there is regenerative braking power), the UC receives all the regenerative braking power within its charging limit; (2) If the load demand power P_{dmd} is greater than P_{min} , UC delivers $(P_{dmd} - P_{min})$ or its max discharging power at that state while battery provides P_{min} ; (3) Otherwise, battery supplies the discharging power within the battery discharging limit.

Using this rule-based control strategy, the authors have shown that the hybridized battery-UC system can effectively reduce the battery peak current and to extend the battery lifetime [60].

Another representative rule-based energy management control strategy is the frequency based power decomposition strategy, which is employed in [61] [52] for the power split in a battery-UC HESS. In this strategy, the demand power of the HESS is decomposed as a sum of a low frequency and high frequency signals. According to the demand power decomposition, the batteries and UCs are used to provide the low and high frequency contents of the load demand power, respectively. However, the filter-based strategies have several deficiencies. One critical disadvantage of a simple filter-based method is that it introduces large phase shift as reported in [61]. The effectiveness of using UC system in reducing the battery current and losses is degraded due to this phase shift. In addition, one needs to adjust the cutoff frequency or other parameters in the filter design for different load demands in order to obtain effective power split results in different situations.

Despite being simple and numerically efficient, these control strategies and methods are heuristic controllers, not optimal power split solutions. These heuristic controllers do not guarantee an effective control in different driving situations.

2.3.2 Fuzzy Logic-Based Energy Management Methods

As an extension to the conventional rule-based control methods, the fuzzy logic approach is proposed [64] [65] [66] [67] [68] [69] [70]. Fuzzy logic based control strategies, which are good at dealing with model uncertainty and complex decisions,

have been proposed and applied for vehicle control and energy management. For energy management problems, there are many factors and parameters involved in the complicated control and model systems. The effect of many control factors and model parameters may be known, but not clearly. The basic idea of a fuzzy logic based control strategy is to use the available knowledge about the problem to construct a number of fuzzy rules to formulate human intelligence and reasoning, which can be represented as a collection of if-then rules based on heuristics or empiric experience. The main advantages of the fuzzy logic based methods are the following: 1) robustness and tolerant to imprecise measurements and component variations, and 2) flexibility and adaptation, as the fuzzy logic rules can be easily tuned.

Fuzzy logic based control strategy have been applied and implemented in HEV control. In [64], a set of fuzzy logic control rules has been developed using the driver commands, the battery SoC and the motor/generator speed as the fuzzy logic controller input. The fuzzy logic controller outputs the optimal generator power for the electric machine and a scaling factor for the electric machine when the electric machine is used as a motor. This scaling factor is (close to) zero when the battery SoC is at very low level. In that case, the electric machine is not used to deliver the power in order to prevent the battery damage. The scaling factor equals one when the battery SoC is high enough. In that case, the electric machine is used to deliver the power instead of the ICE in order to reduce fuel use. The developed fuzzy logic based energy management control strategy effectively split the power between the two power plants: the electric machine and the ICE to improve the operational efficiency of all components and the fuel economy.

In [69], fuzzy logic based control strategy were used in the energy management problem in a PHEV to improve the fuel economy and reduce emissions. In [65] [66], the fuzzy logic control strategies are introduced in a power split problem between fuel cells, batteries and UCs. Real vehicle test data are provided, which showed the fuzzy logic control strategy can achieve the power split target while maintaining the battery SoC within a specified range for PHEV applications.

For EV applications with a battery-UC HESS, a fuzzy logic supervisory controller based on frequency decoupling strategy is proposed in [68]. The proposed fuzzy logic supervisory controller evaluates the load power demand and the UC SoC and then modifies the power references for both battery and UC achieved from the frequency decomposition strategy. In this fuzzy logic controller, the load demand power and the UC SoC are defined as the two input membership functions. Based on these two inputs, given rules, input and output membership functions, a fuzzy number with a normalized membership function is produced. For the input UC SoC, three membership functions are used, namely “Low”, “Medium”, and “High”, whereas the input of the load demand power is represented by five membership functions, namely “Regen”, “Light”, “Med”, “Heavy”, and “VHeavy”. The rules for this fuzzy logic controller, which basically dictate 12 different conditions, are determined based on the experience and the real physical system.

The fuzzy logic controller generates a positive power value regardless of demand power when the UC SoC is at the 'High' state, which will discharge UC. As the UC SoC is at the 'Medium' state, UC can store a portion of the regenerative braking energy when the demand power is less than zero or assist the battery to deliver the

propulsion power if the demand power is greater than 0. When the UC SoC is at the 'Low' state, UC captures the regenerative braking energy completely during braking or partially assists battery in the case when the demand power is greater than 0. The fuzzy logic controller outputs a power value based on these rules. The output power value is then added to the UC power references generated by the frequency decomposition methods to modify the frequency decomposition results based on different states of the demand power and UC SoC.

This proposed fuzzy logic method is more robust than the conventional rule-based control strategy because it takes the load demand and UC state variations into account to generate the power references for HESS power split, instead of only using the frequency decomposition for power split. Both fuzzy logic and rule-based control strategies are real-time implementable. However, the fuzzy logic control strategy cannot guarantee an effective control or the optimal control under different driving situations as it still depends on rules and experiences. Another disadvantage of the fuzzy logic based method is that the defuzzification process consumes memory and time in the controller.

2.3.3 Global Optimization Based Control Strategy

By optimizing a cost function representing efficiency or fuel consumption or other objectives over a drive cycle, an optimization problem is formulated to find the global optimal operating points for power split. Linear programming [71] and dynamic programming are utilized to solve the aforementioned global optimization problem. Dynamic programming is discussed in details.

DP is a powerful numerical tool to determine the optimal control policies or trajectories explicitly using the Bellman's optimality principle [72]. Therefore, the DP solution is the global optimum even for nonlinear systems with constraints [73] [74]. Kolmanovsky *et al.* [75] describe how to apply DP to obtain the optimal powertrain control policies from a software implementation perspectives.

Unlike the rule-based methods, the DP algorithm usually relies on a model to compute the best control strategy. This model can be either analytical or numerical. Based on the model, the best power split control strategy can be obtained by solving the DP problem.

In order to find the global optimal solution of the energy management problems, DP has been first applied to the power split problem in HEV [63] [76] [77] [78] [79] [80]. In [77], DP is utilized to find the optimal control actions including the gear-shifting sequence and the power split between the engine and the electric motor while subject to a battery SoC-sustaining constraint.

In [77], the DP problem is formulated with the control variables of the fuel injection rate to the engine [kg/cycle], the desired output torque from the motor [Nm] and the gear shift command to the transmission. A numerical DP approach is applied to solve the finite horizon optimization problem. The optimal, time-varying, state-feedback control policy is obtained at each of the quantized states and time states. In this way, DP creates a family of optimal paths for all possible initial conditions. Once the initial state of the battery SoC is given, the optimal policy is applied to find an optimal path that can achieve the minimal fuel consumption.

In [74], DP is applied in the energy management problem in a series HEV with the objectives of maximizing the vehicle fuel economy and also minimizing the battery usage, which is represented by the battery cumulative bulk mechanical stress (BCBMS). The instantaneous cost function is a weighted sum of the normalized fuel consumption, the normalized bulk stress and the normalized battery current. In this problem, the battery power is used as the control variable and the battery SoC and the engine power are used as the state variables. By solving this problem with DP, the optimal solution is obtained with the tradeoff between fuel consumption and battery cycle life discussed in [74].

DP is applied in a PHEV energy management problem in [81]. In a PHEV, the charge-depletion mode is more appropriate or desired for the purpose of improving fuel economy, i.e. the battery SoC is expected to drop to a preselected low threshold when the vehicle reaches the destination of the trip. In [81], charge-depletion control of PHEV is nearly globally optimized with a two-scale DP approach based on trip modeling with the real-time and historical traffic data. By specifying the starting point and the end point of a trip, the trip model, i.e. the drive cycle, is first obtained by averaging the historic traffic data. DP is applied to the overall macro-scale problem to obtain the global optimal path of the battery SoC. To adapt this global optimal control strategy during the real-time vehicle operation, a micro-scale framework is proposed by dividing the whole trip into a number of segments. For each segment, a smaller DP will be solved using the online traffic data within this segment. The online traffic data is transmitted to the vehicle from the traffic flow sensors. At the end of the trip, the battery SoC, obtained in the macro-scale DP

solution, is reinforced to be the final value. Simulation study based on this two-scale DP algorithm has been performed on a hybrid SUV model from ADVISOR software on a defined trip [81]. The simulation results demonstrated significant improvement in fuel economy using DP based charge-depletion control in comparison to a rule based control strategy.

DP is well-known for requiring high computations that grow exponentially with the number of states [63]. To reduce the number of states, simplified vehicle models are developed for the optimization purposes [63] [74]. For DP algorithms applied in the power split problems, they usually assume that the entire drive cycle and load demand profile are known. Therefore, the DP algorithms are not implementable in real-time due to their preview nature and the heavy computational requirements. Nevertheless, DP algorithms are good design tools and provide benchmarks against which other energy management control strategies can be compared and improved.

2.3.4 Stochastic Dynamic Programming Based Control Strategy

In an earlier work [63], Lin *et al.* proposed a design procedure that uses DP (or deterministic DP) to find the optimal power split solution and then extracts rules to implement a real-time rule-based control strategy. The DP algorithms can be applied to solve global optimization problem for a specific drive cycle. The obtained rule-based control policy might be neither optimal nor charge-sustaining under other drive cycles. In addition, the optimal solution obtained from DP is not directly implementable. To extract an implementable control rules based on the DP optimal solution might be also time-consuming [63]. To overcome these drawbacks, a design

procedure based on stochastic dynamic programming (SDP) optimization techniques is proposed by Lin *et al.* in [82]. The proposed SDP algorithm is applied to address the power split optimization problem in a HEV with the objective of maximizing the fuel economy and reducing the exhaust emissions. Instead of being optimized over a given specific drive cycle, the power management strategy is optimized over a family of representative drive cycles in an average sense. In order to obtain a time-invariant control strategy, an infinite-horizon optimization problem is formulated and solved using SDP. The key benefit of generating a time-invariant control policy is that the control policy can be directly used in real-time implementations.

In most power split problem where DP algorithm is applied, the power demand is used as a-priori information (e.g., a known power demand path to follow a given specific drive cycle). In order to formulate an infinite-horizon optimization problem, the power demand is modeled as a discrete-time stochastic dynamic process [82] [83] [84] [85]. A stationary Markov chain is used to generate the power demand from the driver, which is assumed to take on a finite number of values [82] as,

$$P_{dmd} \in \{P_{dmd}^1, P_{dmd}^2, \dots, P_{dmd}^{N_p}\} \quad (2.3)$$

where N_p represents the total number of the possible discrete values of the power demand. Moreover, the wheel speed is also discretized into a finite number of values as,

$$\omega_{wh} \in \{\omega_{wh}^1, \omega_{wh}^2, \dots, \omega_{wh}^{N_\omega}\} \quad (2.4)$$

The dynamics of the power demand is assumed to be $P_{dmd,k+1} = w_k$, where the probability distribution of w_k is assumed to be,

$$\Pr\left\{w = P_{dmd}^j \mid P_{dmd} = P_{dmd}^i, \omega_{wh} = \omega_{wh}^l\right\} = p_{il,j},$$

$$i, j = 1, 2, \dots, N_p, \quad l = 1, 2, \dots, N_\omega \quad (2.5)$$

where k is the time index, $p_{il,j}$ represents the one-step transition probability that the system will be with the power demand of P_{dmd}^j at time step $k + 1$, given the system is with power demand of P_{dmd}^i and the wheel speed of ω_{wh}^l at time step k .

A natural way to determine the transition probabilities values is to estimate them on the basis of the observed sample drive cycles, such as the past driving records, or standard representative drive cycles. From the speed profiles, the power demand P_{dmd} and the wheel speed ω_{wh} could be calculated given the vehicle model. Using the nearest-neighbor quantization, the sequence of observations (P_{dmd}, ω_{wh}) is mapped into a sequence of quantized states. The transition probabilities could be estimated based on this sequence of quantized states.

After the Markov model of the power demand is built, the stochastic hybrid vehicle model is constructed [82]. This model includes three state variables: the battery SoC, wheel speed and the power demand. The Markov model of the power demand is used to determine the probability distribution of future power demands and to generate a sequence of a random drive cycle. A power management controller is

then optimized on the basis of this stochastic model. The expected total cost over an infinite horizon can be represented as,

$$J_{\pi}(x_0) = \lim_{N \rightarrow \infty} E \left\{ \sum_{k=0}^{N-1} \gamma^k g(x_k, \pi(x_k)) \right\} \quad (2.6)$$

where $g(x_k, \pi(x_k))$ represents the instantaneous cost function, $0 < \gamma < 1$ is the discount factor, and $J_{\pi}(x_0)$ is the expected cost or the cost-to-go function when the system starts at state x_0 and follows the control policy π thereafter [82]. By solving this infinite horizon optimization problem, the time-invariant control policy is obtained.

The SDP algorithm is also applied in PHEV power management problem with the objective to minimize both the fuel and electricity cost in a PHEV [86]. Similar to [82], a Markov model of the power demand is built based on a finite number of power demand and vehicle speed samples from standard drive cycles. After that, the SDP approach begins with a discretization of the admissible state and control input sets. Given the discrete-valued state variable sets, a policy iteration algorithm is applied to compute the optimal power management cost function and policy. This algorithm consists of two successive steps, namely, policy evaluation and policy improvement. For each possible state, the policy evaluation step approximates the corresponding cost-to-go function over a stochastic distribution of drive cycles starting at that state, given a control policy. The policy improvement step then finds a new optimal control policy by minimizing the cost-to-go function value with respect to this policy for each possible state. This process iterates until a convergence criterion is satisfied. The policy evaluation and policy improvement steps are presented in details in [86] [87].

Based on the above discussion of the SDP approach, it can be concluded that SDP is not a real-time solution by its nature. The SDP methods are appealing because of their ability to optimize a power split problem for a probabilistic distribution of drive cycles, rather than a single specific cycle. To obtain the a probabilistic distribution of the power demand, the power demand and vehicle speed or other related state variables are discretized. The discretization makes the problem amenable to computer calculations, but generally produces suboptimal results of the power split control policy [86]. The obtained time-invariant control policy could be directly used in real-time implementations [88].

One main drawback of the SDP based methods is their well-recognized computational complexity [72]. Another drawback is that to construct the Markov model for the power demand, a large set of drive cycles are required to obtain the enough data. If the data set is not rich enough to cover the whole state space, the transition probability may be zero, which will affect the control policy. The computed control policy is represented as a large table of state-action pairs and is only defined for states that were previously observed in the dataset, while it is desired to construct a more general energy management strategy that can be applied to a wider range of driving scenarios. In addition, there may be storage memory problem with the SDP control policy implementation. The generated control policy from SDP is usually a n -D (dimensional) static mapping that states the control decision to be delivered at given states. Here, n is the number of the states in the SDP problem. In [89], a 4-D static mapping is generated based on the states of speed, acceleration, battery SoC and a binary state of the engine on-off state. The drawback of implementing such a 4-

D static mapping controller are mentioned in [89] as it is difficult to store such a large quantity of data in the commercial electronic controller unit (ECU) as the ECU storage memory is limited.

2.3.5 Model Predictive Control Based Control Strategy

Model Predictive Control (MPC) is a control methodology that computes an optimal control solution based on a model of a dynamical system and its predicted future evolution. The control objective and the dynamic system model are formulated as a real-time optimization problem that repeatedly computes the control inputs to the physical system. Only the computed control inputs associated with the current time step is actuated on the physical system. With new measurements of the physical system, a new state of the dynamic system is estimated and the real-time optimization procedure is repeated [47] [90] [91] [92] [93].

Borhan *et al.* applied MPC based control strategy for the first time to solve the energy management problem of power-split HEVs [94]. In their work, a nonlinear optimization problem is formulated over a future time window, during which the objective is to (1) minimize the fuel use to improve the fuel economy of the power-split HEV; (2) reduce service brake use, and (3) prevent over-charge and over-discharge of the battery. In this energy management problem, equality and inequality constraints should also be taken into account to maintain the engine, motor, generator, and the battery under normal operation. To reduce the computational cost of this nonlinear optimization problem, the nonlinear plant model (powertrain model) and the nonlinear constraints are linearized at each sample time. In this way, the nonlinear

optimization problem is reduced to a quadratic optimization problem for which efficient real-time solutions may exist. The solution to this nonlinear optimization problem determines the power demand distribution between the ICE and the electric motor/generator. It is demonstrated that the fuel economies achieved with this proposed MPC based control strategy outperforms that reported by the rule-based energy management strategy used in PSAT simulation software [94].

To analyze the potential benefits of integrating UC in the ESS unit of a power-split HEV, Borhan *et al.* proposed the work in [95] to develop a MPC controller for the power split among battery, UC and ICE. Different from the work in [94], the number of states is increased by one as the UC is added in the system. In addition, the number of degrees of freedom is increased as the power split factor of ESS has increased by one dimension. Similar approach to [94] is employed in this work for online linearization of the nonlinear plant model around the current operation conditions. The linear MPC is applied to find the control inputs to the plant model.

In this paper [95], the plant model of a power-split HEV with an UC and battery is developed. Then, based on the optimization objectives of minimizing the fuel consumption and also reducing the battery high peak power, an online supervisory controller based on MPC is constructed. With both the plant and controller model, a closed-loop model of the system is developed and simulated, which shows that combining battery and UC can reduce the battery discharge intensity to extend the battery life.

In the MPC based control strategy applied in [94] [95], the optimization is solved over a future prediction horizon of 5 seconds. With this short prediction horizon, it is

likely to make short-sighted decisions. However, with a long prediction horizon, the solution of the optimal control problem may require high computation effort. In addition, the driving cycle information over long time horizons is not generally known in the real-time driving conditions. Usually, the future load demand is assumed to be constant or to be exponentially decreasing over the prediction horizon.

In view of these problems, Borhan *et al.* [96] reformulated this MPC fuel minimization problem to include not only the finite horizon cost of fuel but also an approximate cost-to-go beyond the planning horizon represented as a terminal cost in the optimization problem. This proposed approach is based on breaking the fuel cost for an entire trip into a receding horizon stage cost and an approximation of the minimum cost-to-go cost as a function of battery SoC. With the breakdown to a short-horizon, the updated MPC problem is solved by DP over the prediction horizon. Thus, the fuel minimization problem is solved in real-time while considering the nonlinearities in both the plant model (the powertrain model) and the constraints. Based on the simulation results, it is concluded that with this new approach, the fuel economy of a power-split HEV is improved noticeably in comparison to the MPC controller developed in [94]. However, for this reformulated MPC problem, the optimal solution is dependent on the design of the terminal cost function.

MPC based control strategies have been applied to the battery-UC HESS power split problems in [97] [98]. In [98], a multi-objective optimization problem is formulated to (1) minimize the battery current variations and (2) minimize the UC voltage deviation from a reference voltage. By adding the second objective, it helps to maintain the UC voltage around the required reference value to avoid the UC from

over-charge or over-discharge. This is a similar approach as presented in [96] with adding a terminal cost. The value of the reference voltage and the trade-off factors between the two objectives have to be chosen carefully to achieve good results. To solve this optimization problem formulated in [98], similar approach in [94] [95] has been applied to linearize the nonlinear plant model around each operating point. The proposed MPC based energy management control strategy has been experimentally verified for a hybrid battery-UC power source.

For the MPC based energy management control strategies in [94] - [98], it is shown that it has the potential to be real-time implementable. To prevent the computational cost of a nonlinear optimization problem, the nonlinear constraints and models are linearized at each sample time, which may compromise the model accuracy [94] [95]. Another problem with MPC based control strategy is that one need to choose the appropriate prediction horizon: a MPC problem with short prediction horizon may result in shortsighted decisions while a MPC problem with long prediction horizon may be computationally demanding. One possible solution to this problem is adding a terminal cost function [96] [98]. However, the design of the terminal cost function depends on heuristics or empiric experience.

2.3.6 Instantaneous Optimization Based Control Strategy

For energy management approaches, it is desired to have accurate predicted information of the future power demand and trip information. However, it is not easy to acquire the accurate power demand profiles in advance because the vehicle movement relies on many factors, such as the traffic on the road or the driving pattern

of driver. To solve an energy management problem with no future operating information available, Choi *et al.* [99] [100] [101] formulate an instantaneous optimization problem for a battery-UC HESS power split problem. The optimal power split between the battery and UC is computed at each instant.

In order to utilize the UC efficiently, the UC should be charged or discharged properly. For example, the UC SoC needs to be high before the electric machine requires a large propulsion power. Otherwise, the UC may not provide the requested peak power. It is also desired to set the UC SoC at a relatively low value before there is regenerative braking. Otherwise, the UC may not receive or recover the regenerative braking energy properly. As it is hard to expect the future power demand profile, a simple strategy [100] is used to adjust the UC SoC according to the vehicle speed (denoted as v_s): When v_s is high, UC should be operated in a low SoC range in order to capture the regenerative braking energy as much as possible. On the contrary, the UC SoC needs to be high if the vehicle speed v_s is low because an electric machine may require a large peak power for future accelerations when the vehicle is at low speed. Especially, the electric machine usually requires a large power when the vehicle speed increases from zero. Thus, a reference UC voltage V_{uc}^{ref} is adjusted using the following equation.

$$V_{uc,ref} = \frac{V_{uc,min} - V_{uc,max}}{v_{s,max}} v_s + V_{uc,max} \quad (2.7)$$

where $V_{uc,min}$ and $V_{uc,max}$ are the boundary of the UC voltage values and $v_{s,max}$ is the maximum vehicle speed. The UC reference voltage is repeatedly computed and

updated according to the real-time vehicle speed. This UC reference voltage value is used in the instantaneous optimization problem as a given parameter. In the proposed optimization problem, the objective function is to minimize a sum of the battery current magnitude, the battery current fluctuation and the difference or gap between the UC voltage and the corresponding reference voltage value. In [99], a convex optimization problem is formulated, which can be repeatedly computed by general solvers in polynomial time.

The advantage of this instantaneous optimization based control strategy is that it does not depend on the future vehicle operating profile. However, to ensure that UC can provide or receive sufficient power at each instant, the UC reference voltage is set based on experience, which is not guaranteed to be optimal.

2.3.7 Neural Networks Based Control Strategy

NN has the capacity to represent or emulate human knowledge and take intelligent decisions. The NNs have been widely applied to system identification, process control, prediction, diagnosis, etc [42].

An efficient energy management system for HEV, using NNs is developed and tested in [42]. In this work, an auxiliary energy system (AES) is used in an HEV to receive regeneration and give peak power during high acceleration periods. The use of AES allows using energy systems (gas turbines, fuel cells, etc.) with lower power ratings or with power ratings that close to the average power consumption. In the AES adopted in [42], batteries are used as the "main source" while UCs are used as the "auxiliary source". It is essential to develop an energy management system to

control the power flow between these two sources. An optimization problem is formulated to minimize the battery discharge. A numerical solution to this optimization problem is derived to find the optimal path for the UC current. In order to obtain a simple implementation of the control strategy, in real-time, NN is utilized on system identification to approximate the optimization function of the UC current. As a first step to built the NN, various city drive datasets are resolved based on the optimal control obtained from numerical solutions, generating the required input and output data for NN training. The current demand and power demand of the AES are used as the NN input, together with the vehicle speed and the kinetic energy. The data output of the NN is the ideal UC current output. The trained NN is implemented and tested using an urban test course. It is shown that the AES, using the optimal control implemented with NNs, can improve the system efficiency.

NN is also applied to learn the energy management optimization with specific roadway types and traffic congestion levels in [102] [103]. In this work, NNs are trained to predict the roadway type and traffic congestion levels. Different NNs are trained to predict driving trends and to learn the optimal engine speed and optimal battery power command.

First of all, 11 standard drive cycles, called facility-specific (FS) cycles, are used as the standard measure of roadway type and traffic congestion levels. These cycles represent passenger car and light truck operations over a broad range of facilities and congestion levels in urban areas. A multilayered and multiclass NN, for the prediction of roadway types and traffic congestion levels is constructed and trained using these

FS cycle data. The output of this NN is the predicted roadway type and traffic congestion level.

Another NN is developed for predicting the driving trend at any given time step. The NN is trained based on the average speed, maximum speed, minimum speed, average acceleration during a past time period window. The vehicle speed at the start and end point of this past time period window is also used as the NN input. The output of the NN is the vehicle driving trend, which is defined into five classes: "No Speed", "Low Speed Cruise", "High Speed Cruise", "Acceleration" and "Deceleration". With this NN, the driving trend can be obtained based on the driving history data.

The next step is to construct an NN to learn the optimal power split results. In this work, the optimal power split between the battery and engine is obtained for each FS cycle, with the optimal power split and settings associated with each specific roadway type and traffic congestion level. The optimal sequence of the two control variables, i.e., engine speed and the battery power are used as the training data for NNs. Two sets of NN ($NN_{\omega_{eng}}^i$, $NN_{P_{bat}}^i$) are developed to learn the engine speed and the battery power respectively, for each of the 11 FS cycle roadway type and congestion levels with $i = 1, 2, \dots, 11$. $NN_{P_{bat}}^i$ is used to predict the battery power with the NN inputs of vehicle speed, driving trend, battery SoC, and the total power demand. $NN_{\omega_{eng}}^i$ is used to predict the optimal engine speed with the input of vehicle speed, battery SoC and the total power demand. Based on these NNs, an intelligent online power controller is developed and presented in [103].

In addition, NN based method is applied in similar energy management problems [37] [43] [104] for vehicle applications to obtain the real-time implementation of the power split control strategies. The use of NN in energy management problem is very efficient and effective for real-time implementations.

The pros and cons of the main energy management strategies have been summarized in Table 2.2.

Table 2. 2 Characteristics of Energy Management Control Strategies.

Energy Management	Advantages	Disadvantages	References
Rule-based	(1) Simple implementation (2) Computational efficiency (3) Real-time implementable	(1) Dependent on heuristics (2) Do not provide optimal control	[60] [61]
Fuzzy logic	(1) Robust and good with model uncertainties and state variations (2) Real-time implementable	(1) Dependent on heuristics (2) Do not provide optimal control	[66] [67] [68]
Dynamic programming	(1) Guarantees the global optimal solution for energy management optimization problem	(1) DP is not real-time implementable.	[74] [81]
Stochastic Dynamic Programming	(1) Generate a time-invariant control policy. (2) Has ability to optimize a	(1) state-action pairs are only defined for states that were previously	[82] [83] [84] [85]

	power split problem for a probabilistic distribution of drive cycles, rather than a single specific cycle.	observed. (2) May have memory storage issues for SDP implementations.
Model predictive control	(1) Has potential for real-time implementations; (2) Easy to handle constraints directly in the design procedure.	(1) May compromise model accuracy by using linearized model. (2) May need large memory for heavy computations
Neural networks	(1) Robust responses to new input information and different load demand profiles (2) Real-time implementable	(1) Require proper training input and a proper training procedure in the neural network design (2) It does not guarantee optimality.

2.4 Summary

In this chapter, the main HESS topologies have been discussed and compared comprehensively for the battery-UC HESS applications. The HESS sizing methodologies are introduced and discussed. It is concluded that the interdependence between the energy management control strategy and the sizing of different energy sources should be taken into account.

The energy management strategies for hybrid energy systems have been extensively discussed and classified into seven main categories, including rule-based methods, fuzzy logic methods, global optimization, stochastic dynamic programming, model predictive control, instantaneous optimization and neural network based methods. The advantage and disadvantage of each energy management control strategy is discussed.

Chapter 3: Optimal Sizing of a Battery-UC Hybrid Energy Storage System for EV applications

This chapter targets the interdependence between sizing and power split optimization of HESS in EVs. In particular, a high energy density battery with an UC hybrid system is investigated as a benchmark. A convex optimization problem is formulated to optimize the power split between battery and UC offline. Based on this simplified power split optimization, a HESS sizing optimization problem is developed to minimize the HESS weight and to fulfil the EV specifications of driving range and acceleration time. It shows that the benefit of size/weight reduction is more effective for EV with relatively low or median range. For EV with extended driving range, the improvement of acceleration time is more impressive using the battery-UC HESS.

This chapter is organized as follows: in Section 3.1, the HESS power split optimization is formulated as a convex optimization problem; in Section 3.2, the interdependence between sizing and power split optimization is investigated and a comprehensive sizing analysis is conducted. Furthermore, HESS sizing for EV with different specifications is discussed. Finally, the contribution of this work is summarized in Section 3.3.

3.1 HESS Power Split Optimization

UC packs can supply the high power demand to alleviate the stress on battery packs and contribute to battery life extension. To explore the maximum benefit of a HESS, an optimization-based power split problem is formulated as described below.

The objective of power split is to share the load power demand into the battery power and the UC power. To achieve the optimization objective, the power split is designed to reduce the overall battery power magnitude and to avoid high peak charging/discharging power to/from the battery. The battery cycle life can be extended due to the reduced battery current rate.

3.1.1 Problem Formulation for the Power Split Optimization

An offline optimization problem is formulated based on specific driving cycles. The load power demand schedule $\{P_{dmd}(k), k = 1, 2, \dots, N\}$ is discretized with the sampling time of $\Delta T = 1$ second. At each time step k , the sum of the instantaneous battery and UC power equals to the load power demand.

$$P_{bat}(k) + P_{uc}(k) = P_{dmd}(k), \quad k = 1, 2, \dots, N \quad (3.1)$$

The UC energy is related to UC power as shown in Eq. (3.2).

$$E_{uc}(k+1) - E_{uc}(k) = -P_{uc}(k)\Delta T, \quad k = 1, 2, \dots, N \quad (3.2)$$

Note that $P_{uc}(k)$ is the instantaneous UC output power at time step k . It is assumed that the discharging power is positive and the charging power is negative. It is also assumed that $P_{uc}(k)$ remains constant from time step $k\Delta T$ to $(k+1)\Delta T$.

The UC energy is related with the UC voltage as,

$$E_{uc}(k) = \frac{1}{2} C V_{uc}^2(k), \quad k = 1, 2, \dots, N \quad (3.3)$$

where, C is the equivalent UC pack capacitance.

The UC energy storage is constrained by its maximum storable energy limits $E_{uc,max}$ and the minimum allowable energy $E_{uc,min}$, as shown in Eq. (3.4).

$$E_{uc,min} \leq E_{uc}(k) \leq E_{uc,max}, \quad k = 1, 2, \dots, N \quad (3.4)$$

Thus, $E_{uc}(k) - E_{uc,min}$ is the usable energy from UC at time step k .

Given the number of UC cells, the initial energy in a UC is given as a constant value of E_{init} .

$$E_{uc}(1) = E_{init} \quad (3.5)$$

To ensure a successful power split, the instantaneous UC power is limited by its maximum discharging and charging power at each time step k , as in Eq. (3.6).

$$P_{uc,min}(k) \leq P_{uc}(k) \leq P_{uc,max}(k), \quad k = 1, 2, \dots, N \quad (3.6)$$

If the UC internal resistance is neglected in an ideal condition, the UC max discharging/charging power can be expressed by Eq. (3.7) and Eq. (3.8).

$$P_{uc,max} = V_{uc} I_{uc,max} \quad (3.7)$$

$$P_{uc,min} = V_{uc} I_{uc,min} \quad (3.8)$$

$I_{uc,max} (>0)$ is the maximum discharging current that can be delivered by UC and $I_{uc,min}$ (<0) is the maximum charging current. The maximum discharging/charging currents are determined by the UC characteristics [106].

The decision variable in this optimization problem is the UC power vector $P_{uc} \in R^N$. A quadratic function of the decision variable is designed as the objective function, shown in Eq. (3.9).

$$f_0(P_{uc}) = \|P_{dmd} - P_{uc}\|_2^2 \quad (3.9)$$

The power split optimization problem is formulated as below.

$$\underset{P_{uc} \in R^N}{\text{Minimize}} \quad f_0(P_{uc}) \quad (3.10)$$

s.t.

$$E_{uc} = E_{init} + B^T P_{uc} \quad (3.11)$$

$$E_{uc,min} \leq E_{uc}(k) \leq E_{uc,max}, \quad k = 1, 2, \dots, N \quad (3.12)$$

$$P_{uc}(k) \leq I_{uc,max} \sqrt{2E_{uc}(k)/C}, \quad k = 1, 2, \dots, N \quad (3.13)$$

$$P_{uc}(k) \geq I_{uc,min} \sqrt{2E_{uc}(k)/C}, \quad k = 1, 2, \dots, N \quad (3.14)$$

where, $B^T \in R^{(N+1) \times N}$ is a given constant matrix. Eq. (3.11) computes the UC energy $E_{uc} \in R^{N+1}$ over the horizon of a given drive cycle. The constraint functions in Eq. (3.12) limit UC energy storage within an usable range. The last two constraints limit the UC power by its physical limitations.

3.1.2 Convex Optimization

The objective function in Eq. (3.9) is a quadratic convex function. The first equality constraint is linear (affine) and the second constraint is a linear inequality equation. The last two inequality constraints are convex with their second-order derivative on P_{uc} always positive. Thus, the problem formulation as shown in Eq. (3.10) - Eq. (3.14) is a convex optimization problem. This problem can be solved efficiently using the MATLAB software CVX [107] [108]. Despite its simple formulation, this optimization problem provides effective power split which can result in battery power reduction and peak shaving.

3.2 HESS Sizing Optimization and Analysis

The HESS sizing optimization problem is to find an optimal combination of (N_{bat} , N_{uc}) to minimize the HESS weight and to fulfill all the EV specifications in terms of range, acceleration time, etc. With an increasing number of UC cells, the benefit of battery power shaving can be enhanced in tradeoff with the increased HESS weight. In order to make a comprehensive comparison, the battery-only ESS is analyzed first with the assumption of $N_{uc} = 0$.

3.2.1 Battery-only ESS Sizing Optimization

The battery-only ESS sizing optimization problem is formulated in Eq. (3.15) – Eq. (3.19). In a battery-only ESS, the battery pack is directly connected to DC bus with the input voltage range from $V_{dc,min}$ to $V_{dc,max}$. This voltage range constrains the battery pack terminal voltage that is dependent on the number of series-connected battery cells $N_{b,ser}$, in Eq. (3.16) and Eq. (3.17).

The sizing optimization problem is formulated to minimize the number of battery cells that can satisfy the transient power requirements and the energy needs imposed by range requirements, as given in Eq. (3.18) and Eq. (3.19). The maximum storable energy in one battery cell is denoted as $E_{b,cell}$. The maximum discharge power of batteries and UC cells are denoted as $P_{b,cell,max}$ and $P_{uc,cell,max}$.

$$\underset{N_{bat} \in \mathbb{Z}_+}{\text{Minimize}} \quad N_{bat} \cdot m_{b,cell} \quad (3.15)$$

s.t.

$$N_{bat,ser} V_{bat} \geq V_{dc,min} \quad (3.16)$$

$$N_{bat,ser} V_{bat} \leq V_{dc,max} \quad (3.17)$$

$$N_{bat} P_{b,cell,max} \geq P_{dmd}(k), \quad k = 1, 2, \dots, N \quad (3.18)$$

$$N_{bat} E_{b,cell} \geq \sum_k P_{dmd}(k), \quad k = 1, 2, \dots, N \quad (3.19)$$

Fig. 3.1 shows the optimal sizing result for high energy density and high power density battery-only ESS under UDDS drive cycles for different range specifications. To deliver the same range, it requires a much larger number of high power density batteries in comparison to the high energy density batteries due to their different energy densities.

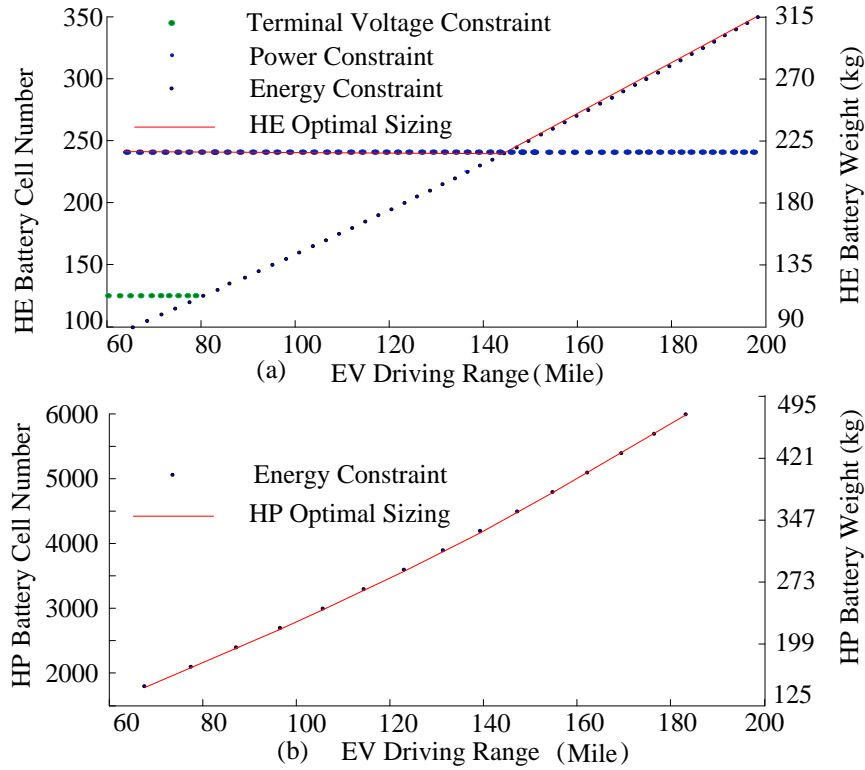


Figure 3.1 (a) High energy density battery-only ESS optimal sizing; (b) High Power battery-only ESS optimal sizing.

As shown in Fig. 3.1(a), the power and energy constraints give different lower bounds on the high energy density battery cell number. For an EV with all electric range less than 140 miles, oversized high energy density batteries are used to satisfy the power requirements. In this case, there is a chance to reduce the battery size by hybridizing them with UCs, which can lower the load power requirement on batteries. With the optimal power split, this load power requirement on batteries can be reduced. Thus, the number of battery cells can be reduced.

Notice that UDDS drive cycle with a high percentage of regenerative braking is considered in this simulation case. Therefore, the energy storage requirement on battery may be underestimated in this sizing analysis.

3.2.2 Battery-UC HESS Sizing Optimization

3.2.2.1 HESS Sizing Optimization (Case 1: EV range \leq 140 Miles)

Similar to the battery-only ESS sizing problem, the HESS sizing optimization problem is formulated to minimize the HESS weight, in Eq. (3.20) - Eq. (3.23).

$$\underset{N_{bat}, N_{uc} \in \mathbb{Z}_+}{\text{Minimize}} \quad J_m(N_{bat}, N_{uc}) = N_{bat} \cdot m_{b,cell} + N_{uc} \cdot m_{uc,cell} \quad (3.20)$$

s.t.

$$N_{bat} P_{b,cell,max} \geq P_{bat}(k), \quad k = 1, 2, \dots, N \quad (3.21)$$

$$N_{uc} P_{uc,cell,max} \geq P_{uc}(k), \quad k = 1, 2, \dots, N \quad (3.22)$$

$$N_{bat} E_{b,cell} \geq \sum_k P_{dmd}(k), \quad k = 1, 2, \dots, N \quad (3.23)$$

where, $P_{bat}(k)$ and $P_{uc}(k)$ are determined by the optimal power split.

In this case, the battery power reduction and peak shaving effect is influenced by the number of UC cells. A combined HESS sizing and power split optimization objective can be defined to find the pareto points between $J_m(N_{bat}, N_{uc})$ and $f_0(P_{uc})$ as shown in Fig. 3.2. In this case, a 160 battery cells are used with the energy storage of 22.4kWh which can provide a low to median driving range. Different number of UC cells are integrated into the ESS.

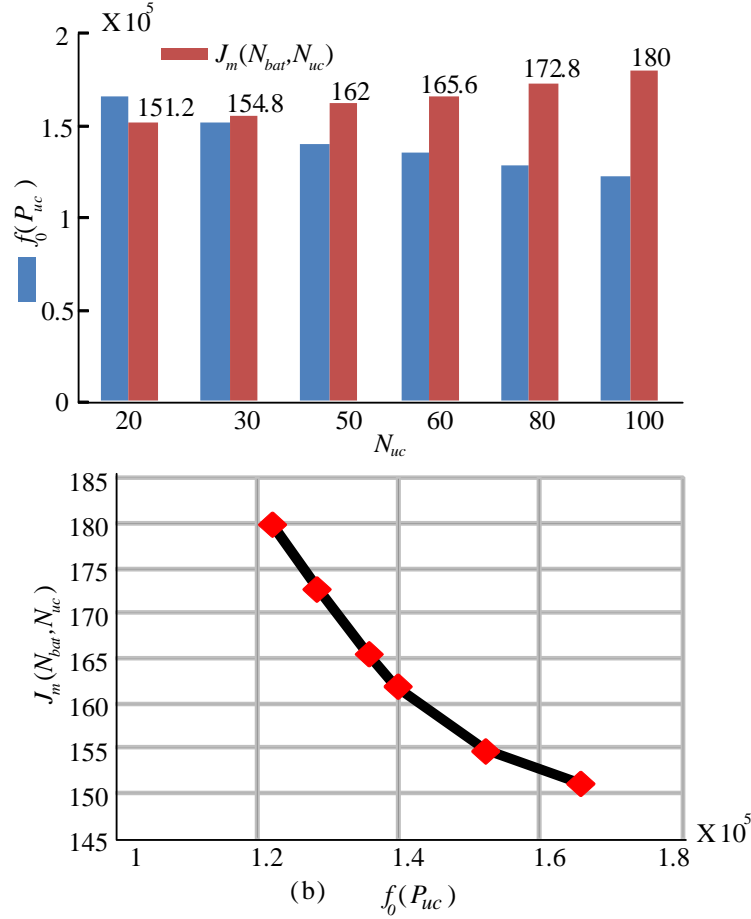


Figure 3.2 (a) Values of $J_m(N_{bat}, N_{uc})$ and $f_0(P_{uc})$; (b) Pareto points.

Fig. 3.2(a) shows that an increasing number of UC cells results in a larger HESS weight $J_m(N_{bat}, N_{uc})$ and a lower value of the power split objective function $f_0(P_{uc})$. Notice that the total weight of the battery-UC HESS in a real vehicle will be much heavier than the result of $J_m(N_{bat}, N_{uc})$ as a packing factor over 1.5 is reasonable in realistic situations.

Fig. 3.2(b) plots the pareto frontiers in objective function domain to show the trade-offs between HESS sizing and power split objective. Based on the results, the EV manufacturers can make decisions on how to achieve the best trade-offs between

the battery-UC weight and the power split goals of the battery peak shaving, according to different EV design requirements.

3.2.2.2 HESS Sizing Optimization (Case 2: EV range>140Miles)

For EVs with high AER specifications, a HESS shows no advantage in weight reduction since a large number of batteries are always required to deliver such a long driving range. To explore the benefit of HESS for high range EV, the AER and power performance (acceleration time) at different combinations of (N_{bat}, N_{uc}) are discussed.

The EV acceleration time from 0 to 60mph is evaluated with the assumption that HESS delivers a continuous power at its maximum power value during the acceleration time. This maximum continuous power is dependent on the number of battery and UC cells as the more energy storage components and power sources, the more propulsion power can be provided by the vehicle. With more energy storage components, the vehicle mass is also increased. Thus, a heavier vehicle will have a larger power requirement when the vehicle is accelerated to the same target speed.

In this work, a midsize EV model from the Autonomie software is used [109]. The sizing influence on the EV range and its acceleration time from 0 to 60mph is investigated. Given a combination of (N_{bat}, N_{uc}) , the corresponding range and acceleration time are estimated. The estimation results are shown in Fig. 3.3.

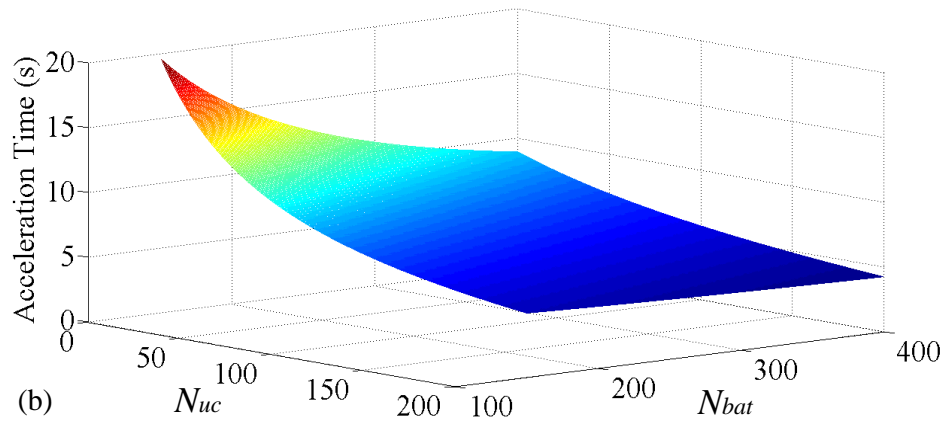
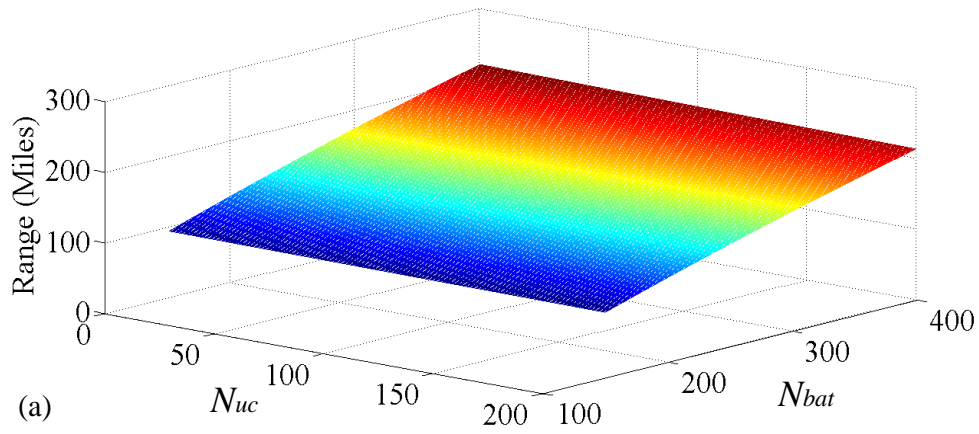


Figure 3.3 (a) EV Range vs. (N_{bat}, N_{uc}) ; (b) Acceleration time vs. (N_{bat}, N_{uc}) .

Based on Fig. 3.3, the optimal HESS sizing for EV with specific range and acceleration time can be determined. For example, to build a high performance EV with AER of 160 miles and acceleration time within 6.5s, two horizontal planes at 160 miles range and 6.5s acceleration time are set to form intersections with the plots and determine the feasible region of (N_{bat}, N_{uc}) . The optimal HESS sizing is attained when $J_m(N_{bat}, N_{uc})$ reaches the minimal value in this feasible region. For these particular EV specifications, the optimal HESS sizing is achieved at $(N_{bat}=275, N_{uc}=101)$ with the minimal battery/UC cell weight of $J_m(N_{bat}, N_{uc})=283.86\text{kg}$.

In light of this analysis, the HESS optimal sizing are determined for different EV specifications with ranges from 100 to 220 miles and acceleration times from 6 s to 10 s. The optimal HESS weight (only the weight of the battery and UC cells) is shown in Fig. 3.4. The optimal combination of (N_{bat}, N_{uc}) is given in Fig. 3.5.

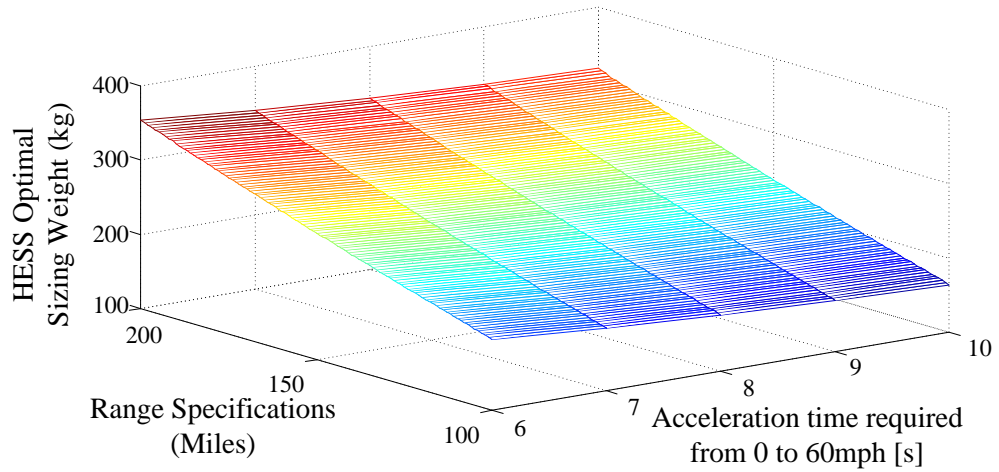
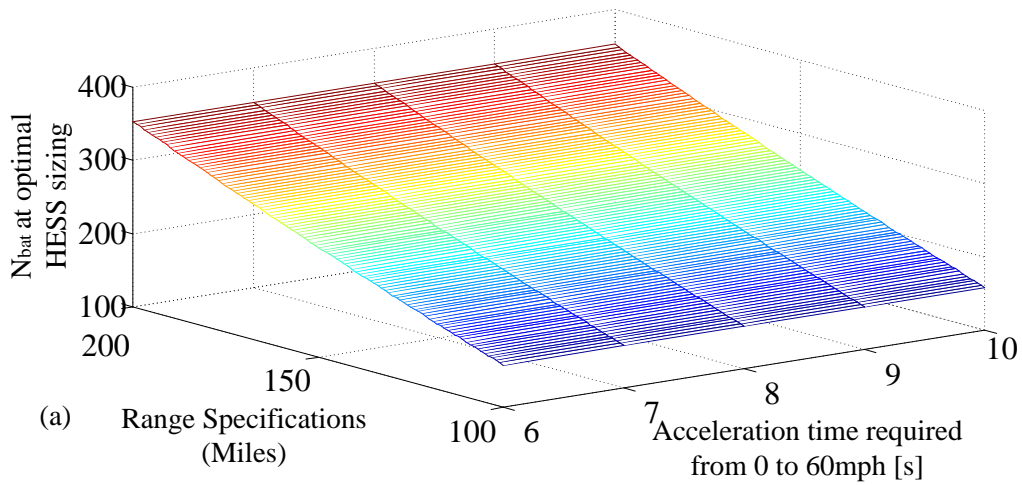


Figure 3.4 HESS optimal sizing at different range / acceleration time specifications.



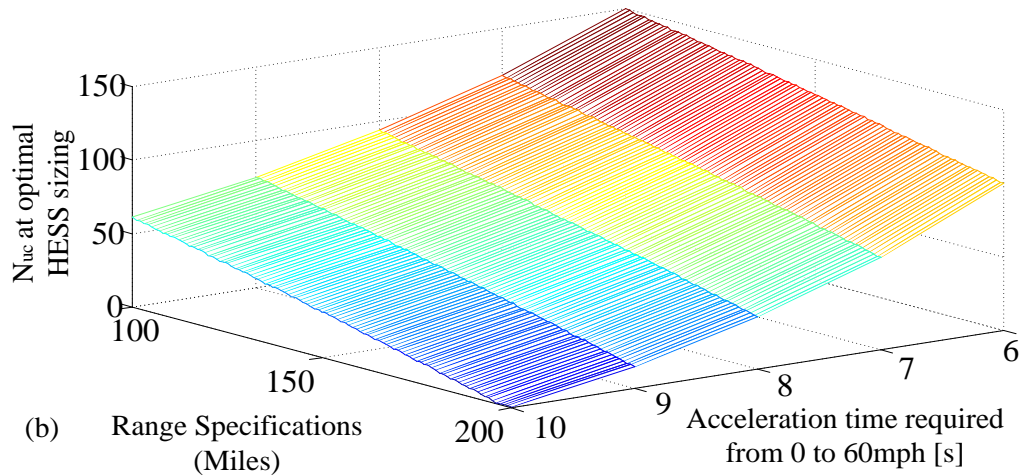


Figure 3.5 (a) N_{bat} at optimal HESS sizing; (b) N_{uc} at optimal HESS sizing.

Fig. 3.5 reveals the simulation results for HESS optimal sizing design. A smaller energy storage system has less power for vehicle acceleration. Therefore, it requires a longer period of acceleration time to reach the target speed. With a more strict specification on acceleration time, it requires more UC cells. Thus, for EVs with large range and small acceleration time specifications, a HESS with a large UC pack shows benefits in sizing optimization [110].

3.3 Summary

In this chapter, an ESS sizing problem and a convex optimization-based power split problem are combined and investigated. The results show that the hybridization of UCs with high energy density batteries can achieve high power capabilities and large energy storage at the same time with smaller size and weight in comparison to the high power density battery-only ESS counterpart. This chapter also reveals that the benefit of size reduction by HESS is very effective for EVs with median driving ranges. For large range EVs, HESS provides good trade-offs between high driving

range and fast acceleration. In particular, for a high performance EV with strict specifications of acceleration time, more UC cells are required in a HESS for optimal sizing and improved power performance.

The main contribution of this chapter is to introduce a systematic approach to optimize the HESS sizing which takes the interdependence between the HESS energy management and sizing into account. Following this systematic approach, the HESS design can be evaluated in terms of the sizing and the power split objectives simultaneously. This HESS sizing approach can be adapted to different optimization objectives, vehicle models, HESS energy management strategies and design variables.

Chapter 4: A Supervisory Energy Management Control Strategy in a Battery-Ultracapacitor Hybrid Energy Storage System

One of the major challenges in a battery-UC HESS is to design a supervisory controller for real-time implementation that can yield good power split performance. This chapter presents the design of a supervisory energy management strategy that optimally addresses this issue. In this work, a multi-objective optimization problem is formulated to optimize the power split in order to prolong the battery lifetime and to reduce the HESS power losses. In this HESS energy management problem, a detailed DC-DC converter model is considered to include both the conduction losses and the switching losses. The optimization problem is numerically solved for standard drive cycle datasets using DP. Trained using the DP results, an effective and intelligent online implementation of the optimal power split is realized based on neural networks. The proposed online intelligent energy management controller is applied to a midsize EV. The proposed online energy management controller effectively splits the load demand and achieves excellent result of the system efficiency. It is also estimated that the proposed online energy management controller can extend the battery life by over 60% under New York drive cycle as the daily commute assumptions, which greatly outperforms rule-based control strategies.

In this chapter, Section 4.1 provides a system-level model of HESS, including the efficiency model of the bi-directional DC-DC converter that interfaces the UC pack with the battery pack. A multi-objective optimization problem is formulated in Section 4.2 and solved using DP. Section 4.3 presents the developed NN for the

online energy management. The battery SoH improvement of both the offline and online optimization results are evaluated in Section 4.4. Finally, this chapter is summarized in Section 4.5.

4.1 HESS Model

This section describes the models used in the HESS including the battery pack, the UC pack and the bi-directional DC-DC converter. The propulsion machine and inverter group is modeled as a current source connected to its DC bus, which draws the current determined by the drive cycle profiles. In this work, we use the drive cycle information from the Autonomie software developed by Argonne National Lab.

In the designed HESS, a bi-directional DC-DC converter is used to interface the UC to the DC bus. Different HESS topologies have been discussed extensively in [6] [32]. In this work, we adopt the topology of Fig. 4.1.

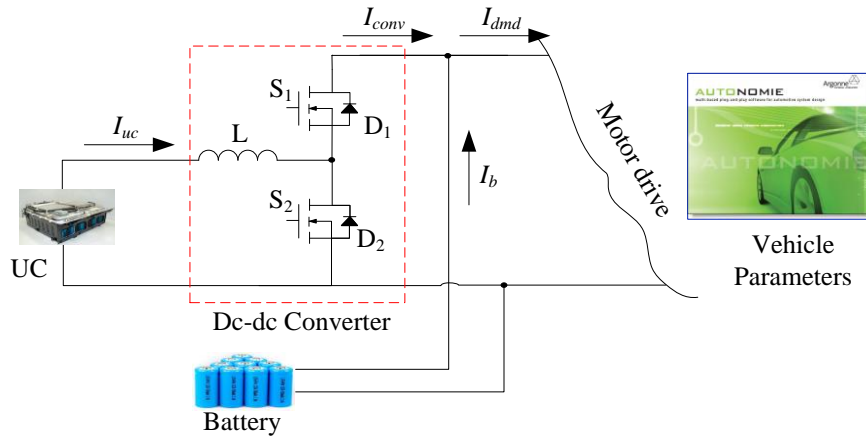


Figure 4.1 Bi-directional DC-DC converter in the HESS.

This bi-directional DC-DC converter is composed of an inductor L , two power MOSFETs S_1 and S_2 , and two body diodes D_1 and D_2 . The low-side voltage of the

DC-DC converter is equal to the UC voltage V_{uc} ; and the high-side voltage is the battery voltage V_b . Decoupled from the DC bus, the UC voltage can swing in a wider range; thus, it can improve the utilization of UC.

The circuit models of the HESS components are shown in Fig. 4.2. The following sections describe the HESS modeling based on these circuit models.

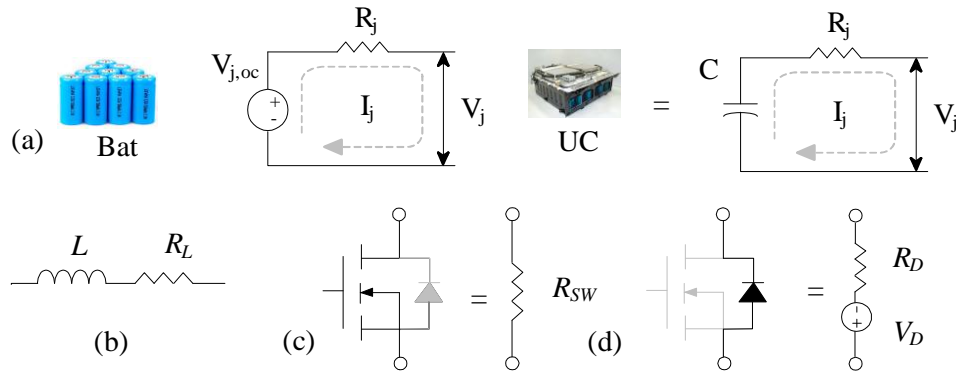


Figure 4.2 The model of (a) battery/UC; (b) inductor; (c) MOSFET; (d) body diode.

4.1.1 Battery/UC Model

The battery/UC circuit model is shown in Fig. 4.2(a). The voltage source $V_{j,oc}$ represents the open-circuit voltage for battery/UC and R_j is the internal resistance, with $j = \{b, uc\}$. In this work, the battery open-circuit voltage $V_{b,oc}$ is assumed constant during one drive cycle. This is because the battery has a flat discharge curve in the usable discharge range from 90% SoC to 30% SoC. This work uses a pack of K2 Energy battery cells with the energy storage of 34kWh. One hundred BCAP 2000 UC cell from Maxwell Technology are connected in serial as the UC pack of 203Wh energy storage. This 34kWh battery pack weights 324kg and the UC pack weights 36kg. The battery pack volume is 145 Liter while the UC pack is 29.2Liter. Given a

packing factor of 1.4, the total mass of the battery-UC HESS is 504kg with 244Liter volume. The battery and UC cell characteristics are listed in Table 4.1.

Table 4.1 Battery and UC cell characteristics.

Specifications	Battery	UC
Nominal voltage (V)	3.2	2.7
Nominal capacity (Ah)	2.6	N/A
Rated capacitance (F)	N/A	2000
Energy storage (Wh)	8.5	2.03
Weight (kg)	0.0805	0.36

4.1.2 Bi-directional DC-DC Converter Model

The bi-directional DC-DC converter works in two different operation modes, as Boost mode and Buck mode. The Boost and Buck operation modes are shown in Fig. 4.3 with the current direction indicated.

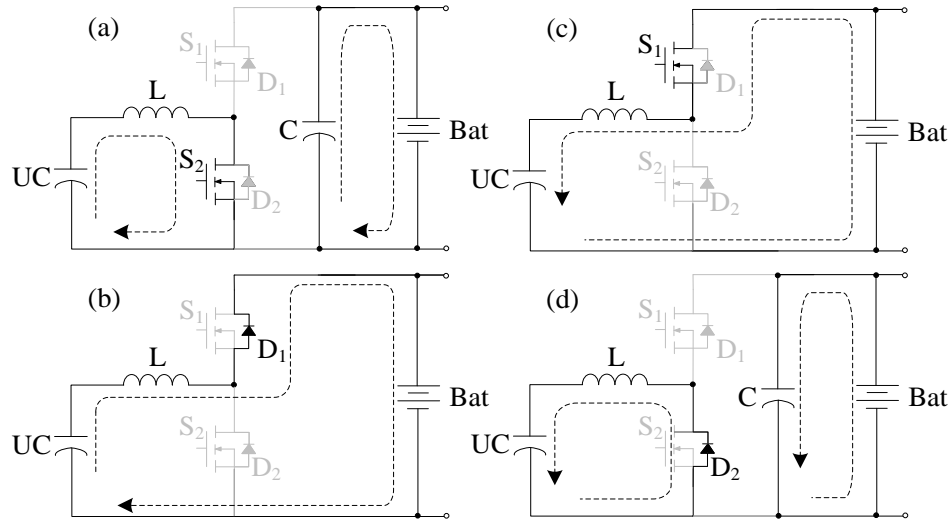


Figure 4.3 The DC-DC converter operation modes. (a) and (b) are in Boost mode, and (c) and (d) are in Buck mode. (a) S_2 is on and D_1 is off; (b) S_2 is off and D_1 is on; (c) S_1 is on and D_2 is off; (d) S_2 is on and D_2 is on.

In Boost mode, the bi-directional DC-DC converter transfers energy from UC to the DC bus by triggering the power MOSFET S_2 ; in Buck mode, the UC pack captures the regenerative braking energy from DC bus through bi-directional DC-DC converter by triggering the power MOSFET S_1 .

The equivalent circuit model of each component shown in Fig. 4.2. The inductance of the inductor is represented as L and the inductor winding resistance is represented by R_L . The inductor current is I_L , which is equal to the UC current I_{uc} . The MOSFET is modeled by the on-resistance R_{SW} in its conducting state as shown in Fig. 4.2(c). The body diode is modeled by a resistance R_D and a voltage source V_D representing the voltage drop across the forward-biased diode in its conducting state as shown in Fig. 4.2 (d). The output capacitance of the DC-DC converter is C and V_c

denotes the voltage across. With these circuit parasitic included, a state space average model is analyzed as below [111].

(1) Boost Mode of Operation:

The equivalent circuit model of the converter at boost mode of operation is shown in Fig. 4.4. When the gate drive signal of S_2 is high, S_2 turns on and the diode D_1 is reverse-biased. The equivalent circuit in this condition is shown in Fig. 4.4 (a).

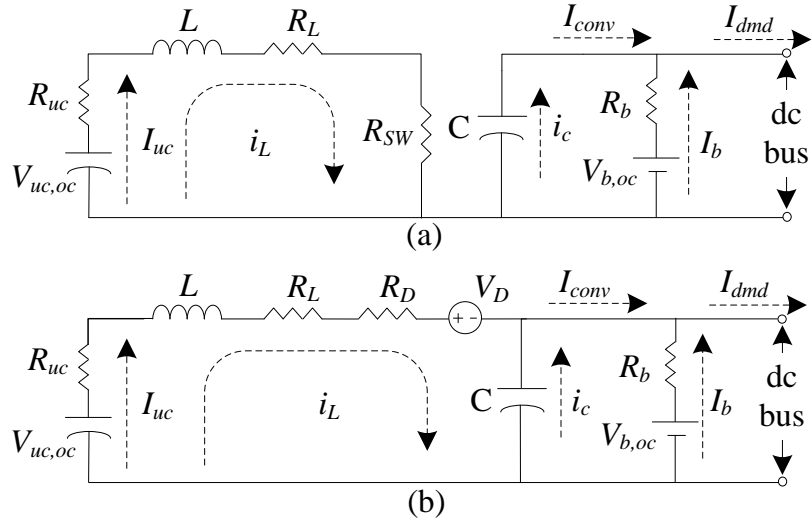


Figure 4.4 Boost Mode. (a) S_2 is on and D_1 is off; (b) S_2 is off and D_1 is on.

The steady state differential equation for the circuit of Fig. 4.4(a) is,

$$\begin{bmatrix} \frac{di_L}{dt} \\ \frac{dv_c}{dt} \end{bmatrix} = \begin{bmatrix} -\frac{(R_{uc} + R_L + R_{SW})}{L} & 0 \\ 0 & -\frac{1}{CR_b} \end{bmatrix} \begin{bmatrix} i_L \\ v_c \end{bmatrix} + \begin{bmatrix} \frac{1}{L} & 0 & 0 \\ 0 & \frac{1}{CR_b} & -\frac{1}{C} \end{bmatrix} \begin{bmatrix} V_{uc,oc} \\ V_{b,oc} \\ I_{dmd} \end{bmatrix} \quad (4.1)$$

When the gate signal of S_2 is low, S_2 turns off. The diode D_1 becomes forward-biased by the inductor current. The equivalent circuit is shown in Fig. 4.4(b). The differential equation for this circuit is,

$$\begin{aligned}
\begin{bmatrix} \frac{di_L}{dt} \\ \frac{dv_c}{dt} \end{bmatrix} &= \begin{bmatrix} -\frac{(R_{uc} + R_L + R_D)}{L} & -\frac{1}{L} \\ \frac{1}{C} & -\frac{1}{CR_b} \end{bmatrix} \begin{bmatrix} i_L \\ v_c \end{bmatrix} \\
&+ \begin{bmatrix} \frac{1}{L} & 0 & 0 \\ 0 & \frac{1}{CR_b} & -\frac{1}{C} \end{bmatrix} \begin{bmatrix} V_{uc,oc} \\ V_{b,oc} \\ I_{dmd} \end{bmatrix} + \begin{bmatrix} -\frac{1}{L}V_D \\ 0 \end{bmatrix}
\end{aligned} \tag{4.2}$$

For steady-state analysis, we have the inductor volt-balance equation and the capacitor charge balance equation as Eq. (4.3) and Eq. (4.4),

$$\int_0^{T_s} v_L(t) dt = 0 \tag{4.3}$$

$$\int_0^{T_s} i_c(t) dt = 0 \tag{4.4}$$

where, T_s is the switching period of the DC-DC converter, $v_L(t) = L \frac{di_L(t)}{dt}$ is the inductor voltage, $i_c(t)$ is the current in the output capacitor with $i_c(t) = C \frac{dv_c(t)}{dt}$.

Based on the inductor volt-balance equation and the capacitor charge balance equation, the average capacitor voltage V_c and the duty cycle D_{boost} of the DC-DC converter can be solved by integrating the Eq. (4.3) and Eq. (4.4) with state variable $X = \left\{ \frac{di_L}{dt}, \frac{dv_c}{dt} \right\}$ over one switching period, for the two switching intervals as $D_{boost}T_s$ and $(1-D_{boost})T_s$.

The obtained average capacitor voltage is,

$$V_c = V_{b,oc} + (1 - D_{boost}) R_b I_L - R_b I_{dmd} \tag{4.5}$$

Based on the capacitor charge balance equation, the relationship between the input and output currents is derived in Eq. (4.6),

$$I_{conv} = (1 - D_{boost}) I_L \quad (4.6)$$

The boost duty cycle D_{boost} , in the range of (0, 1), is then obtained by integrating the Eq. (4.4) over one switching period,

$$D_{boost} = \frac{V_{b,oc} + V_D - I_{dmd} R_b + I_L (R_D - R_{sw} + 2R_b) - \sqrt{\Delta_1}}{2I_L R_b} \quad (4.7)$$

$$\Delta_1 = \left(V_{b,oc} + V_D - I_{dmd} R_b + I_L (R_D - R_{sw} + 2R_b) \right)^2 - 4I_L R_b \left(I_L (R_D + R_L + R_{uc} + R_b) - V_{uc,oc} + V_{b,oc} - I_{dmd} R_b + V_D \right) \quad (4.8)$$

(2) Buck Mode of Operation:

The bi-directional DC-DC converter circuit model in Buck mode is shown in Fig.

4.5.

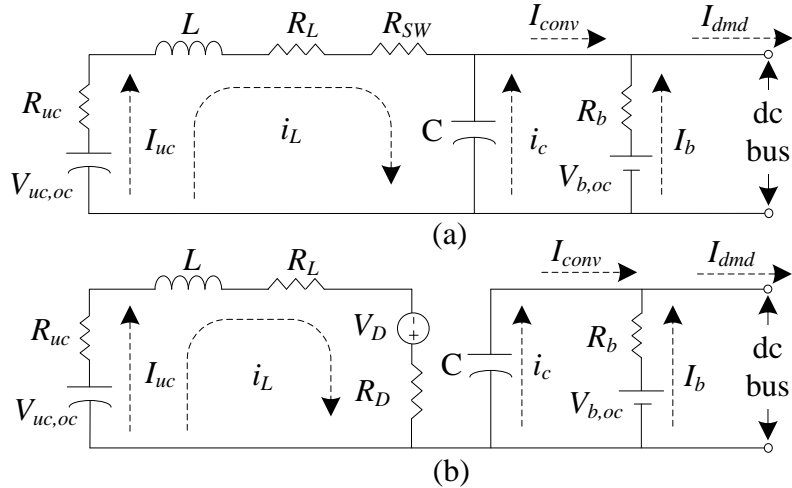


Figure 4.5 Buck Mode. (a) S_1 is on and D_2 is off; (b) S_2 is on and D_2 is on.

When the gate drive signal of S_1 is high, MOSFET S_1 turns on and the diode D_2 is reverse-biased. The circuit then reduces to Fig. 4.5(a). When S_1 turns off, D_2 is forward-biased and the equivalent circuit is shown in Fig. 4.5(b). The differential equation Eq. (4.9) and Eq. (4.10) are derived for these two switching intervals in Fig. 4.5(a) and Fig. 4.5(b) based on steady-state analysis.

$$\begin{bmatrix} \frac{di_L}{dt} \\ \frac{dv_c}{dt} \end{bmatrix} = \begin{bmatrix} -\frac{(R_{uc} + R_L + R_{SW})}{L} & -\frac{1}{L} \\ \frac{1}{C} & -\frac{1}{CR_b} \end{bmatrix} \begin{bmatrix} i_L \\ v_c \end{bmatrix} + \begin{bmatrix} \frac{1}{L} & 0 & 0 \\ 0 & \frac{1}{CR_b} & -\frac{1}{C} \end{bmatrix} \begin{bmatrix} V_{uc,oc} \\ V_{b,oc} \\ I_{dmd} \end{bmatrix} \quad (4.9)$$

$$\begin{bmatrix} \frac{di_L}{dt} \\ \frac{dv_c}{dt} \end{bmatrix} = \begin{bmatrix} -\frac{(R_{uc} + R_L + R_D)}{L} & 0 \\ 0 & -\frac{1}{CR_b} \end{bmatrix} \begin{bmatrix} i_L \\ v_c \end{bmatrix} + \begin{bmatrix} \frac{1}{L} & 0 & 0 \\ 0 & \frac{1}{CR_b} & -\frac{1}{C} \end{bmatrix} \begin{bmatrix} V_{uc,oc} \\ V_{b,oc} \\ I_{dmd} \end{bmatrix} + \begin{bmatrix} \frac{1}{L} V_D \\ 0 \end{bmatrix} \quad (4.10)$$

Based on the steady-state analysis as describe above, the average value of V_c is obtained as,

$$V_c = V_{b,oc} + D_{buck} R_b I_L - R_b I_{dmd} \quad (4.11)$$

The input and output currents relationship is,

$$I_{conv} = D_{buck} I_L \quad (4.12)$$

The duty cycle D_{buck} in the range of (0, 1) is,

$$D_{buck} = \frac{-V_{b,oc} - V_D + I_{dmd}R_b - I_L(R_{sw} - R_D) + \sqrt{\Delta_2}}{2I_L R_b} \quad (4.13)$$

$$\Delta_2 = \left(V_{b,oc} + V_D - I_{dmd}R_b + I_L(R_{sw} - R_D) \right)^2 - 4I_L R_b \left(I_L(R_D + R_L + R_{uc}) - V_{uc,oc} - V_D \right) \quad (4.14)$$

4.1.3 Power Losses in HESS

In this study, the conduction and switching losses of the DC-DC converter are considered for both Boost and Buck modes. The DC-DC converter conduction losses is,

$$P_{dc,loss} = \begin{cases} D_{boost} I_L^2 (R_{SW} + R_L) + (1 - D_{boost}) (I_L^2 (R_D + R_L) + I_L V_D), & I_L > 0 \\ D_{buck} I_L^2 (R_{SW} + R_L) + (1 - D_{buck}) (I_L^2 (R_D + R_L) - I_L V_D), & I_L < 0 \\ 0, & I_L = 0 \end{cases} \quad (4.15)$$

The DC-DC converter switching losses is,

$$P_{sw,loss} = f_s \left(\frac{1}{2} V_c |I_L| (t_r + t_f) + \frac{1}{2} V_c^2 C_{oss} + Q_t V_g + V_c Q_{rr} \right) \quad (4.16)$$

Here, f_s is the switching frequency. t_r and t_f denotes the rise-time and fall-time transitions of MOSFETs during switching periods. C_{oss} is the output capacitance of MOSFET. Q_t is the gate charge due to charging the gate capacitance by gate voltage. Q_{rr} denotes the reverse recovery charge. The part parameters for DC-DC converter are shown in Table 4.2.

Table 4.2 Parameters for DC-DC converter.

Parameter	Symbol	Value	Unit
Inductor winding resistance	R_L	10	[mΩ]
Switch on resistance	R_{sw}	43	[mΩ]
Body diode resistance	R_D	40	[mΩ]
MOSFET rise-time	t_r	13	[ns]
MOSFET fall-time	t_f	12	[ns]
MOSFET output capacitance	C_{oss}	1860	[pF]
Gate charge	Q_t	490	[nC]
Gate voltage	V_g	30	[V]
Reverse recovery charge	Q_{rr}	2	[μC]

Considering both the conduction losses and switching losses, the DC-DC converter efficiency is evaluated for both operation modes as,

$$\eta = \begin{cases} \frac{V_c(1-D_{boost})I_{uc}}{V_c(1-D_{boost})I_{uc} + P_{dc,loss} + P_{sw,loss}}, & I_{uc} > 0 \\ \frac{(V_{uc,oc} - I_{uc}R_{uc})|I_{uc}|}{(V_{uc,oc} - I_{uc}R_{uc})|I_{uc}| + P_{dc,loss} + P_{sw,loss}}, & I_{uc} < 0 \end{cases} \quad (4.17)$$

Using the part parameters for DC-DC converter as given in Table 4.2, the efficiency maps for both Boost mode and Buck mode are demonstrated in Fig. 4.6.

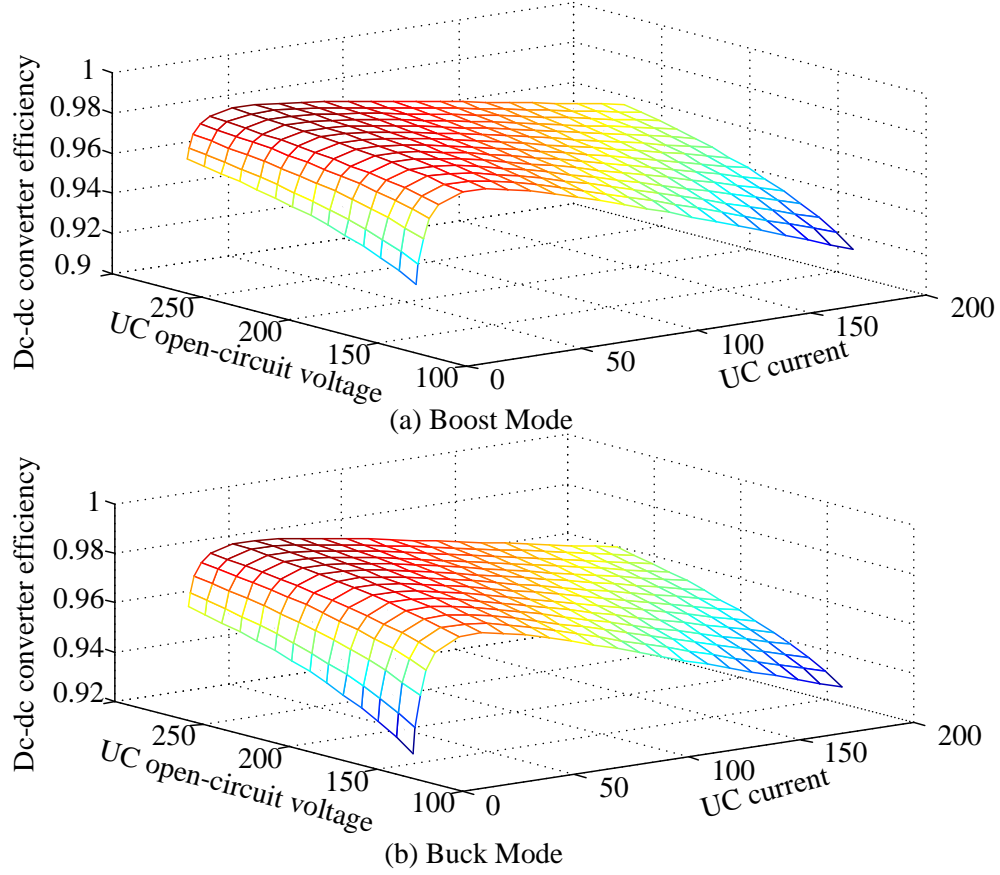


Figure 4.6 (a) The efficiency map of the DC-DC converter in Boost mode; (b) the efficiency map of the DC-DC converter in Buck mode.

In this efficiency map, the UC current value range is from 5A to 200A and the UC open-circuit voltage varies from 135V to 270V. It can be observed that the DC-DC converter has lower efficiency when it operates at light-load condition. The total power losses in HESS is the sum of power losses in the bi-directional DC-DC converter and in the battery/UC as,

$$P_{loss} = P_{dc,loss} + P_{sw,loss} + I_b^2 R_b + I_{uc}^2 R_{uc} \quad (4.18)$$

4.2 HESS Energy Management Problem Formulation

The HESS energy management problem is to effectively split the load demand between battery and UC. The driving schedule $\{v_s(k), k = 1, 2, \dots, N\}$, and the load demand current $\{I_{dmd}(k), k = 1, 2, \dots, N\}$ are known as a priori for offline optimization problem. This optimization problem is a multi-step decision problem: at each time instant, one decides the demand current split for battery and UC for the next time step, to achieve the minimum objective value while satisfying the constraints. To find the optimal control sequence, DP algorithm is applied to solve the problem.

4.2.1 Objective Functions

Two cost functions are considered in the HESS energy management problem as,

$$f_1(k) = P_{loss}(k) / P_{loss,max}, \quad k = 1, 2, \dots, N \quad (4.19)$$

$$f_2(k) = \begin{cases} (I_b(k) - I_b(k-1))^2 / (\Delta I_{b,max})^2, & k = 2, 3, \dots, N \\ (I_b(k))^2 / (\Delta I_{b,max})^2, & k = 1 \end{cases} \quad (4.20)$$

Here, both cost functions are normalized because the scales of these two cost functions are different. The value of $P_{loss,max}$ is set to 2000W and the $\Delta I_{b,max}$ is set to 20A. Minimizing the objective function, f_1 , results in reduced power losses. Minimizing the objective functions f_2 will result in the battery current magnitude/variations reduction, which in turn will prolong the battery lifetime. The optimization problem, as given in Eq. (4.21), is to minimize a weighted sum of these

two functions over the entire drive cycles, while satisfying several constraints for each time step.

$$\sum_{k=1}^N (w_1 f_1(k) + w_2 f_2(k)) \quad (4.21)$$

Here, $w_1, w_2 \geq 0$ are the weight factors of the two cost functions.

4.2.2 Problem Formulation

In this optimization problem, the DC-DC converter output current is chosen as the control variable. The battery current can be obtained based on the load demand current conservation equation as,

$$I_b(k) = I_{dmd}(k) - I_{conv}(k), \quad k = 1, 2, \dots, N \quad (4.22)$$

The UC current, which is equal to I_L , can be derived based on the state space average model of the bi-directional DC-DC converter as,

$$I_{uc}(k) = \begin{cases} I_{conv}(k)/(1-D_{boost}(k)), & I_{conv}(k) > 0 \\ I_{conv}(k)/D_{buck}(k), & I_{conv}(k) < 0 \\ 0, & I_{conv}(k) = 0 \end{cases} \quad k = 1, 2, \dots, N \quad (4.23)$$

The constraints in this problem include the limits on the battery/UC current and voltage operation ranges,

$$I_{b, \min} \leq I_b(k) \leq I_{b, \max}$$

$$I_{uc, \min} \leq I_{uc}(k) \leq I_{uc, \max}$$

$$V_{uc, \min} \leq V_{uc}(k) \leq V_{uc, \max}, \quad k = 1, 2, \dots, N \quad (4.24)$$

where the subscripts of min and max denote the minimum and maximum value of each variable.

Thus, the optimization problem is formulated as,

$$\underset{I_{conv} \in \mathcal{R}^N}{\text{Minimize}} \quad \text{Eq. (4.21)} \quad (4.25)$$

$$s.t. \quad \text{Eq. (4.22) - Eq. (4.24)}$$

4.2.3 Dynamic Programming

In this optimization problem, the control variable I_{conv} is denoted as μ . The objective $f_2(k)$ at time step k involves both $I_b(k)$ and $I_b(k-1)$. While $I_b(k)$ is determined by the control value $\mu(k)$ at time step k ; $I_b(k-1)$ depends on the previous control value. To fit within the standard dynamic programming model, we make $I_b(k-1)$ a state variable $x_1(k)$. In view of Eq. (4.22), we have,

$$x_1(k+1) = I_b(k) = I_{dmd}(k) - \mu(k), \quad k = 1, 2, \dots, N \quad (4.26)$$

which we write more compactly as,

$$x_1(k+1) = g_{1k}(\mu(k)), \quad k = 1, 2, \dots, N \quad (4.27)$$

where the subscript k reflects the dependence on $I_{dmd}(k)$.

Next, to allow for the constraint Eq. (4.24) on the UC voltage, we make the UC state-of-charge SoC_{uc} a second state variable, x_2 . The associated state equation is written as,

$$x_2(k+1) = g_{2k}(x_2(k), \mu(k)), \quad k = 1, 2, \dots, N \quad (4.28)$$

Eq. (4.27) and Eq. (4.28) are grouped into a 2-dimensional state equation.

$$x(k+1) = g(x(k), \mu(k)), \quad k = 1, 2, \dots, N \quad (4.29)$$

where $x(k) = [x_1(k), x_2(k)]$. We re-write the objective function Eq. (4.21) compactly as,

$$J(\mu) = \sum_{k=1}^N J_k(x(k), \mu(k)) \quad (4.30)$$

where μ denotes the N -vector $\mu(k)$, $k=1,2,\dots, N$. The subscript k in J_k reflects dependence of $f_1(k)$ on $I_{dmd}(k)$. The constraints in Eq. (4.24) are generalized on x and μ as,

$$\varphi_k(x(k), \mu(k)) \leq 0, \quad k = 1, 2, \dots, N \quad (4.31)$$

A cost-to-go function, $V_\tau(\zeta)$, is constructed for each time step τ and each state level $\zeta = [\zeta_1, \zeta_2]$. This cost-to-go function keeps track of the minimum objective function value that can be achieved when the initial time is τ and the initial state is ζ . With this cost-to-go function, the optimal control decision at time τ and the state ζ can be found, according to Bellman's principle of optimality,

$$V_\tau(\xi) = \begin{cases} 0, & \tau = N+1 \\ \min_{u \in U_{\tau\xi}} \{J_\tau(\xi, u) + V_{\tau+1}(g_\tau(\xi, u))\}, & \tau = 1, 2, \dots, N \end{cases} \quad (4.32)$$

This cost-to-go function is recursively evaluated using backwards induction from $\tau = N$ to $\tau = 1$ and for all the states $x \in \mathcal{R}^2$. The optimal decision at time τ with state ξ is obtained as,

$$\mu_\tau(\xi) = \arg \min_{u \in U_{\tau\xi}} \{J_\tau(\xi, u) + V_{\tau+1}(g_\tau(\xi, u))\} \quad (4.33)$$

where $U_{\tau\xi}$, the set of admissible controls at time τ and state ξ , is given by,

$$U_{\tau\xi} = \{u : \varphi_\tau(\xi, u) \leq 0\} \quad (4.34)$$

4.2.4 DP Implementations and Optimization Results

To implement DP, we first discretize the state variable of $x_1(k)$. The feasible area of the battery current is set by the bounds of $I_{b,max}$ and $I_{b,min}$. This area is mapped onto a fixed grid with grid size of ΔI_b , such that $q+1$ discrete state levels are considered,

$$\Delta I_b = \frac{I_{b,max} - I_{b,min}}{q} \quad (4.35)$$

Similarly, the state variable of $x_2(k)$ is discretized. A feasible area of SoC_{uc} is set by the bounds of $SoC_{uc,max}$ and $SoC_{uc,min}$. This area is mapped onto a fixed grid with grid size of ΔSoC_{uc} , such that exactly $m+1$ state levels are considered,

$$\Delta SoC_{uc} = \frac{SoC_{uc,max} - SoC_{uc,min}}{m} \quad (4.36)$$

Problem in Eq. (4.33) is then solved as follows.

First, at each step τ , $V_\tau(\zeta)$ is computed for state ζ in the finite set $\mathcal{E} = \{[\zeta_1, \zeta_2]$: $\zeta_1 \in \{ \zeta_1^1, \dots, \zeta_1^{q+1} \}$, $\zeta_2 \in \{ \zeta_2^1, \dots, \zeta_2^{m+1} \} \}$. Second, for each state $\zeta \in \mathcal{E}$, the minimization with respect to μ is performed over the finite set $\tilde{U} = \{ \mu^1, \dots, \mu^{q+1} \}$ by evaluating the right-hand side of Eq. (4.33) at each grid point. Third, in effecting this minimization, $g(\zeta, \mu)$ is replaced by its nearest point (coordinate-wise) in \mathcal{E} .

As a result, this computation generates a table containing, the optimal control $\mu_\tau(\zeta)$ for each time step $\tau=1,2,\dots, N$, and each state $\zeta \in \mathcal{E}$. In the simulation, this table is invoked to give the optimal control decision at each current state with the state value rounded to its nearest point in \mathcal{E} .

The flowchart of the DP algorithm is shown in Fig. 4.7.

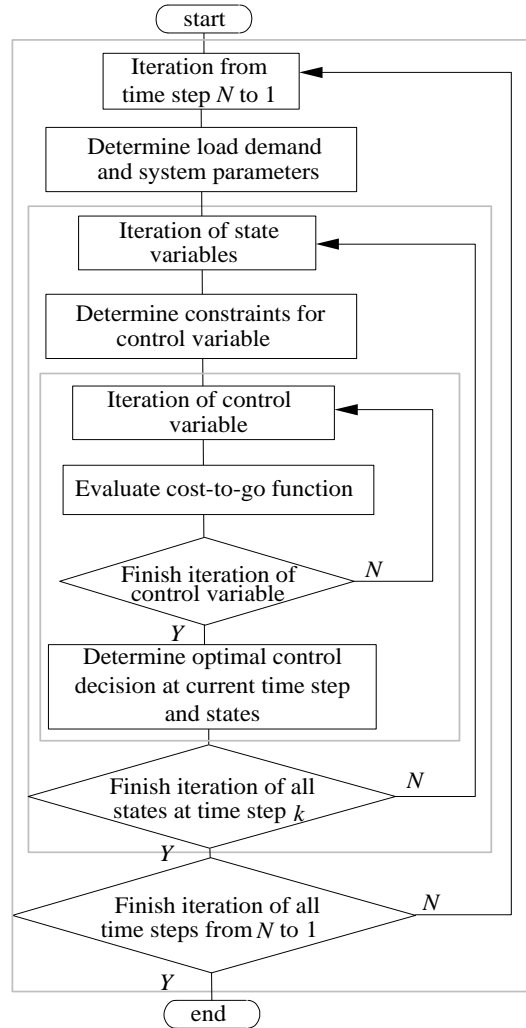


Figure 4.7 The flowchart of DP implementation.

As shown in Fig. 4.7, there are three iteration loops in this DP algorithm. The algorithm starts backwards iteration from time $k=N$ to $k=1$. At each time step, the cost-to-go function is updated based on the control variable iteration results at each state by minimizing the objective function value. After the state iterations, DP generates a look-up table of the optimal decision variable at each state at each time step.

With an initial state, the optimal decision at this state can be determined and performed according to the generated look-up table. Based on the state transition process, the next state and the corresponding optimal decision at the next time step are found. With the optimal decision performed at each time step, the optimal decision sequence is determined.

4.2.5 Numerical Results

The DP algorithm is applied to the Urban Dynamometer Driving Schedule (UDDS) with the weight factors set as $w_1 = w_2 = 0.5$ to give the equal importance for the two objective functions. With the standard drive cycle data, the load demand is obtained based on the EV model parameters. In this work, the total mass of the EV model is 1600kg. The frontal area of the EV is 2.25m^2 , the aerodynamic drag coefficient is 0.3 and the wheel radius is 0.3m. The DC bus voltage is 360V. With these EV model parameters, the load demand for the HESS is derived [5].

The feasible area of the UC voltage is set by the bounds of $V_{uc,max} = 270$ and $V_{uc,min} = 135$. The limits on the battery/UC current are set as $I_{b,max} = 360\text{A}$, $I_{b,min} = -90\text{A}$ and $I_{uc,max} = 120\text{A}$, $I_{uc,min} = -120\text{A}$, according to the battery/UC characteristics. In this work, the number of discrete state levels are set with $q = 225$ and $m = 200$ for the consideration of quantization errors and the computation complexity. Therefore, the state grid size of ΔI_b is 2A and the ΔSoC_{uc} is 0.25%.

Fig. 4.8 shows the optimization results, including the load current, the battery/UC current and the DC-DC converter output current. The DC-DC converter efficiency is evaluated according to Eq. (4.17).

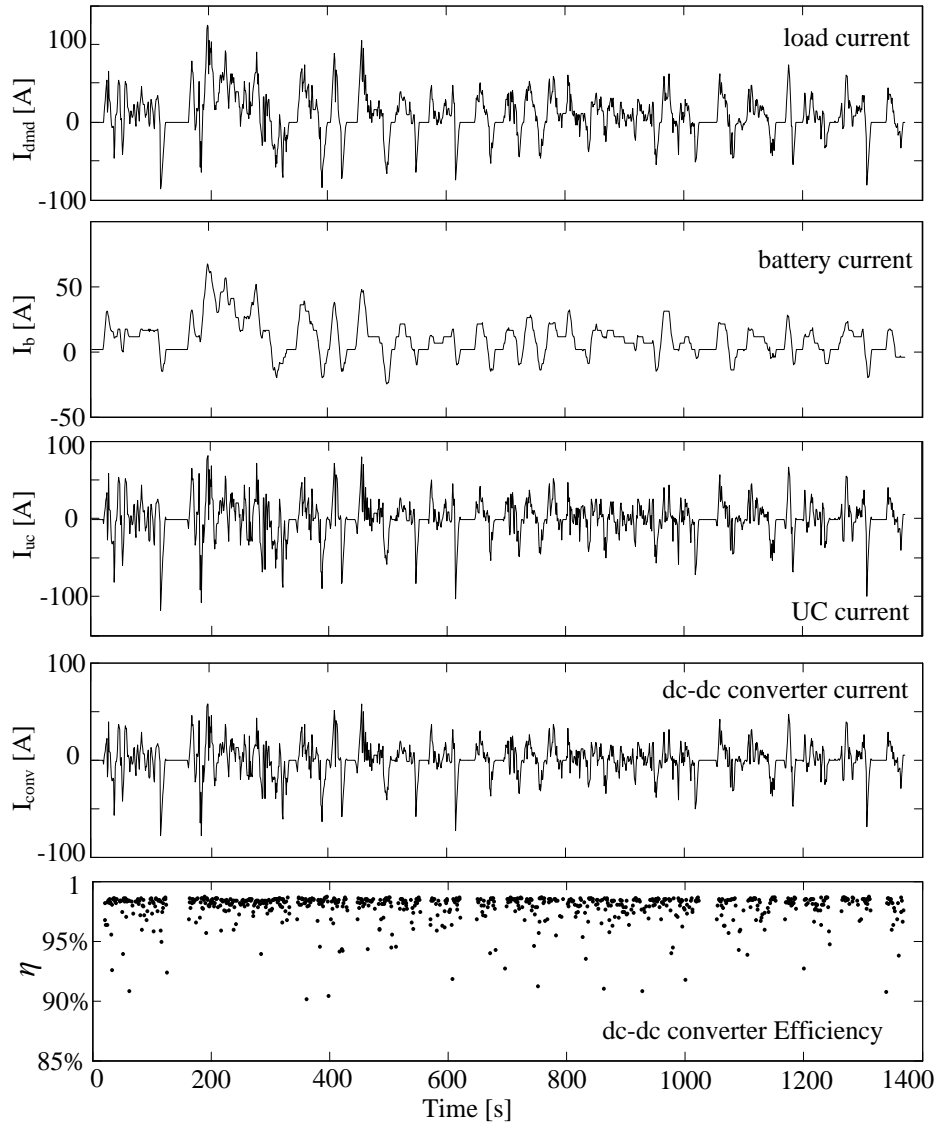


Figure 4.8 Optimization results of DP algorithm under UDDS cycle.

The optimization result shows that UC effectively reduces the battery current peak. In this optimized HESS, the peak battery discharging and charging currents have been reduced by 46% and 82% in comparison to the battery-only ESS. In addition, the DC-DC converter works with high efficiency during the entire drive cycle, which minimizes the HESS power losses. This offline optimization framework

using DP algorithm has been applied to various drive cycles, obtaining the training data to construct the NN.

4.3 Real-Time HESS Energy Management

The goal is to construct an effective online implementation of the control strategy described in offline optimization. As mentioned in Section 4.2, DP algorithm explicitly depends on the future load demand or the future vehicle trip information, thus it is infeasible for real-time implementations. It is also difficult to derive a deterministic equation of the optimal energy management control strategy due to the system complexity. NN, with the capacity to represent or emulate human knowledge, can be effectively used for system approximation of complex systems. In this way, NN is applied to learn the optimal results by DP.

4.3.1 NN Training Data

As a first step in constructing the NN, the offline optimization program is solved for different representative drive cycle datasets, obtaining the required input and target data to train the NN.

In this work, the standard drive cycle datasets are used, obtained from Autonomie software by Argonne National Laboratory, including UDDS, NEDC, Extra-Urban Driving Cycle (EUDC), CUDEC, Japan 10 Mode, Japanese 10-15 Mode, Japanese JC08, SC03, Unified LA92 and FTP75 drive cycles [109].

For each drive cycle, the DP optimization described in Section 4.2 is solved to obtain the optimal decision sequences of the battery/UC current. With the optimal data vectors/sequences of the battery current (I_b), UC current (I_{uc}) determined, the UC

SoC (SoC_{uc}) sequence is also obtained. These obtained data vectors are used as the net input including the load current (I_{dmd}), the UC SoC and the battery current at the previous time step (I_{b_prev}). These inputs are used because the energy management control strategy is influenced by these factors according to the DP algorithm. In addition, the vehicle speed (v_s), and the vehicle acceleration (a) are used as the net inputs. Note that unlike the DP algorithm, the NN does not depend on future load demand or future drive cycle information. However, it does not preclude the opportunity to use the current or the past drive cycle information to improve the energy management performances. The vehicle speed and the acceleration data provide knowledge about the driving trend, which also influence the energy management control strategy. Given these net input data, the optimal decision of I_{uc} is used as the target data. With these training data, the NN is trained with the net architecture shown in Fig. 4.9.

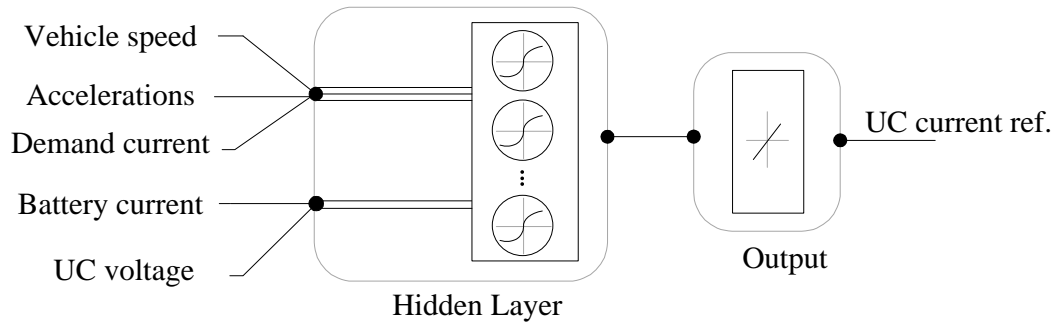


Figure 4.9 The NN architecture for online energy management controller.

4.3.2 NN Training

This NN is designed and trained using the Neural Network Toolbox software in MATLAB [112]. This feed-forward NN is designed with five input nodes for the five

different inputs, with one hidden layer and one output node. There are 20 neurons in the hidden layer. This hidden layer of 20 neurons with nonlinear transfer functions allow the network to learn nonlinear relationships between the input vectors and the output vector. To train the NN, Levenberg-Marquardt algorithm is used as it is characterized by its fast convergence and robustness. The NN training performance is measured by the mean quadratic errors (MSEs) [112].

To create and configure this two layer NN, the *feedforwardnet* command in Matlab have been used with the following command lines.

```
hiddenLayerSize = 20;  
net = feedforwardnet(hiddenLayerSize);
```

To configure the NN training algorithm, the training algorithm '*net.trainFcn*' is set to '*trainlm*' as the Levenberg-Marquardt algorithm is selected. The performance function '*net.performFcn*' is set to '*mse*'. The following command lines are implemented in Matlab to configure the NN for the selected training algorithm and performance function.

```
net.trainFcn = 'trainlm';  
net.performFcn = 'mse';
```

To validate the NN, the relationship between the outputs of the NN and the actual target value is plotted as shown in Fig. 4.10.

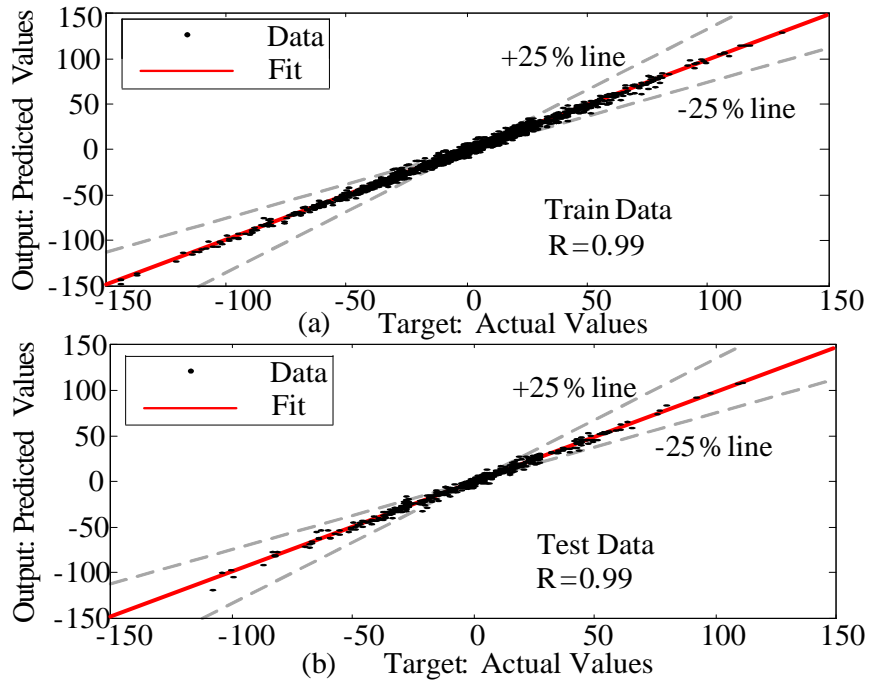


Figure 4.10 Performances of NN in output prediction. (a) Train data; (b) Test data.

Fig. 4.10(a) illustrates the results in the training phase while Fig. 4.10(b) shows the results in the test phase, respectively. Two $\pm 25\%$ error lines are added for comparisons. As shown in Fig. 4.10, the NN model performs well in terms of prediction accuracy.

4.3.3 Intelligent Online Energy Management Controller

The trained and validated NN is implemented as an intelligent online energy management controller. By taking the real-time data for the NN inputs, the NN outputs the command value of the DC-DC converter current.

4.3.4 Test Results

The proposed online energy management controller is applied to test drive cycles.

The online power split results are illustrated in Fig. 4.11 over a test drive cycle.

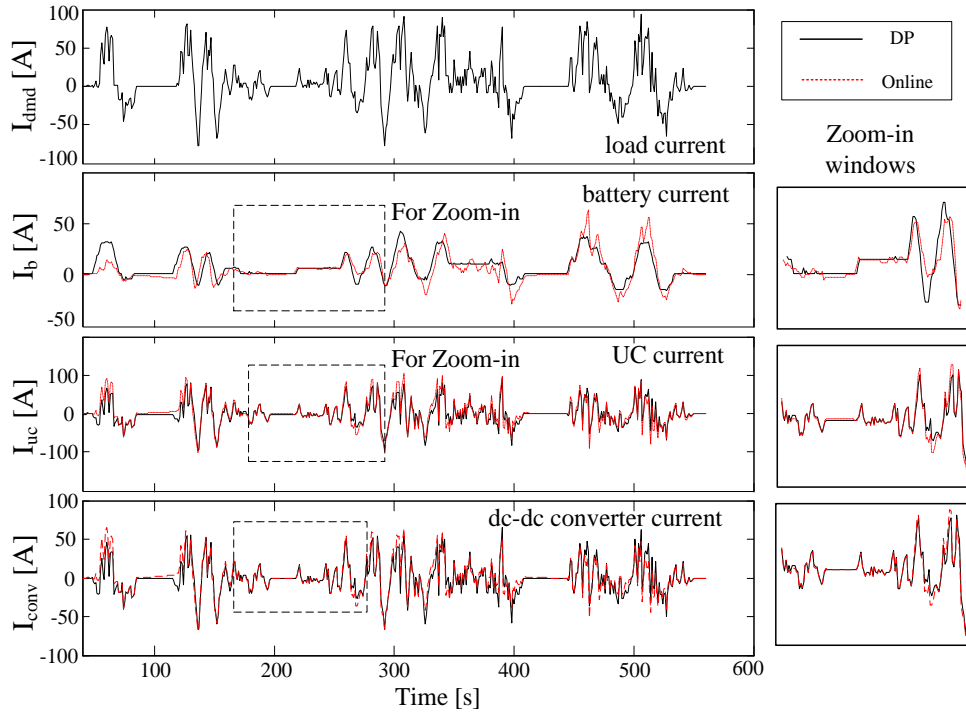


Figure 4.11 Online energy management results vs. offline DP optimization results.

The power split performance generated by NN is analyzed and compared with those generated by DP in offline, which is used as the benchmark of the optimal performances. The online results are shown in dotted lines and the offline results are presented in solid lines. It can be observed that the power split performance generated by the NN closely follows the offline optimization results. The study also involves the analysis of the battery peak shaving effect by UC and the battery lifetime as described in the following section.

4.4 Battery State-of-Health Evaluation

While the system efficiency and fuel economy have been extensively used for evaluation of energy management in HEV applications, there is no standardized performance measure to evaluate the effectiveness of control strategies for EV applications. The battery life, as one critical performance metric, is not often considered/evaluated for EV applications due to the battery life modeling difficulty, especially under realistic driving conditions [113] [114] [115].

4.4.1 Battery State-of-Health Estimation Model

For different real-time energy management methodologies, problem formulations and implementation processes are different. To perform a comparative analysis for different control strategies, a standard performance measure for various energy management methodologies is crucial.

A typical battery EOL refers to 20% degradation in the battery nominal energy capacity. In this case, the estimation of the battery SoH is determined by the estimation of the battery capacity degradation. The battery capacity degradation can be estimated by measuring the battery SoC-OCV (open circuit voltage) relationship [116] [117]. Various methods of battery capacity estimation are summarized in [116]. These methods require extensive laboratory investigations and large experimental data sets. These large test data of the battery characteristics and conditions are used to develop battery capacity fade model. The battery capacity fade models have been primarily categorized as physics-based model [118] [119] and empirical model [117] [120]. The physics-based models are derived based on complex battery

electrochemical models, which require the investigation and measurements of the battery material properties, internal structures and parameters. This information, in general, is not easily available. Different models have been developed to account for various incidents responsible for capacity loss such as the parasitic side reactions [121], SEI (solid electrolyte interface) formation [122], and impedance increase [123]. The computation burden of these physics-based models makes them impractical for EV battery real-time SoH estimation [124] [125]. Therefore, an empirical model is more suitable for battery SoH estimation for EV application. For empirical model development, experimental data are essential for statistical evaluation and validation. Bloom *et al.* presents the testing results and develops a battery capacity fade prediction model using large experimental data set [120]. This model is later adopted as a starting point by Wang *et al.* [117] to develop a physically justified empirical model as shown in Eq. (4.37),

$$\Delta Q_{loss} = B e^{\frac{-E_a}{RT}} Q_{tp}^z \quad (4.37)$$

Here, ΔQ_{loss} is the battery capacity degradation percentage number. T is the absolute temperature and R is the gas constant of $8.314 \text{ Jmol}^{-1}\text{K}^{-1}$. Q_{tp} is the charge throughput (in [Ah]) that leads to the capacity degradation. z is the power law factor with the value of 0.55. B and E_a are the fitting parameter and the activation energy from Arrhenius law [117], respectively. The activation energy E_a is a function of the current rate as shown in Eq. (4.38).

$$E_a = 31700 - 370.3I_{br} \quad (4.38)$$

where, the battery current rate I_{br} is defined as the ratio between battery current and its nominal capacity (in [Ah]) in Eq. (4.39).

$$I_{br} = \frac{|I_b|}{Q_b} \quad (4.39)$$

The pre-exponential parameter B under different current rates is obtained based on the empirical fitting as shown in Table 4.3.

Table 4. 3 Parameter B with respect to current rates [117].

Current rate I_{br}	0.5	2	6	10
B	31630	21681	12934	15512

In order to account for the effect of realistic drive cycle on EV battery life, a throughput-based battery capacity fade model is adopted [124] [126]. This throughput-based model assumes that a battery can deliver or take a certain amount of charge throughput under constant operation condition before it reaches EOL. Based on this throughput-based battery capacity fade model [124], the battery SoH is given as a function of battery current, shown in Eq. (4.40).

$$SoH(t) = SoH(0) - \frac{\int_0^t |I_b(\tau)| d\tau}{3600Q_{p,\max}} \quad (4.40)$$

Therefore, the battery SoH variation from the initial time to time t is defined in Eq. (4.41),

$$\Delta SoH(t) = \frac{\int_0^t |I_b(\tau)| d\tau}{3600Q_{p,\max}} \quad (4.41)$$

In this model, both charging and discharging currents are assumed to have the same impact, in contributing to the battery aging. Thus, the absolute value of battery current is integrated. The $SoH(0)$ represents the initial battery SoH and $Q_{tp,max}$ (in [Ah]) is the maximum amount of charge throughput that a battery can have before it reaches its EOL. As dt is considered in the unit of second, the number 3600 in the denominator is used for unit conversion from second to hour.

The derivative of each side of Eq. (4.41) is derived to evaluate the effect of battery current rate on the battery SoH variation rate.

$$\Delta SoH_{rate} = \frac{I_{br} Q_b}{3600 Q_{tp,max} (I_{br})} \quad (4.42)$$

Under different battery current rates, the maximum charge throughput, $Q_{tp,max}$, is different. It is assumed that under a certain current rate, a battery can deliver a certain amount of charge throughput [124]. To evaluate the maximum amount of charge throughput, $Q_{tp,max}$, under different current rates, the capacity degradation percentage number ΔQ_{loss} is set to 20. Using Eq. (4.39), $Q_{tp,max}$ can be expressed by Eq. (4.43).

$$Q_{tp,max} (I_{br}) = \left(\frac{20}{B(I_{br}) e^{\frac{-(E_a(I_{br}))}{RT}}} \right)^{1/z} \quad (4.43)$$

Substituting Eq. (4.43) into Eq. (4.42) gives,

$$\Delta SoH_{rate} = \frac{I_{br} Q_b \cdot \left(B(I_{br}) e^{\frac{-(E_a(I_{br}))}{RT}} \right)^{1/z}}{3600 \cdot 20^{1/z}} \quad (4.44)$$

Though various factors may impact the battery SoH, the proposed battery SoH estimation model emphasizes the relative impact of the battery current rate, which can provide a performance measure for real-time EV energy management strategies. This simplified control-oriented battery SoH estimation model permits its application in real-time realistic drive cycles. To evaluate the battery SoH variation during one drive cycle, the Eq. (4.44) is integrated obtain ΔSoH as defined in Eq. (4.41). This battery ΔSoH estimation is used as one performance measure for different real-time energy management strategies under realistic drive cycles.

In order to extend this battery SoH estimation model to different scenarios with current rates below 10C, a piecewise-defined function is used to fit and derive the relationship between the value of ΔSoH_{rate} and the intermediate current rates. The value of ΔSoH_{rate} under different battery current rates is evaluated and plotted in Fig. 4.12.

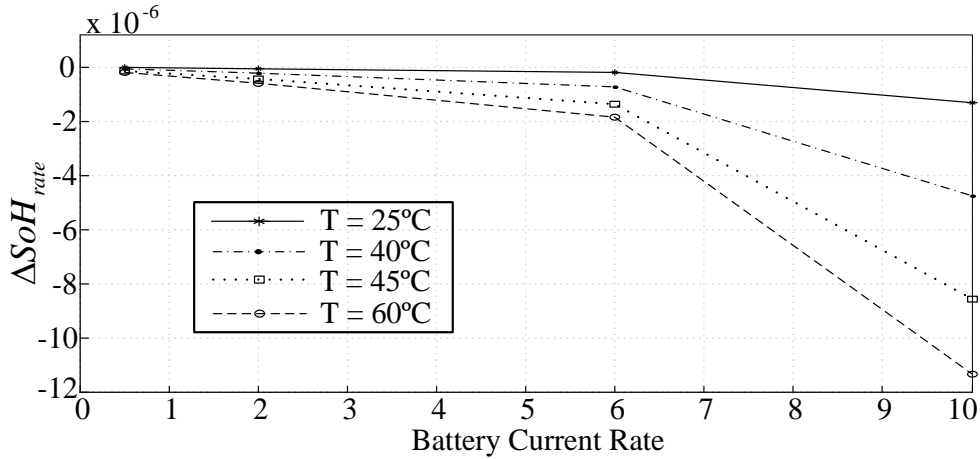


Figure 4.12 ΔSoH_{rate} as a function of battery current rate.

With higher battery current rate, the effect on SoH is greater. At room temperature of $T = 25^\circ\text{C}$, the relationship between ΔSoH_{rate} and the battery current rate is fitted using a piecewise-defined function for current rates in $[0,6]$ and $(6,10]$ with $k_1 = -3.1327 \cdot 10^{-8}$ and $k_2 = -2.7977 \cdot 10^{-7}$.

$$\Delta\text{SoH}_{rate}(I_{br}) = \begin{cases} k_1 I_{br} & I_{br} \in [0,6] \\ k_2 (I_{br} - 6) + 6k_1 & I_{br} \in (6,10] \end{cases} \quad (4.45)$$

In this way, the battery SoH derivative is expressed as a function of battery current. This model can be adopted to evaluate the battery SoH under various current rates for EV application.

4.4.2 Results and Analysis

The battery peak shaving and its SoH are evaluated. These results of the proposed online intelligent energy management controller are analyzed through comparison with the offline optimization results and the results obtained by a rule-based control strategy as described below.

This rule-based energy management control strategies set UC voltage references based on heuristics [60]. Typically, when the vehicle starts, it requires a large amount of power. Thus, the UC voltage references are set to high levels when the vehicle is stopped or at very low speed in order to prepare sufficient power to the motor whenever needed for accelerations. In urban driving situation, UC captures regenerative braking energy when the vehicle speed decreases from high speed.

Therefore, the control strategy sets UC voltage references to allow room for receiving the regenerative braking energy. The UC voltage reference profile is given as [60],

$$V_{uc,ref}(k) = V_{uc,max} \sqrt{1 - \frac{3v_s(k)}{160}} \quad (4.46)$$

Here, the unit of $v_s(k)$ is mi/h. According to this defined UC voltage reference, the UC discharge and charge current is controlled based on rules explained in details in [60]. In this rule-based algorithm, UC is used to receive the regenerative braking current as much as possible while battery receives the rest within the battery charging current limit. In discharging mode, a battery discharging current limit is set. When there is a large demand current, the battery delivers the maximum discharging current while UC supplies any remaining current if UC voltage is above the reference voltage. In this way, this rule-based algorithm aims at reducing the battery peak current through peak shaving by UC. In this work, we implemented this rule-based control strategy for result comparisons.

Fig. 4.13 presents the objective function evaluation for different drive cycles. The objective function values are also normalized by the drive cycle length. Four test drive cycles are used for results evaluation including the New York city drive cycle, the Artemis drive cycle, the West Virginia city drive cycle and the Manhattan drive cycle.

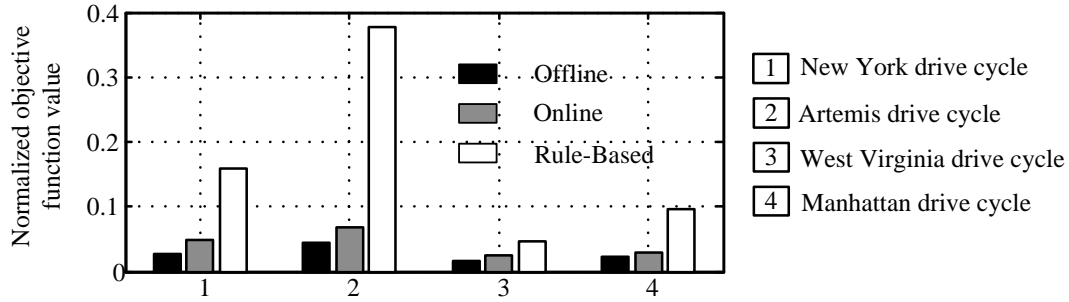


Figure 4.13 Normalized objective function value evaluated under different methodologies for four different drive cycles.

Tables 4.4 - Table 4.6 summarize the results obtained by DP, the proposed online controller and the rule-based control strategy, under different drive cycles. Table 4.4 presents DC-DC converter operation efficiency in both propulsion and regeneration modes.

Table 4.4 Bi-directional DC-DC converter operation efficiency in both propulsion mode and regenerative braking mode [%].

Cycle Name	DP		Online		Rule-Based	
	Propulsion	Regen.	Propulsion	Regen.	Propulsion	Regen.
NY_City	98.1	98.6	98	98.2	94.6	94.5
Artemis	98.1	97.7	97.9	98	94.9	95.3
WVU	97.7	97.6	97.6	97.1	92.7	94.8
Manhattan	98	97.2	97.8	97.2	94.9	94.5

As shown in Table 4.4, the proposed supervisory energy management controller has improved the bi-directional DC-DC converter operation efficiency by about 4% in comparison to the rule-based control strategy.

Fig. 4.14 presents the simulation results of the battery peak current under different drive cycles.

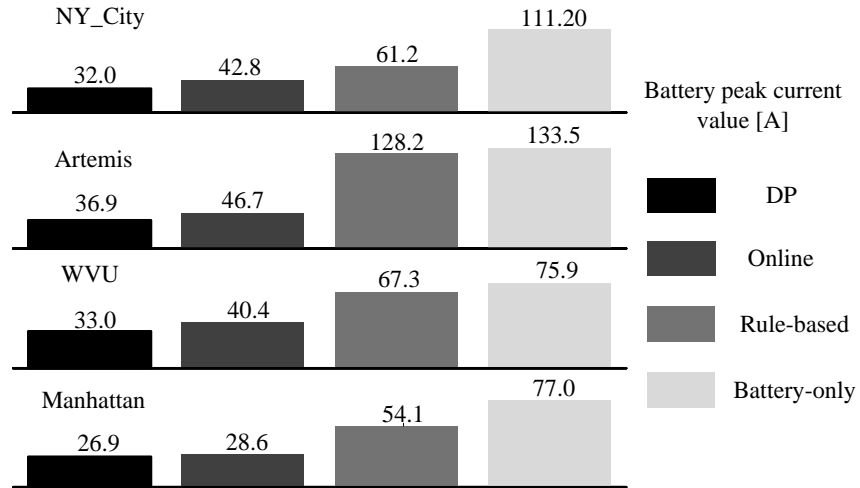


Figure 4.14 Battery peak current value $|I_b|$ under different drive cycles [A].

The proposed energy management controller effectively reduces the battery peak current by 60% in comparison to the battery-only ESS, while the rule-based strategy can only reduce 20% of the battery peak current, in average. The proposed energy management controller can achieve good battery peak current shaving results for all the test drive cycles; while the rule-based controller cannot guarantee effective performance under different driving situations.

In addition, the battery remaining SOH after 10 years are estimated based on the battery SoH estimation model. Here, a daily commute cycle is constructed as a repeated sequence of the corresponding drive cycles to cover 40 miles. The battery remaining SoH after 10 years is estimated based on the assumption that the EV repeats the same daily commute every day. In Table 4.5 -Table 4.6, the results in a

battery-only ESS are also evaluated for comparison. The improvement achieved by the proposed online controller over the battery-only ESS is shown in the last column.

Table 4.5 Battery SoH Estimation After Different Drive Cycles.

Cycle Name	DP	Online	Rule-base	Bat-only	improvement
NY_City	0.88	0.83	0.73	0.72	14.9%
Artemis	0.89	0.88	0.77	0.72	21.6%
WVU	0.91	0.87	0.84	0.84	3.3%
Manhattan	0.89	0.89	0.76	0.75	18.4%

The proposed online intelligent energy management controller obtains effective results in comparison to the benchmark results obtained by DP algorithm. In addition, this proposed online controller improves the battery SoH by 15% in average, in comparison to the battery-only ESS, while the rule-based strategy achieves very small improvement of the battery SoH. Based on the battery SoH estimation, the battery cycle life (in number of daily commute cycles) before the battery reaches a 20% SoH reduction is also evaluated based on the daily commute cycle assumptions.

Table 4.6 Battery Cycle Life Estimation Result.

Cycle Name	DP	Online	Rule-base	Bat-only	Improvement
NY_City	6080	4290	2700	2600	64%
Artemis	6640	6080	3170	2600	134%

WVU	8110	5620	4560	4560	23%
Manhattan	6640	6640	3040	2920	127%

The proposed online energy management controller shows the potential to extend the battery cycle life by 64 % in comparison to the battery-only ESS, while the rule-based control strategy only improves the battery cycle life by less than 5%, using the New York city drive cycles as daily commute. This shows that the proposed real-time energy management controller can greatly outperform the simple rule-based energy management control.

4.5 Summary

In this work, a supervisory energy management strategy for a battery-UC HESS is presented. In the battery-UC HESS modeling stage, a detailed DC-DC converter model is considered in order to include both the conduction losses and the switching losses in the energy management problem. This accurate model gives more insight on how to control the DC-DC converter to avoid light-load operation with low efficiency. In the supervisory energy management controller design state, a multi-objective optimization problem is formulated to prolong the battery lifetime while maintains high efficiency operation of the HESS. The problem is solved by DP and the results are used to develop the neural network for online implementation. As a result, an intelligent real-time energy management controller is implemented. The proposed online energy management controller effectively splits the load demand and achieves excellent result of the battery current peak shaving. It is concluded that the

proposed online energy management controller can effectively reduce the battery peak current by 60% in comparison to the battery-only ESS while the HESS system is operated under high average power efficiency over 95%. Based on the proposed battery SoH estimation model, it is estimated that the battery cycle life can be extended by over 60%, which greatly outperforms the rule-based control strategy.

Chapter 5: Experiment Design and Real-Time Controller Implementation for a Battery-Ultracapacitor Hybrid Energy Storage System

In this work, the proposed real-time energy management strategy has been investigated for the optimal current split between batteries and UCs in EV applications. The proposed NN based strategy is implemented as an intelligent controller for the battery-UC HESS. A 38V-385Wh battery and a 16V-2.06Wh UC HESS hardware prototype has been developed and a proposed real-time experiment platform has been built for energy management controller validation, using xPC Target and National Instrument data acquisition system (DAQ). Both the simulation and real-time experiment results have successfully validated the real-time implementation feasibility and the effectiveness of the real-time controller design.

In this chapter, the system modeling and integration is introduced in Section 5.1, followed by real-time simulation platform introduction and the construction details in Section 5.2. As an extension to the real-time simulation platform, a DAQ system is configured to provide access to the hardware features prior to the final hardware system construction as described in Section 5.3. The hardware prototype of the battery-UC HESS is described in Section 5.4. The experiment results using the proposed real-time controller and the built battery-UC hardware prototype is presented in Section 5.5 followed by the chapter conclusions in Section 5.6.

5.1 Modeling and System Integration

In the designed EV powertrain, a 34kWh battery pack and a 203Wh UC pack are integrated as the HESS for a mid-sized EV. In this work, a scaled-down hardware prototype will be designed with a 385Wh battery pack and a 2.06Wh UC pack. The battery/UC models and their specifications are described in this Section 5.1.

A semi-active HESS topology, shown in Fig. 5.1, is considered. With this topology, the UC current I_{uc} can be controlled through the control of the DC-DC converter. In addition, as the UC pack is decoupled from the DC bus, its voltage can be lower than the DC bus voltage, and consequently the size and cost of UC can be reduced.

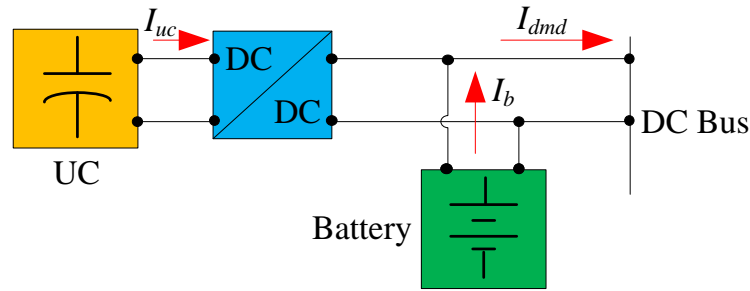


Figure 5.1 The semi-active topology of the battery-UC HESS.

5.1.1 Battery/UC Characteristics

The scaled-down HESS prototype is constructed using a 38V battery pack and a 16V UC pack. The battery pack consists of 40 battery cells with 4 parallel branches including 10 cells in serial connection in each branch. The 16V UC module consists of 6 small UC cells in serial connection. The UC pack is connected to the input of the

DC-DC converter. The battery/UC pack specifications and operation ranges are given in Table 5.1.

Table 5.1 The battery/UC specifications.

Parameter	Value	Unit
Battery Voltage Operation Range	36 ~ 40	[V]
Battery Capacity	10.4	[Ah]
Battery Energy Storage	385	[Wh]
Maximum Battery Current	20	[A]
UC Voltage Operation Range	8~16	[V]
UC Capacitance	58	[F]
UC Energy Storage	2.06	[Wh]
Maximum UC Current	12 ~ 19	[A]

5.1.2 Battery/UC Models

For the real-time simulation, the battery-UC HESS is modelled using high fidelity models from Autonomie software developed by Argonne National Laboratory [127]. The battery cell equivalent circuit model is shown in Fig. 5.2(a). Based on this equivalent circuit model, the relationship between battery voltage V_b and the current I_b is derived as Eq. (5.1),

$$V_b = V_{oc} - I_b \left(R_0 + R_{p1} \frac{I_{p1}}{I_b} + R_{p2} \frac{I_{p2}}{I_b} \right) \quad (5.1)$$

V_{oc} is the battery open-circuit voltage, R_0 is the ohmic resistance, R_{p1} and R_{p2} are the polarization impedances. The parameters are obtained through curve fitting of the battery test data. The two RC networks have time constants $\tau_1 = R_{p1}C_{p1}$ and $\tau_2 = R_{p2}C_{p2}$ with $\tau_1 = 22.8$ second and $\tau_2 = 270$ second, respectively [128]. The battery parameters are implemented as a look-up table using battery SoC as input. Based on the battery equivalent circuit model, the battery discharge curve under 0.5C current rate is shown in Fig. 5.2(b).

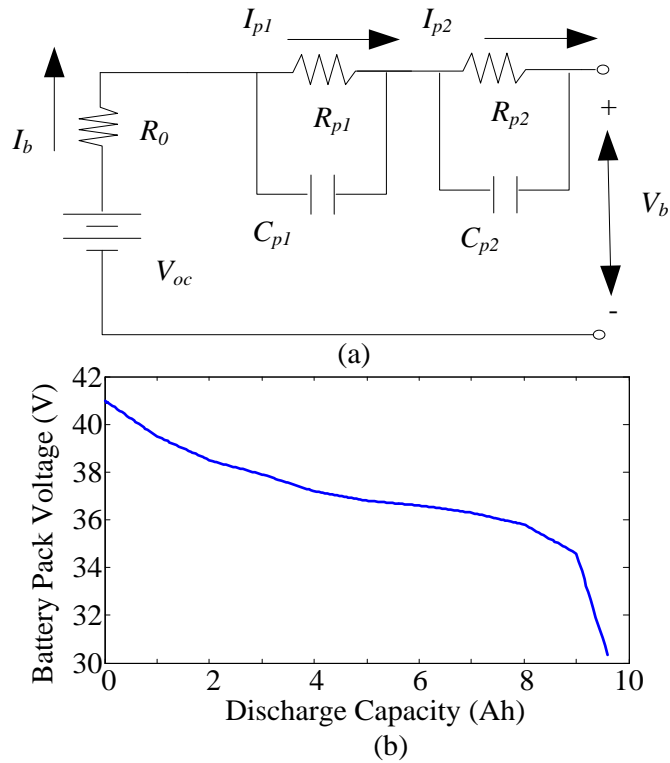


Figure 5.2 (a) Battery equivalent circuit model; (b) Battery discharge curve under 0.5C current rate.

The UC pack is modelled with its capacitance C and an internal resistance R_{uc} as shown in Fig. 5.3.

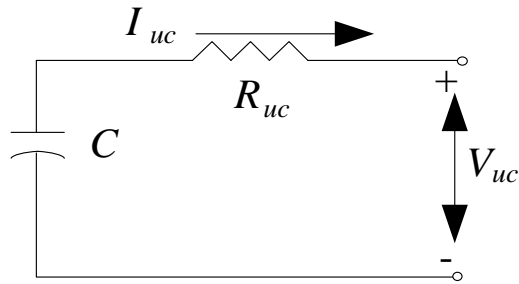


Figure 5.3 UC equivalent circuit model.

The two parameters of C and R_{uc} are implemented as look-up tables with input of the UC current based on UC cells test data [127].

5.1.3 DC-DC Converter Model

The DC-DC converter controls the current flow of the UC pack. Therefore, it is important to model the DC-DC converter efficiency-map under different operation and load conditions. In this work, both the conduction losses and switching losses are included in the DC-DC converter efficiency analyses as the DC-DC converter operates at 120kHz. The efficiency of the DC-DC converter at given input voltage values presented in Fig. 5.4.

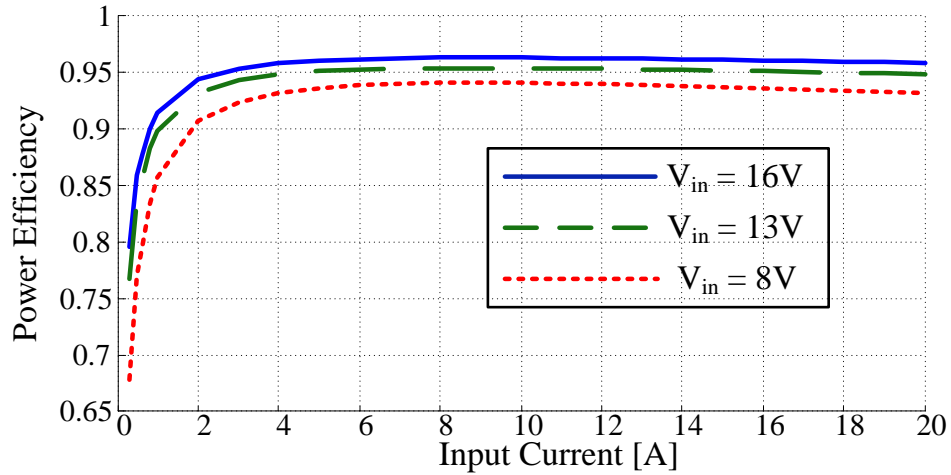


Figure 5.4 DC-DC converter efficiency-map.

5.2 Real-Time Simulation Setup

The entire experiment setup consists of three main subsystems: the real-time controller implemented in the target computer, the hardware plant system and the DC electronic load. Each subsystem setup will be introduced in details.

A block diagram of this experiment platform is shown in Fig. 5.5.

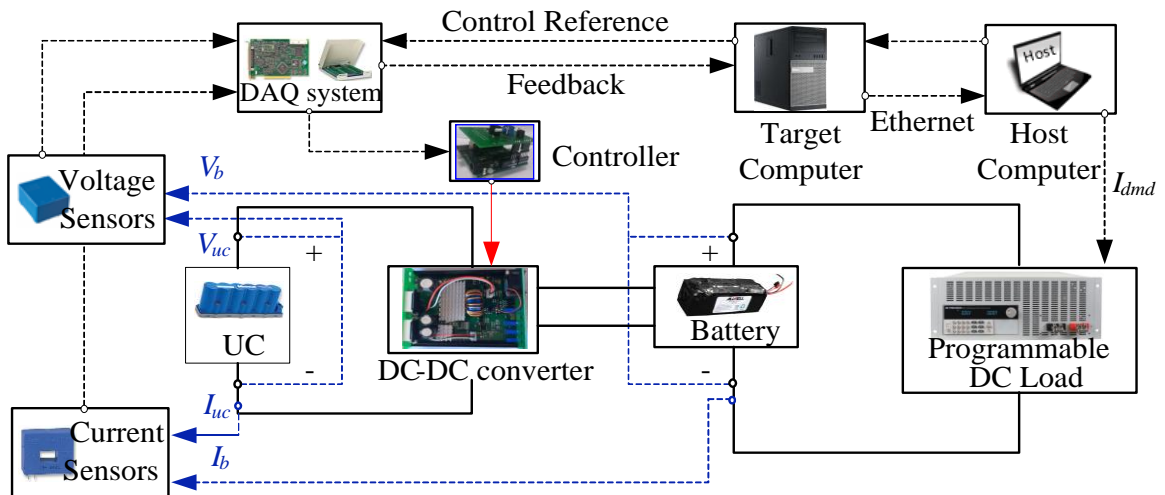


Figure 5.5 The Experiment Setup Diagram.

Based on the battery/UC and DC-DC converter system modeling and the controller system integration, a closed-loop system is configured with the controller and plant interfaced with each other as shown in Fig. 5.6.

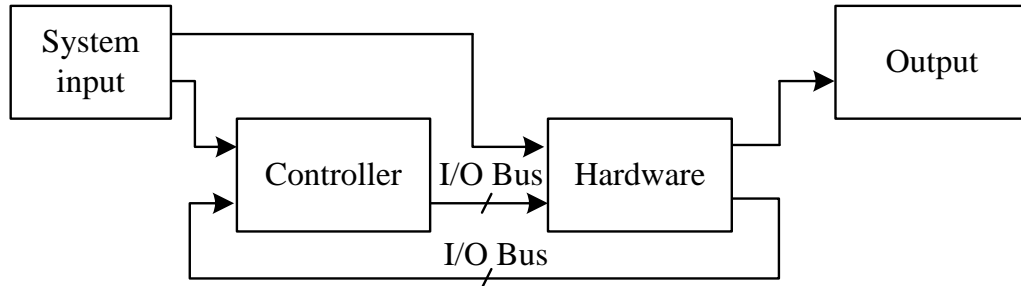


Figure 5.6 The closed-loop system model for testing.

In this closed-loop system model, the system input provides the drive cycle information, i.e., the vehicle speed, the vehicle acceleration and the load demand current, to both the controller and the plant. The plant system consists of the battery/UC and the DC-DC converter. Output from the plant system, the battery/UC voltage and current will be measured and used as the input to the controller system. This closed-loop system is configured in Matlab/Simulink.

Generally, Simulink models are non-real-time simulation models, which may not be configured directly for hardware-in-the-loop simulations. To bridge the gap between a non-real-time simulation and a hardware experiment, a real-time simulation platform is built using xPC Target [129]. An xPC Target real-time system consists of a host computer and a target computer. The non-real-time simulation model in the host computer is transformed into a real-time xPC Target model using Real-time workshop and MS Visual C++ [129], which generates code directly from

the Simulink model. The generated code is downloaded and deployed on the target computer over an Ethernet host-target link. As the target computer is booted using a high performance kernel, which requires very little memory and can be run in real-time, it enables the closed-loop system for real-time simulation.

5.2.1 Target Computer

Different target computers are compatible with the real-time application generated by the real-time workshop. Desktop PC, rack-mount or industrial PC, compact PCI, all-in-one embedded PC are all good candidates for the target computer. To determine an appropriate target computer for the real-time simulation platform, one needs to understand the environment constraints of the real-time application and other physical limitations. The typical environment constraints include the operating temperature, water and dust, mechanical vibration/shock and electromagnetic interference (EMI). The physical limitations include the physical dimensions and the PCI I/O board expandability. For the real-time simulation platform setup in the lab, a desktop computer is selected as the target computer which satisfy all the required environmental and physical constraints and have good performance-to-cost ratio. For in-vehicle use, a mobile real-time target machine can be used which can withstand high levels of shock, vibration, and electromagnetic noise.

5.2.2 Ethernet Connection Setup between the Host computer and the Target Computer

To setup a real-time simulation and testing platform, a connection between the host computer and the target computer is configured via Ethernet connection using

the *xpcexplr* tool. This tool is executed from the Matlab command line and used to define the network connection between the host computer and the target computer. The network can be a LAN, the Internet, or a direct connection using a crossover Ethernet cable. Both the host and target computers are connected to the network via Ethernet adapters using the TCP/IP protocol for communication. To configure the Ethernet connection between the host computer and the target computer, an Intel EXPI9301CT Gigabit CT PCI-e desktop adapter is used in target desktop computer, as shown in Fig. 5.7.

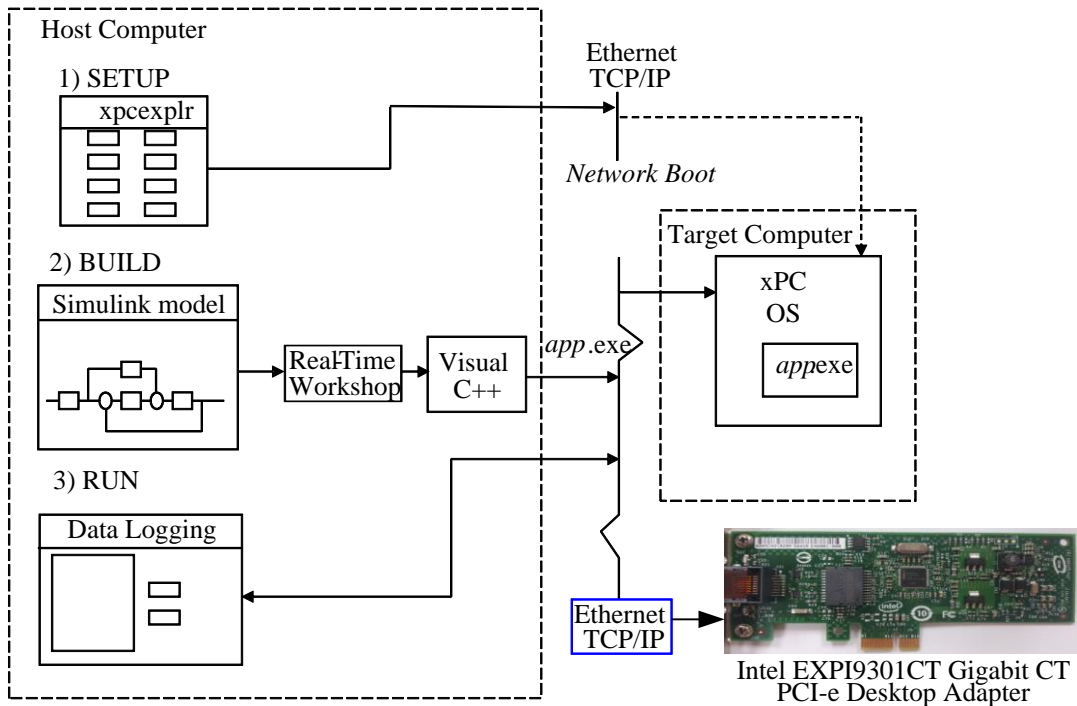


Figure 5.7 Configuration between the host computer and target computer.

In order to set up the Ethernet connections between the host computer and the target computer, this supported Ethernet card is plugged into a free PCI bus slot of the target computer. A static IP address is assigned to the target computer Ethernet card.

For example, the target computer IP address is set to:

IP address: 192.168.1.3

Port: 22222

Subnet mask: 255.255.255.0

With this PCI Ethernet adapter connected with the host computer via an Ethernet cable, the host-to-target communication hardware setup can be configured. In the host computer, the controller and/or the plant system is developed. The developed Simulink model is used to generate C code. The generated C code is then downloaded to the target computer for real-time simulation.

5.3 Real-Time Experiment Platform Setup

To mimic the real system, where a real-time controller and the physical system would communicate through an I/O bus with the hardware, the Simulink controller models are modified by adding I/O driver blocks to interface with the prototype hardware or even the actual plant hardware. The I/O driver blocks in the Simulink model are provided by the xPC Target. The xPC Target supports a wide range of third-party I/O boards. In this work, a National Instrument DAQ board PCI-6070E is used as the I/O board for signal and data acquisition [130]. With this DAQ board installed in the PCI slot, the target computer can be connected to a physical system as shown in Fig. 5.8.

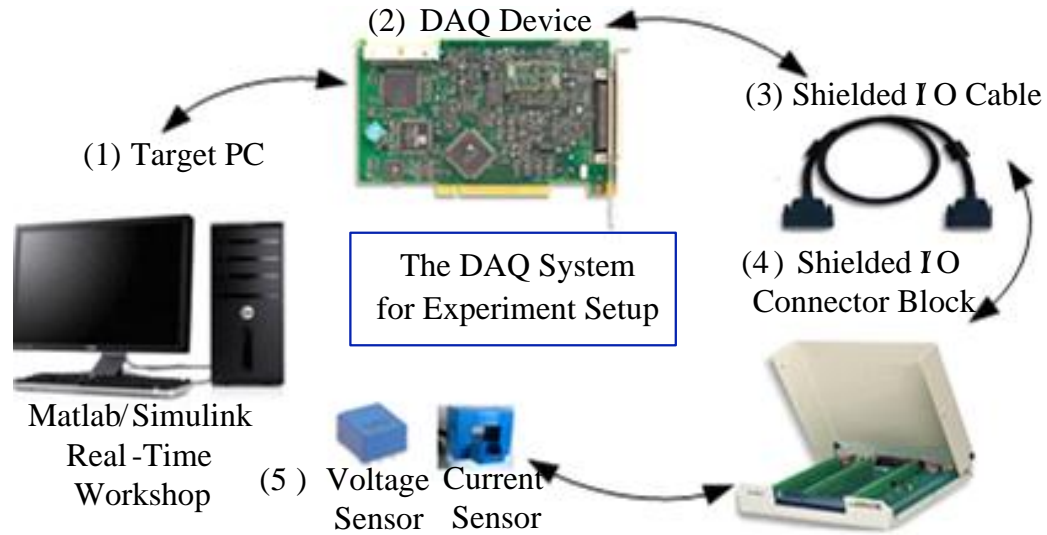


Figure 5.8 The DAQ system for target computer.

As most sensors and transducers require signal conditioning before a computer-based measurement system acquires the signal, a shielded I/O connector block is used as the I/O terminals. The signal conditioning system may include functions as signal amplification, filtering, electrical isolation, etc. A shielded I/O cable is used to connect the DAQ board with the I/O terminal block. Equipped with this DAQ system, the target computer can communicate via the I/O terminals by generating/receiving analog and digital signals.

The selected DAQ components are listed in Table 5.2.

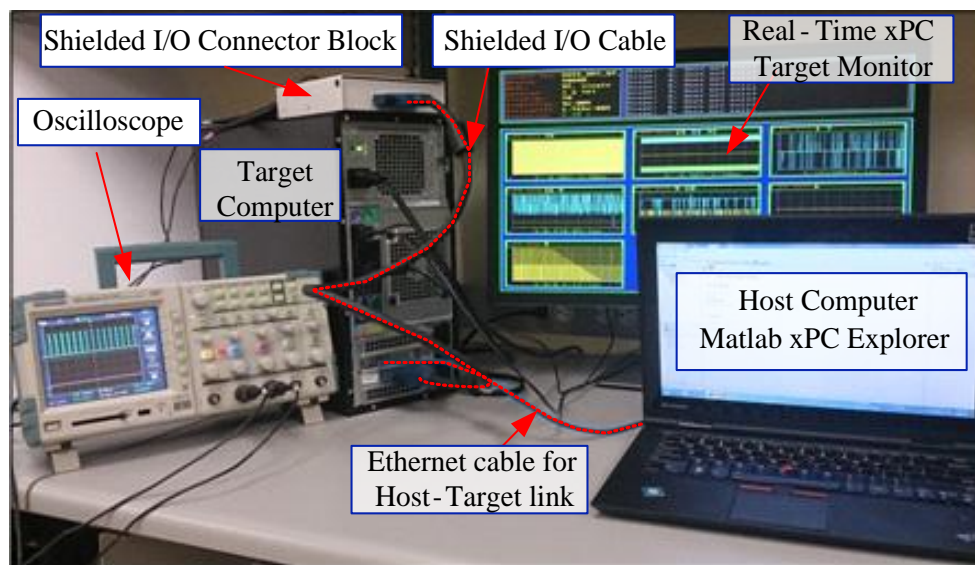
Table 5.2 DAQ components.

Function	Device
DAQ Card	NI PCI-6070E
Shielded I/O Cable	SH68-68-EP Shielded Cable

With the target computer set up for real-time simulation and the DAQ system configured for physical signal exchange, the real-time experiment system is prepared as shown in Fig. 5.8 (a).

5.4 Battery-UC Hybrid Energy Storage System Hardware Prototype Design

This hardware prototype system consists of a battery pack, an UC pack, a DC-DC converter and a DC electric load which mimics the function of a propulsion machine in a real EV. This physical system is shown in Fig. 5.9 (b).



(a)

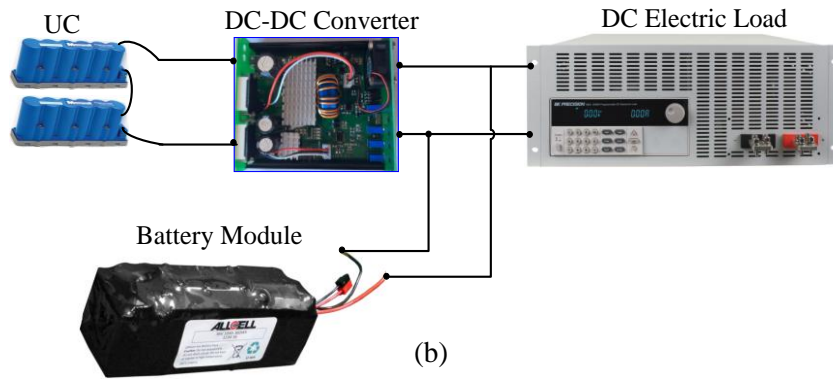


Figure 5.9 (a) The real-time experiment platform. (b) The battery-UC hybrid energy storage system for experiment test.

5.4.1 DC Electronic Load

A 8526 model of the DC electronic load from BK Precision is used in this work [131]. This 8500 series DC electronic load has wide operating ranges up to 500V and 120A. The DC electronic load can operate in constant current (CC), constant voltage (CV), constant resistance (CR) or constant power (CP) mode while the current, voltage, resistance and power values are set, measured and displayed in real-time.

In this work, the DC electronic load is used in the constant current (CC) mode. Thus, the load will sink a current based on the programmed current value regardless of the input voltage. The CC mode can be used for load regulation test of DC power supplies or for characterizing the discharge profile of a battery or a battery-UC HESS.

In this work, a USB to TTL serial interface between a personal computer and the DC electronic load is enabled in order to remotely control the DC electronic load for real-time load demand variation. An IT-E132 isolated communication cable is used to

set up this USB to TTL serial interface. A PV8500 software from BK Precision is used to remotely control the DC electronic load and set the operation modes [131].

5.4.2 DC-DC Converter Hardware

The DC-DC converter is used to interface the UC pack with the DC electronic load. Given the operating voltage of the UC pack and the battery module, the input/output voltage of the DC-DC converter can be set. In the experiment, the DC-DC converter specifications is selected in order to satisfy the test requirement. The DC-DC converter specifications are listed in Table 5.3.

Table 5.3 DC-DC Converter Specifications.

Parameter	Value	Unit
Input Voltage	2.8-80	[V]
Output Voltage	1.3-80	[V]
Maximum Inductor Current	26	[A]
Operating Frequency	120	[kHz]

A high performance LT8705 buck-boost switching regulator controller is integrated in the DC-DC converter which enables wide operation voltage range and provides input or output current monitor and limit. This high performance controller is also compatible with most solar, automotive, telecom and battery-powered systems [122].

5.4.2.1. Inductor Selection

The DC-DC converter works using inductor current mode control. The peak of the inductor current is sensed across a sensing resistor. With this sensing resistor R_{sense} , the DC-DC converter input-output power relationship is derived considering the inductor current ripple ΔI_L in Eq. (5.2),

$$V_{in} \left(\frac{V_{Rsense}}{R_{sense}} - \frac{1}{2} \Delta I_L \right) \cong V_{out} I_{out} \quad (5.2)$$

Here, the V_{in} and V_{out} are the DC-DC converter input and output voltage. V_{Rsense} is the sensing voltage of the inductor current. In this DC-DC converter, a high accuracy 3mOhm sensing resistor is used to sense the inductor current.

An inductor is used in the DC-DC converter. A small value inductor will result in increased current ripples and thus, due to the limited peak inductor current, decreases the maximum average current that can be provided to the load, especially in boost operation region. In order to provide adequate load current at low input voltage in boost operation region, the minimum inductance value is given by Eq. (5.3),

$$L_{min} = \frac{V_{in,min} D_{boost,max}}{f_{sw} \Delta I_{L,max}} \quad (5.3)$$

The maximum inductor ripple current can be derived based on Eq. (5.2) as,

$$\Delta I_{L,max} = 2 \left(\frac{V_{Rsense,max}}{R_{sense}} - \frac{I_{out,max} V_{out}}{V_{in,min}} \right) \quad (5.4)$$

Substitute Eq. (5.4) into Eq. (5.3), the minimum inductance value can be obtained as in Eq. (5.5).

$$L_{\min} = \frac{V_{in,\min} D_{boost,\max}}{2f_{sw} \left(\frac{V_{Rsense,\max}}{R_{sense}} - \frac{I_{out,\max} V_{out}}{V_{in,\min}} \right)} \quad (5.5)$$

Here, $D_{boost,\max} = 79\%$ is the maximum duty cycle percentage in boost operation for this DC-DC converter based on the input/output voltage relationship. $f_{sw} = 120\text{kHz}$ is the switching frequency. The maximum inductor current sense voltage value of $V_{Rsense,\max} = 85\text{mV}$ is obtained based on the typical performance characteristics of the maximum inductor current sense voltage graph given in the DC-DC converter product application note [132]. $R_{sense} = 3\text{m}\Omega$ is the inductor current sensing resistor. Based on the calculation, the minimum inductance value is obtained as $3.1 \mu\text{H}$.

Another consideration in the inductor selection is that the inductor must have a current rating greater than its peak operating current to prevent the inductor saturation, which will result in efficiency loss. The peak inductor current can be derived based on Eq. (5.6),

$$I_{L,\max} \cong I_{out,\max} \frac{V_{out}}{V_{in,\min}} + \left(\frac{V_{in,\min} D_{boost,\max}}{2Lf_{sw}} \right) \quad (5.6)$$

Based on Eq.(5.6), the inductor current rating of at least 25 A should be satisfied given an inductance at $22\mu\text{H}$. For high frequency application, it is important to choose an inductor with low core loss. In addition, the inductor is required to have low DC resistance to reduce the I^2R losses during high current operation. In order to reduce the radiated noise, ferrite, pot core or shielded bobbin inductor is suggested [132]. In this work, a $22\mu\text{H}$ ferrite core inductor with a current rating over 26A is used.

5.4.2.2. Power MOSFET Specifications

It is very important to consider the power dissipation in the power MOSFET selection. The power MOSFET with high power dissipation will impact the DC-DC converter power efficiency. Thus, it is critical to limit the power dissipation to avoid overheating which may even damage the devices.

In this work, the power MOSFET IPP023NE7N3 from Infineon Technology Inc. is used. This power MOSFET features as ideal for high frequency switching and DC-DC converter application. The specification of the MOSFET is provided in Table 5.4.

Table 5.4 Power MOSFET specifications.

Parameter	Symbol	Value	Unit
Breakdown voltage	$V_{BR,DSS}$	75	[V]
Threshold voltage	$V_{GS,th}$	3.1	[V]
Continuous drain current	I_D	20	[A]
Pulsed drain current	$I_{D,pulse}$	480	[kg]
Switch on-state resistance	R_{on}	2.1	[m Ω]
MOSFET output capacitance	C_{oss}	2420	[pF]
Reverse recovery charge	Q_{rr}	129	[nC]
Reverse recovery time	t_{rr}	72	[ns]
Gate charge	Q_t	155	[nC]

MOSFET rise time	t_r	26	[ns]
MOSFET fall time	t_f	22	[ns]

5.4.2.3. *Cin and Cout Selection*

For DC-DC converter design, the input and output capacitance is necessary to reduce the voltage ripple of the input and output voltage.

Ceramic capacitors should be placed near the regulator input and output to suppress high frequency switching spikes. Ceramic capacitors are selected because of their low ESR (equivalent series resistance) characteristics, which can reduce the input voltage ripples and help reduce the power losses in comparison to the higher ESR bulk capacitors. In order to achieve high capacitance and low ESR, a parallel combination of the capacitors is typically used.

In this work, a bank of three $1\mu\text{F}$ capacitors are connected in parallel with an $820\mu\text{F}$ polarized capacitor as the input capacitor network.

The output capacitance is used to suppress the output voltage ripples caused by the ripple in the output and the load currents. Similar to the input capacitance selection, a parallel combination of multiple capacitors are placed near the output pin. In this work, a bank of three $1\mu\text{F}$ capacitors are connected in parallel with two $820\mu\text{F}$ polarized capacitors as the output capacitor network.

5.4.3 DC-DC Converter Control Technique

DC-DC converters are widely used in power electronics. Various DC-DC converter control techniques are discussed in literature [133], including the voltage

mode control, current model control, PID (proportional-integral-derivative) control, sliding mode control, etc. Among which, the voltage mode control and the current mode control techniques have been widely adopted by industry.

The voltage mode control technique regulates the DC-DC converter output voltage and maintain a constant or fixed output voltage regardless of the load current or input voltage. On the other hand, a current mode controller regulates the converter current directly. The most popular method in the current mode control is the fixed frequency peak current mode control [134]. In this method, the peak inductor current is regulated using a control reference.

Fig. 5.10 shows the schematic of a DC-DC converter with current mode control in boost operation region.

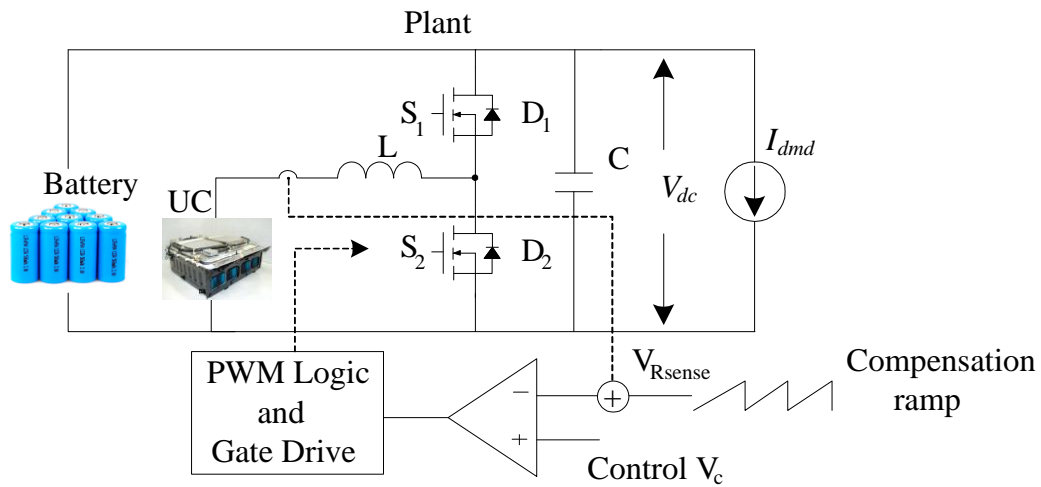


Figure 5.10 The DC-DC converter with current mode control.

As shown in Fig. 5.10, this current mode controller regulates the peak inductor current with a control signal V_c . A compensating ramp is added to the inductor current

sense signal $V_{R_{sense}}$ to provide slope compensation, which improves stability in constant frequency current mode control architectures by preventing subharmonic oscillations, especially at high duty cycles [134].

In this work, a current mode control based switching regulator controller LT8705 is used. The control reference signal V_c is generated based on the input/output current monitor circuits. The input current monitor and regulation circuit is shown in Fig. 5.11.

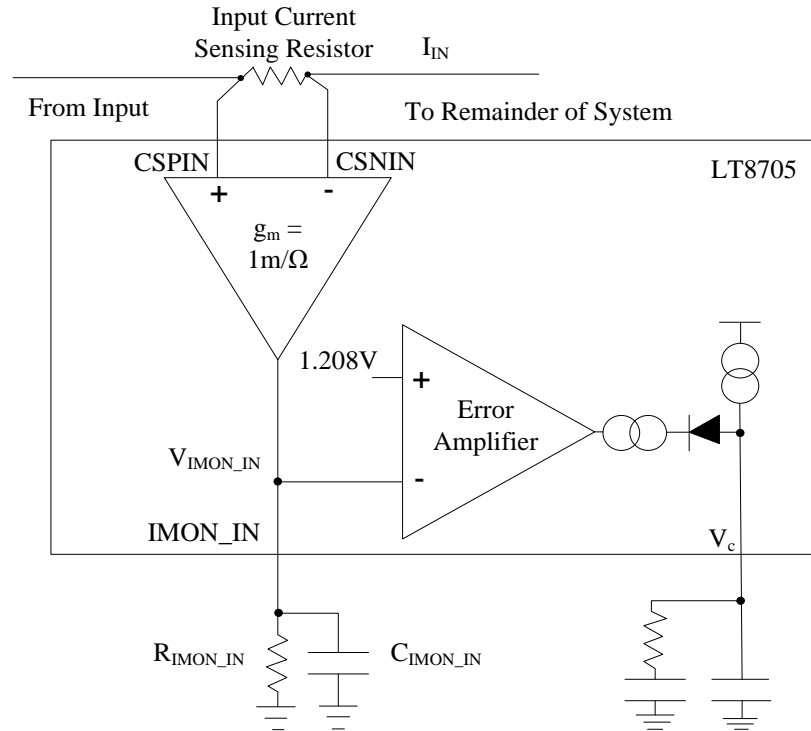


Figure 5.11 The input current monitor and regulation circuit in the controller [132].

The input current I_{IN} is sensed through a 3mOhm sensing resistor R_{sense1} which develops a voltage across the CSPIN and CSNIN pins in the LT8705 controller chip. This voltage across CSPIN and CSNIN is converted to a current by multiplying

1mA/V. This current is flowing out the pin IMON_IN and into the resistor R_{IMON_IN} . The resulting voltage over the resistor R_{IMON_IN} is derived as,

$$V_{IMON_IN} = (I_{IN} R_{SENSE1} \cdot 1mA / V) R_{IMON_IN} \quad (5.7)$$

This voltage is proportional to the input current of the DC-DC converter. As shown in Fig. 5.11, when this voltage V_{IMON_IN} is greater than 1.208V, it causes the V_c voltage to reduce; when the voltage V_{IMON_IN} is smaller than 1.208V, it causes the V_c voltage to increase therefore regulates the inductor and input currents [132].

The relationship between the input current reference and the resistor value of R_{IMON_IN} is given in Eq. (5.8),

$$I_{in,ref} = \frac{1.208V}{R_{SENSE1} \cdot 1mA / V \cdot R_{IMON_IN}} \quad (5.8)$$

The range of the resistance value R_{IMON_IN} can be determined based on the input current range. If the maximum input current is set to 25A, the minimum value of R_{IMON_IN} should be 16.1kOhm. In this work, the R_{IMON_IN} resistor is selected to be the sum of a fixed 18kOhm and a digital potentiometer with the maximum value of 500kOhm. The fixed 18kOhm is used for current limiting and protection. The digital potentiometer is used to set the input current reference. For a given input current reference, the digital potentiometer resistance value in the unit of [kOhm] is given in Eq. (5.9).

$$R_{dp} = \begin{cases} \frac{1.208V}{R_{SENSE1} I_{in,ref}} - 18, & 0.08A \leq I_{in,ref} \leq 20A \\ 500, & 0 \leq I_{in,ref} < 0.08A \end{cases} \quad (5.9)$$

Therefore, the DC-DC converter current control is implemented by setting different values of the digital potentiometer. The design and implementation details are explained in Section 5.4.4.

5.4.4 Interface between the Real-Time Controller and DC-DC Converter

The DC-DC converter current mode control technique is explained in Section 5.4.3. The DC-DC converter input current can be regulated based on a given current reference. To set the DC-DC converter input current reference, the resistance of the resistor R_{IMON_IN} is varied accordingly. To vary the resistance of R_{IMON_IN} , a digital potentiometer with a resistance value in the range of 0 to 500kOhm is set by the real-time supervisory controller.

In this work, an AD5235 digital potentiometer from Analog Devices Inc., is utilized [135] and directly connected to the R_{IMON_IN} with the DC-DC converter regulator controller, as shown in Fig. 5.11. This AD5235 dual channel digitally controlled potentiometer with 1024 step resolution can provide enhanced resolution in comparison to the mechanical potentiometer. In each channel, the maximum nominal resistance is 250kOhm. By connecting the two channels in series, a nominal resistance of 500kOhm is obtained.

The digital potentiometer resistance value is determined by the position of the wiper. The position of the wiper is directly controlled by a scratchpad RDAC register. This scratchpad RDAC register can load values via a Serial Peripheral Interface (SPI) compatible serial interface, which allows the adjustment of the resistance value of the potentiometer. For example, if the scratchpad RDAC register loads all 0s, the digital

potentiometer value is set to 0 Ohm. If the register value is set to all 1s, the digital potentiometer will output the maximum nominal resistance value, which gives 500 kOhm as the sum of two channel resistance. To implement the SPI communication, an Arduino Uno board is employed to send the serial data input to the digital potentiometer.

To configure the interface between the real-time controller and the digital potentiometer, the real-time controller computes the input current reference based on the supervisory energy management control strategy. The computed input current reference is translated into an analog voltage value within 0 to 5V. This analog voltage value is then used to set the digital potentiometer resistance value via the SPI interface. The analog voltage reference value can be computed as Eq. (5.10),

$$V_{ref} = \begin{cases} \frac{1.208V \cdot (0.01)}{R_{SENSE1} I_{in,ref}} - 0.18, & 0.08A \leq I_{in,ref} \leq 20A \\ 5, & 0 \leq I_{in,ref} < 0.08A \end{cases} \quad (5.10)$$

Notice that, when the current reference $I_{in,ref}$ value is smaller than 0.08A, the analog voltage reference value should be limited with the maximum of 5V for device safety considerations. This analog voltage reference is then output through the DAQ system to the Arduino Uno board. By reading this analog voltage reference, the Arduino Uno board converts the analog voltage value into a serial data input to the scratchpad RDAC register of the digital potentiometer. The resistance of the digital potentiometer R_{dp} is generated as a function of the analog voltage value as Eq. (5.11),

$$R_{dp} = V_{ref} \cdot 10^2 \text{ kOhm} / V \quad (5.11)$$

The resistance value of R_{IMON_IN} is the sum of R_{dp} and a fixed 18kOhm. With the resistance value of R_{IMON_IN} set by the supervisory energy management control strategy, the DC-DC converter input current can be regulated based on the reference current according to Eq. (5.8).

The control interface between the target computer and the hardware prototype is shown in Fig. 5.12.

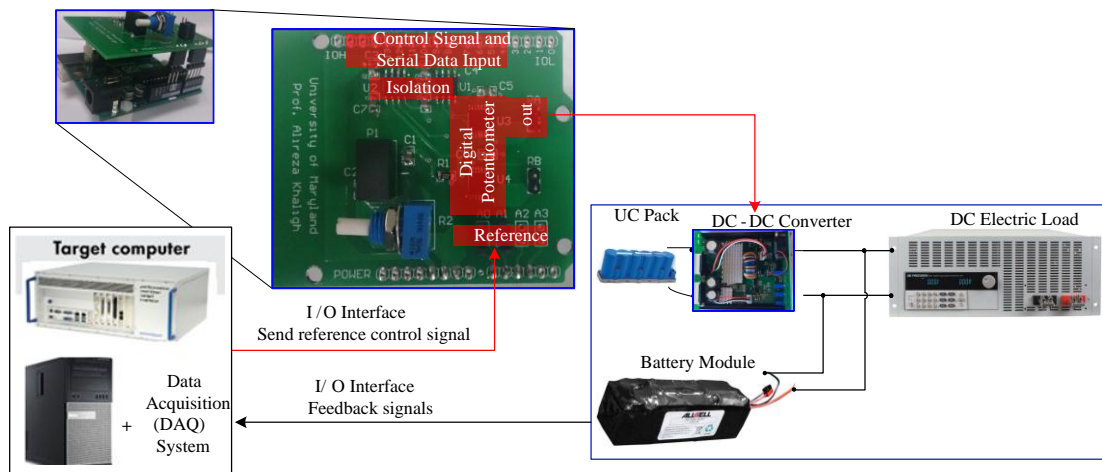


Figure 5.12 The control interface between the target computer and the hardware prototype.

5.4.5 Sensor Network and DAQ Configuration

For a closed-loop experiment platform, the sensor network with proper current sensors and voltage sensors should be configured in order to provide feedback signals to the real-time controller system.

In the battery-UC HESS, two voltage sensors are required to monitor the voltages of the battery module and the UC module to ensure that both energy storage components are working under allowed operation ranges. In addition, two current

sensors are used to monitor the UC current, the battery current. The current sensors and the voltage sensors convert the measurements into a proportional analog voltage signals within the range of 10V. These feedback analog voltage signals are taken to the DAQ analog input channels through the shielded I/O connector block terminals. Therefore, the sensor feedback signals are read into the target computer as inputs to the real-time controller system.

Different supervisory energy management control strategies may require different input signals (feedback) from the hardware plant system. Based on the real-time controller requirements, the sensor network can be flexibly configured.

5.4.5 Experiment Setup

The major components and their specifications in this experimental platform are summarized in Table 5.5.

Table 5.5 The Experiment Test Components.

Name	Model Description
BK Precision 8526 Programmable DC load	Maximum operation at 500V and 120A.
DAQ system	National Instrument PCI-6070E DAQ card, SH68-68-EP shielded cable and SCB-68 terminal block.
Host computer	A Personal laptop.
Target Computer	Lab desktop with Intel(R) Core i7-2640M CPU@2.80GHz and 8GB RAM.

5.5 Experiment Results

The performance of the real-time energy management strategy [105] are tested using standard drive cycles including the ECE drive cycle, New York City drive cycle, and highway driving (HWFET) drive cycle.

The 195-second ECE urban drive cycle captures the low to median speed drive and stop-and-go features in one test cycle. Although the dynamics of this ECE drive cycle is low, it is quite representative for the urban driving scenarios. The New York City drive cycle also features low speed urban driving with more frequent stops, which represents a congested urban driving situations. As a supplemental test, HWFET drive cycle is developed to test vehicles at high speeds and high accelerations during aggressive highway driving conditions. The speed profiles of these three test drive cycles are displayed in Fig. 5.13.

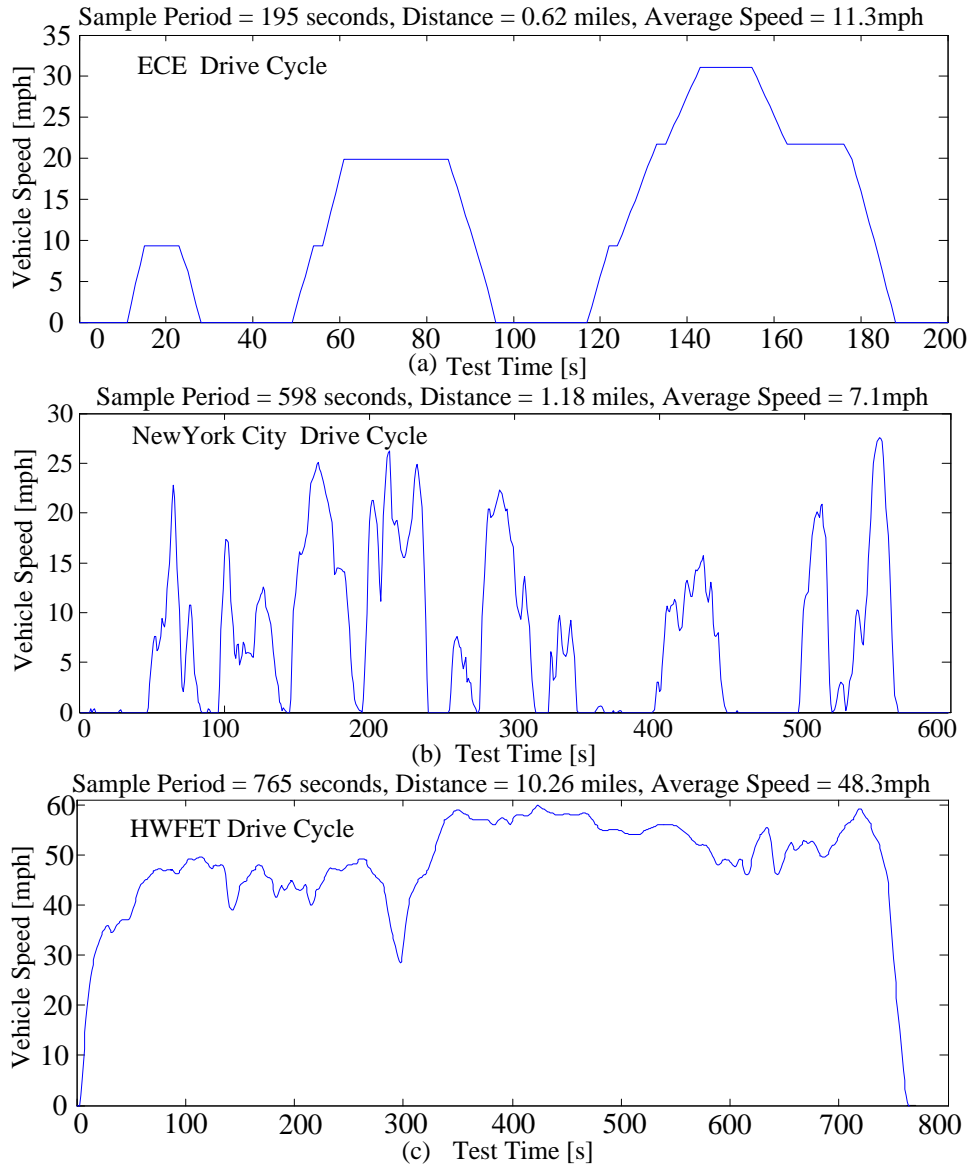


Figure 5.13 The test drive cycles. (a) ECE drive cycle; (b) New York City drive cycle; (c) HWFET drive cycle.

The demand power of these test drive cycles in simulation is downscaled proportionally considering the power rating and energy storage downscaling factor of the battery-UC HESS hardware prototype. The demand current of these test drive cycles are given in Fig. 5.14.

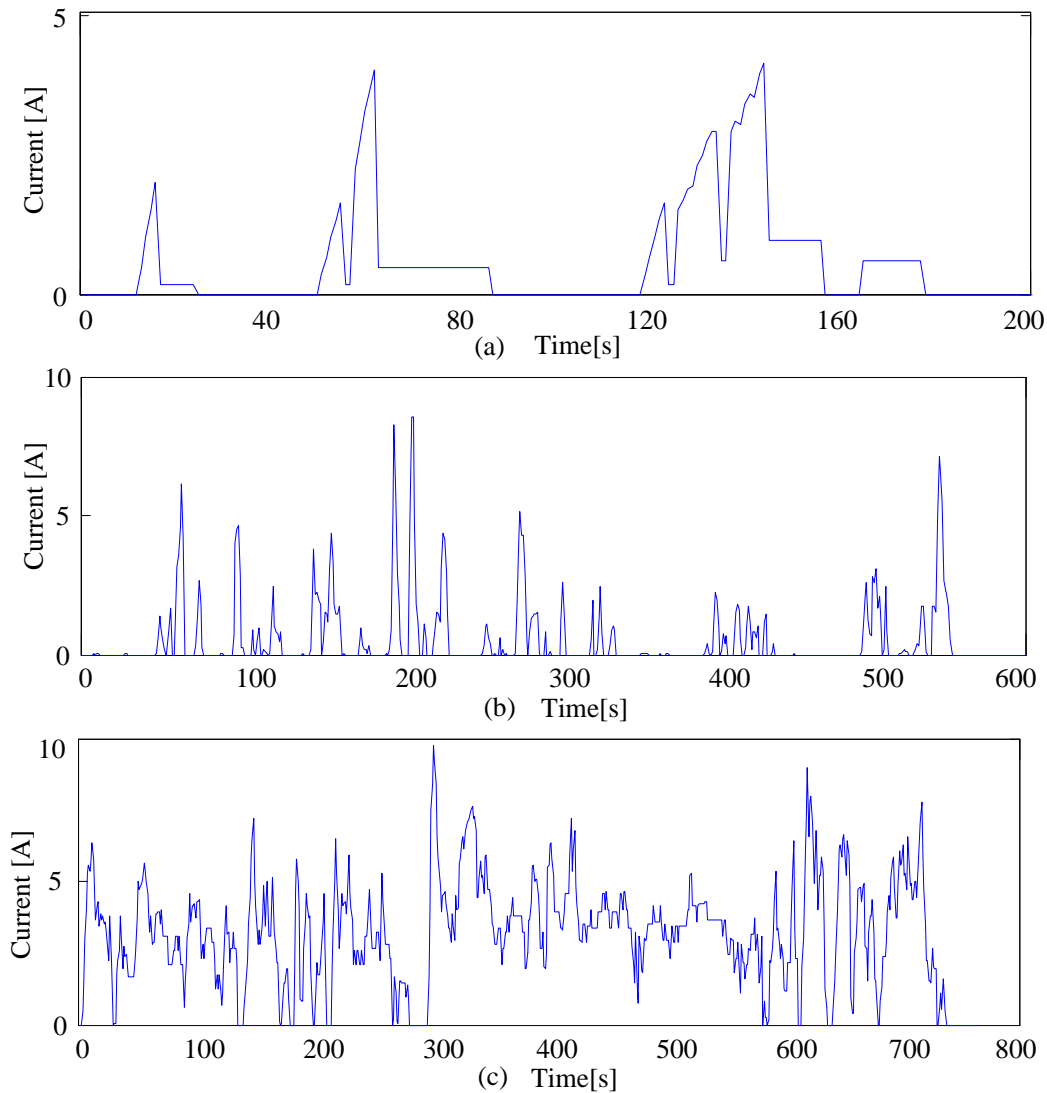


Figure 5.14 The demand current based on the test drive cycles. (a) ECE drive cycle; (b) New York City drive cycle; (c) HWFET drive cycle.

In this experiment test, the built hardware prototype is tested without considering regenerative braking, as the programmable electronic load does not have sourcing features. Under this driving condition, the real-time energy management controllers sustain the charge in both battery and UC packs and provide robust response to the load dynamics. The developed real-time energy management strategy is tested using

the developed experimental platform to validate the real-time implementation feasibility and effectiveness. The experiment results of the battery voltage/current and the UC voltage/current are presented in Fig. 5.15 to Fig. 5.17.

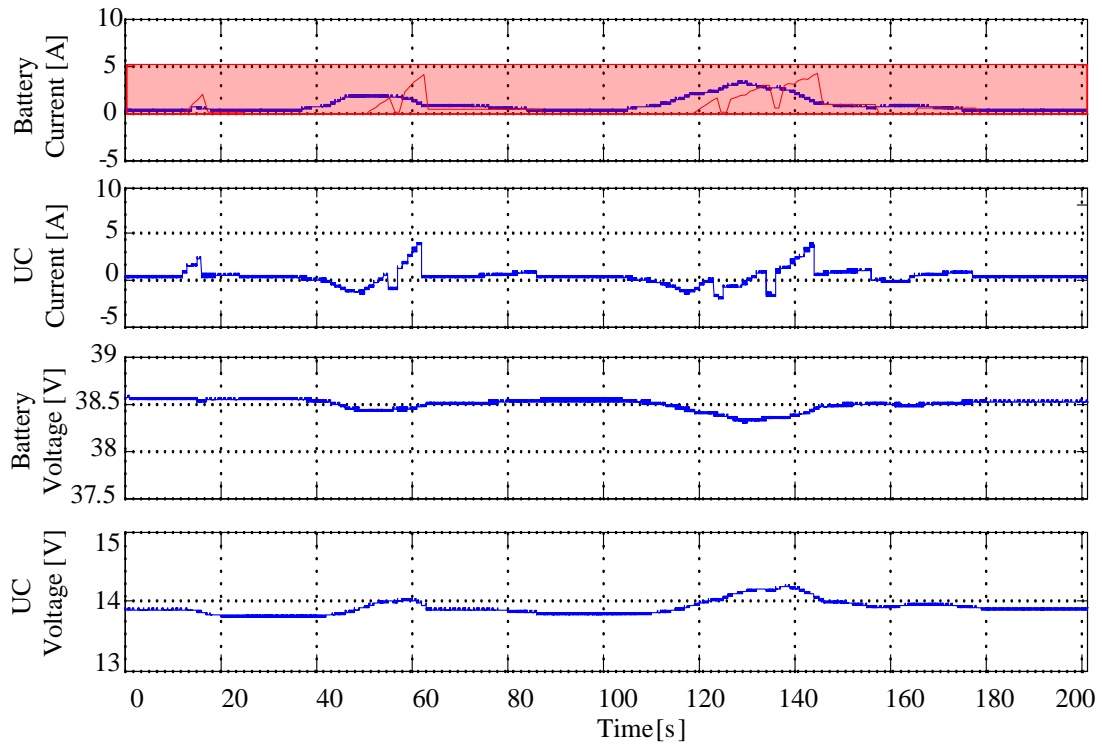


Figure 5.15 The real-time experiment results under ECE drive cycle. The redline shows the load current.

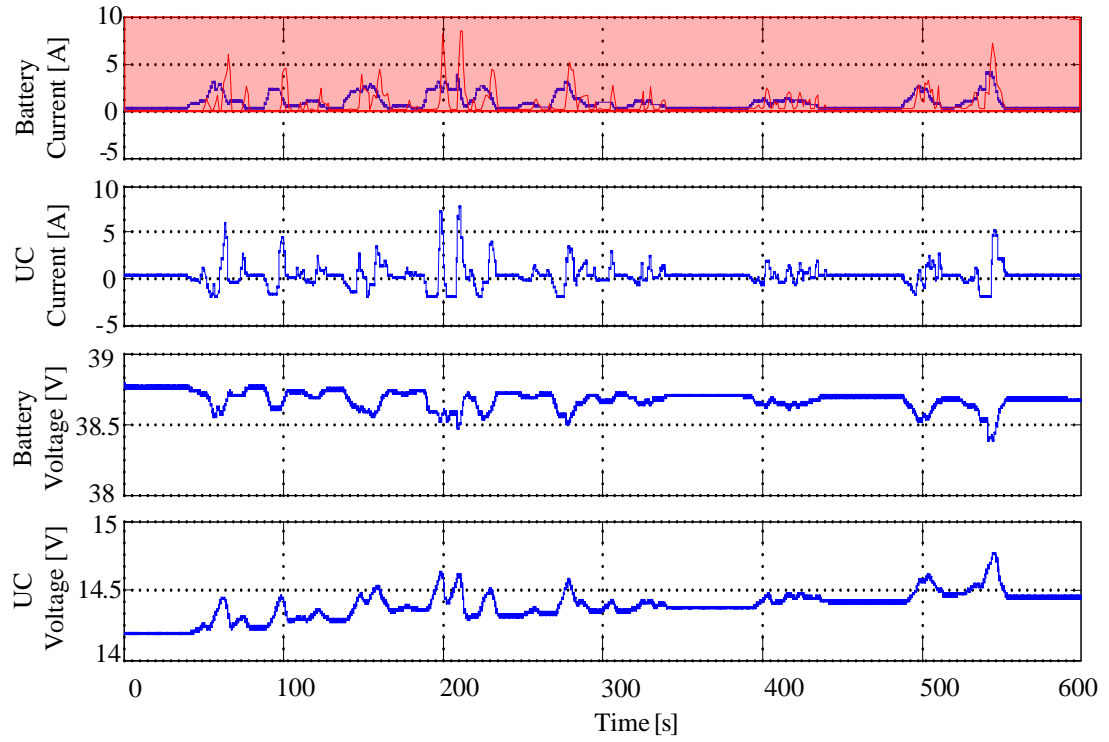


Figure 5.16 The real-time experiment results under New York City drive cycle. The redline shows the load current.

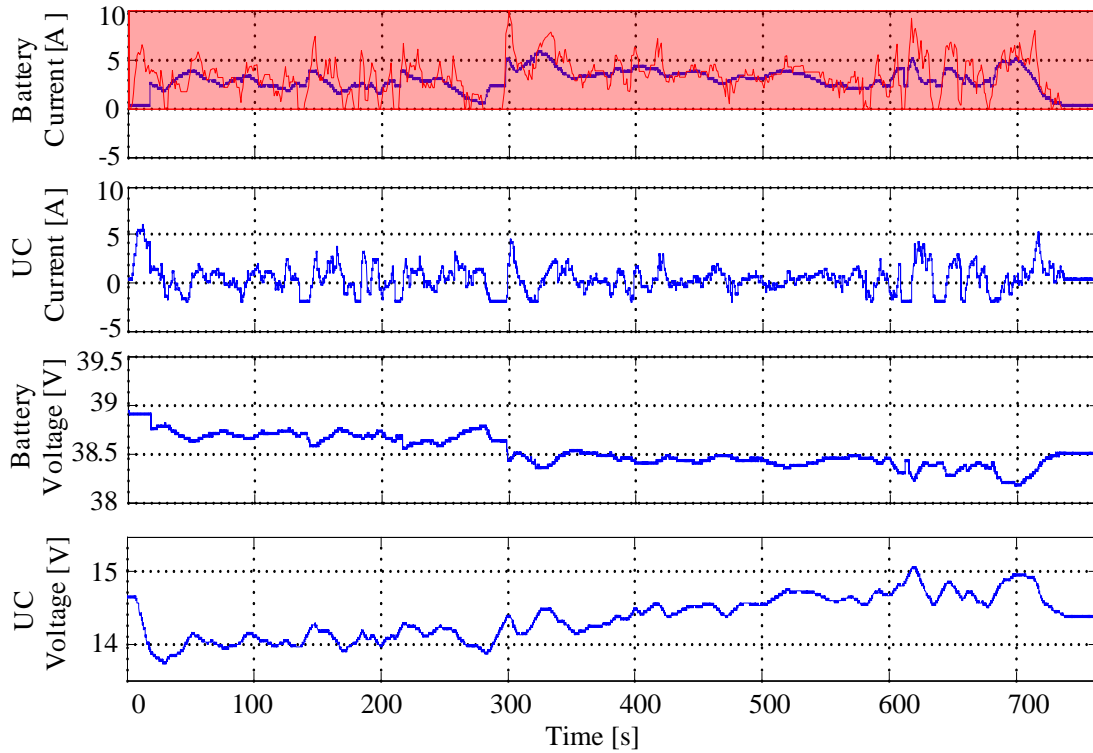


Figure 5.17 The real-time experiment results under HWFET drive cycle. The redline shows the load current.

The proposed real-time energy management strategy presents its robust control capability to precharge the UC for the future high current peak, which can improve the DC-DC converter power efficiency as the input voltage is increased. The experiment results reveal that the DC-DC converter operates under high average efficiency over 95% and the overall HESS system efficiency is at 94.2% evaluated based on Eq. (4.17). The experiment result shows that the real-time energy management control strategy have greatly reduced the battery current magnitude for peak shaving by over 50%. The battery current smoothing effect achieved by the proposed energy management control strategy is also appealing. It can be observed

that the battery is protected from the aggressive transient demand due to its relatively slow dynamics. Instead, the UC delivers the remaining current with fast response to satisfy the transient demand.

5.6 Summary

This chapter presents the work on hardware prototype design and real-time experiment implementations. A real-time experiment platform and a data acquisition system is constructed and integrated. A scaled-down hardware prototype, including the battery pack, UC pack and a DC-DC converter, is developed to validate the proposed control strategies using the proposed platform. This platform provides a dual computer real-time environment that is cost-effective, reliable and practical for the validation of the proposed real-time control strategy for a battery-UC HESS prototype. Using this real-time experiment platform, the proposed supervisory energy management control strategy is tested to validate its real-time implementation feasibility and effectiveness. The hardware experiment is performed under scaled standard drive cycles to capture the performance of the battery-UC HESS for EV applications. The experiment results are presented, which shows effective implementation of the proposed real-time energy management strategy. It is concluded that the proposed real-time energy management strategy exhibits excellent performance and high robustness with different driving scenarios.

Chapter 6: Conclusions and Future Work

6.1 Conclusions

EVs face significant energy storage related challenges, including the range anxiety, high cost, and battery degradation. Batteries, as the energy storage components in majority of current and upcoming EVs, deliver energy to the electric machine during propulsion and recover energy during regenerative braking. During urban drive cycles with frequent stop-and-go, the frequent high power exchange between the electric machine and the ESS results in accelerated battery aging. The battery aging decreases the battery capability of storing energy and providing power over the battery lifetime. One potential solution to this problem is to integrate high-energy density batteries with high-power density UCs as a battery-UC HESS.

In this work, a systematic approach is presented to the energy management problem of battery-UC HESS for EVs. This energy management problem encompasses multiple energy storage resource planning and sizing, power distribution and an effective hardware design for the real-time system implementation. This complex and multidisciplinary problem of the battery-UC HESS development is decomposed into four stages. In the first stage, a comprehensive review of the previous and ongoing research in this area is provided to present an in-depth investigation of the state-of-the-art of the battery-UC HESS design, especially for vehicular applications. Following this comprehensive review in Chapter 2, the sizing of the battery-UC HESS and the system integration issues have been discussed in Chapter 3. In this stage, the sizing design demonstrates the combination of a high

energy density battery pack and a UC pack that can achieve a smaller size and weight in comparison to a high power density battery counterpart. Primarily, the challenges in this battery-UC HESS lies in the energy management between the battery pack and the UC pack, determining the power split and establishing methods to interface the two energy storage devices. In this stage, a real-time energy management supervisory controller is developed and described in Chapter 4, which provides a new perspective to the battery-UC HESS energy management problem. After a thorough exploration of the battery/UC technologies, the system integration and the energy management strategies, we develop and implement the hardware prototype of a scaled-down battery-UC HESS and perform experimental test and empirical validation of the energy management controller in the final stage.

The major contributions of this dissertation are as follows.

First, we formulate a battery-UC sizing problem and take into account the interdependence between sizing and energy management. In this sizing analysis, the trade-off between sizing and EV specifications are analyzed.

Second, we formulate an optimization problem for the battery-UC HESS energy management problem to improve the system efficiency and extend the battery lifetime. To solve this problem, a combined DP and NN method is proposed for real-time energy management. In addition, the battery SoH under realistic driving scenarios is evaluated. This provides a performance measure for real-time EV energy management strategies.

Last, we address the complete implementation process of a working system of the battery-UC HESS hardware prototype and the real-time energy management

controller. This demonstrates a complete structured framework for the battery-UC HESS design, sizing, control and hardware implementations, which provides a foundation for continuing hybrid energy storage research.

The focus of this work was to address one of the main challenges in the EV energy storage system by developing and implementing a battery-UC HESS that can potentially provide reliable operation for over 10 years. With extended battery lifetime and without substantially increasing the system weight/cost, the battery-UC HESS has potential to improve the EV performance, lower the energy storage system life time cost and potentially facilitate the mass adoption of EVs. Furthermore, the proposed real-time experiment platform provides a cost-effective method for energy management controller prototyping, validation and verification. This helps us to explore the energy management controller design and to fully exploit the advantages of the battery-UC HESS, which will result in fundamental improvement in the hybrid energy storage research and EV system power-energy-weight tradeoffs.

6.2 Future Work

Developing an online, optimized and real-time implementable battery-UC HESS for vehicular application is challenging and several problems need to be addressed for its effectiveness and practicality.

First, a more accurate battery SoC estimation can be incorporated into the battery management system (BMS). To improve the accuracy of the SoC estimation, a separate parameter estimation frame along with the thermal models can be developed to account the battery parameter variations under different operation conditions. A

more precise battery SoC gauge can provide more accurate driving range estimation for the vehicle driver.

Second, in this work the battery-UC HESS is developed and tested as a stand-alone component. The next step can be to implement this battery-UC HESS into a scaled EV powertrain system by interfacing the battery-UC HESS with inverters and electric machines. Furthermore, various EV powertrain architectures can be explored as shown in Fig. 6.1. In Fig. 6.1(a), the battery-UC HESS is connected with one inverter and one electric machine for a simple and basic EV powertrain topology. In more complex systems as shown in Fig. 6.1(b) and Fig. 6.1(c), the dual electric machine powertrain architectures are proposed to enhance the propulsion efficiency [136]. The dual electric machine architecture is composed of two propulsion machines with complimentary torque-speed efficiency maps, and coupled either using a torque coupler, or installed on the same shaft. In the case of using a torque coupler, the torques generated by the two propulsion machines are added. In the case of using same shaft architectures, the two propulsion machines rotate at the same angular frequency. The individual inverters control these two machines. The supervisory controller generates the power references for the inverters, such that the two propulsion machines operate at their corresponding highest efficiencies. The supervisory controller also gives control commands to the battery-UC HESS to optimally split the power demand between the battery and UC pack to effectively prolong the battery lifetime.

In the future work, the complete EV powertrain can be developed to provide substantial groundwork for the EV research and development.

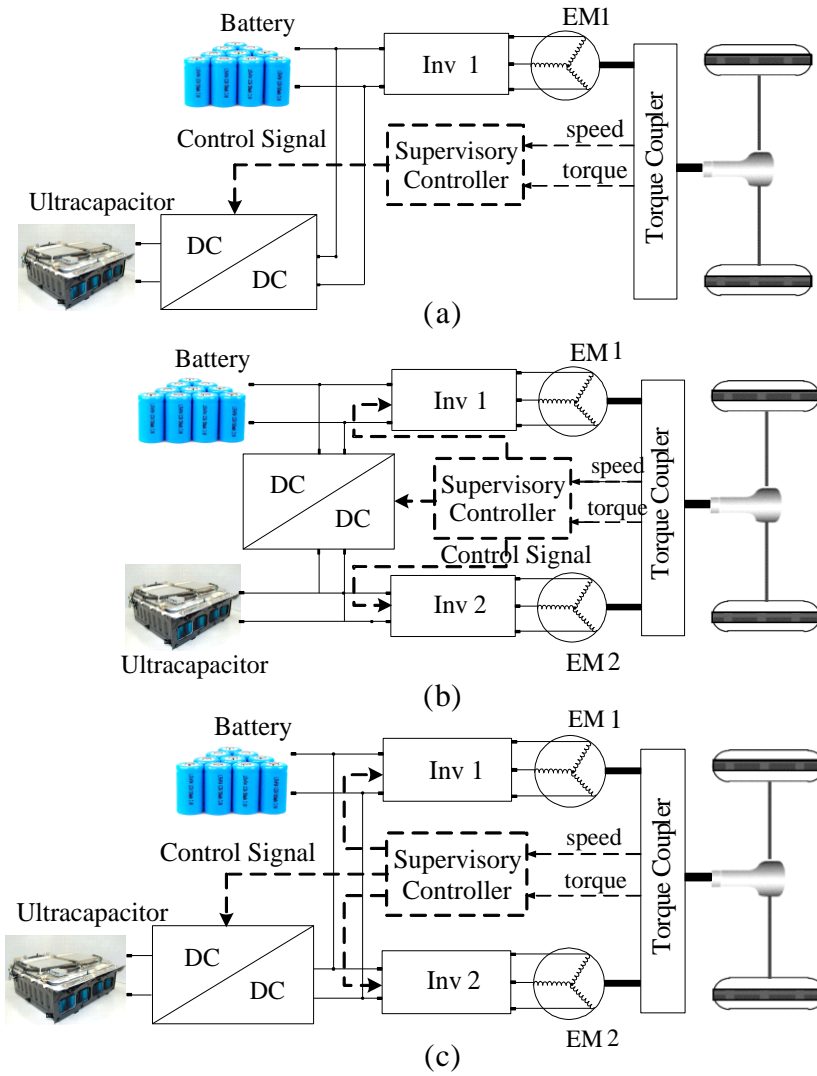


Figure 6.1 The potential EV powertrain architectures.

Bibliography

- [1] Department of Energy, "The History of the Electric Car," 15 September 2014. [Online]. Available: <http://energy.gov/articles/history-electric-car>.
- [2] D. Block, J. Harrison and P. Brooker, "Electric Vehicle Sales for 2014 and Future Projections," Electric Vehicle Transportation Center, Mar., 2015.
- [3] Electric Drive Transportation Association(EDTA) , "Electric Drive Sales Dashboard," Feb 2016. [Online]. Available: <http://electricdrive.org/ht/d/sp/i/20952/pid/20952>.
- [4] K. T. Chau and C. C. Chan, Modern electric vehicle technology, Oxford science publications., 2001.
- [5] M. Ehsani, Y. Gao and A. Emadi, Modern electric, hybrid electric, and fuel cell vehicles: fundamentals, theory, and design, CRC press., 2009.
- [6] A. Khaligh and Z. Li, "Battery, Ultracapacitor, Fuel Cell, and Hybrid Energy Storage Systems for Electric, Hybrid Electric, Fuel Cell, and Plug-In Hybrid Electric Vehicles: State of the Art," *IEEE Transactions on Vehicular Technology*, vol. 59, no. 6, p. 2806–2814, July 2010.
- [7] "All-Electric Vehicles (EVs)," 2015. [Online]. Available: <http://fueleconomy.gov/feg/evtech.shtml#end-notes>.
- [8] H. J. Chae, W. Y. Kim, S. Y. Yun, Y. S. Jeong, J. Y. Lee and H. T. Moon, "3.3 kW on board charger for electric vehicle.," in *IEEE 8th International Conference on Power Electronics and ECCE Asia (ICPE & ECCE)*,, 2011.
- [9] D. S. Gautam, F. Musavi, M. Edington, W. Eberle and W. G. Dunford, "An automotive onboard 3.3-kW battery charger for PHEV application," *IEEE Transactions on Vehicular Technology*, vol. 61, no. 8, pp. 3466-3474, 2012.

- [10] M. Miller, A. Holmes, B. Conlon and P. Savagian, "The GM "Voltec" 4ET50 Multi-Mode Electric Transaxle," *SAE Int. J. Engines*, vol. 4, no. 1, pp. 1102-1114, 2011.
- [11] S. Rogers, "Electric Drive Status and Challenges," Department of Energy, 2012.
- [12] J. M. Miller, "Energy storage technology markets and application's: Ultracapacitors in combination with Lithium-ion," in *IEEE 7th International Conference on Power Electronics*, 2007.
- [13] A. C. Baisden and A. Emadi, "ADVISOR-based model of a battery and an ultra-capacitor energy source for hybrid electric vehicles," *IEEE Transactions on Vehicular Technology* ., vol. 53, no. 1, pp. 199-205, 2004.
- [14] S. G. Chalk and J. F. Miller, "Key challenges and recent progress in batteries, fuel cells, and hydrogen storage for clean energy systems," *Journal of Power Sources*, vol. 159, no. 1, pp. 73-80, 2006.
- [15] A. S. J1772, "SAE Electric Vehicle and Plug in Hybrid Electric Vehicle Conductive Charge Coupler," 2011.
- [16] S. Dusmez, A. Cook and A. Khaligh, "Comprehensive analysis of high quality power converters for level 3 off-board chargers," in *IEEE Vehicle Power and Propulsion Conference (VPPC)*, 2011.
- [17] D. Anderson, Status and trends in the HEV/PHEV/EV battery industry, Rocky Mountain Institute, 2008.
- [18] D. Anderson, An evaluation of current and future costs for lithium-ion batterie for use in electrified vehicle powertrains, Duke University, April 2009.
- [19] H. H. Hussein and I. Batarseh, "An overview of generic battery models," in *IEEE Power and Energy Society General Meeting*, 2011.

- [20] USABC, "Electric Vehicle Battery Test Procedures Manual, Revision 2," Department of Energy / ID-10479, 1996.
- [21] A. Burke, "Ultracapacitor technologies and application in hybrid and electric vehicles," *International Journal of Energy Research*, vol. 34, no. 2, pp. 133-151, 2009.
- [22] M. Armand and J. M. Tarascon, "Building better batteries," *Nature*, vol. 451, pp. 652-657, 2008.
- [23] "Battery Calendar Life Estimator Manual Revision 1: Modeling and Simulation," US Department of Energy Vehicle Technologies Program, Oct. 2012.
- [24] A. Burke, "Ultracapacitor technologies and application in hybrid and electric vehicles," *International Journal of Energy Research*, vol. 34, no. 2, pp. 133-151, 2010.
- [25] J. M. Miller, P. J. McCleer, M. Everett and E. G. Strangas, "Ultracapacitor Plus Battery Energy Storage System Sizing Methodology for HEV Power Split Electronic CVT's," in *IEEE International Symposium on Industrial Electronics*, 2005.
- [26] J. M. Miller, "Electrical and thermal performance of the carbon-carbon ultracapacitor under constant power conditions," in *IEEE Vehicle Power and Propulsion Conference*, 2007.
- [27] J. M. Miller, "Energy storage system technology challenges facing strong hybrid, plug-in and battery electric vehicles.," in *IEEE Vehicle Power and Propulsion Conference*, 2009.
- [28] J. M. Miller, U. Deshpande, T. J. Dougherty and T. Bohn, "Power electronic enabled active hybrid energy storage system and its economic viability," in *IEEE Applied Power Electronics Conference and Exposition*, , 2009.

- [29] J. M. Miller, T. Bohn, T. J. Dougherty and U. Deshpande, "Why hybridization of energy storage is essential for future hybrid, plug-in and battery electric vehicles.," in *IEEE Energy Conversion Congress and Exposition*, 2009.
- [30] J. M. Miller and G. Sartorelli, "Battery and ultracapacitor combinations—Where should the converter go?," in *IEEE Vehicle Power and Propulsion Conference (VPPC)*, 2010.
- [31] A. W. Stienecker, T. Stuart and C. Ashtiani, "A combined ultracapacitor-lead acid battery storage system for mild hybrid electric vehicles.," in *IEEE Vehicle Power and Propulsion Conference*, 2005.
- [32] S. M. Lukic, S. G. Wirasingha, F. Rodriguez, J. Cao and A. Emadi, "Power management of an ultracapacitor/battery hybrid energy storage system in an HEV," in *IEEE Vehicle Power and Propulsion Conference*, 2006.
- [33] S. M. Lukic, J. Cao, R. C. Bansal, F. Rodríguez and A. Emadi, "Energy storage systems for automotive applications," *IEEE Transactions on Industrial electronics*, vol. 55, no. 6, pp. 2258-2267, 2008.
- [34] J. Cao and A. Emadi, " A new battery/ultracapacitor hybrid energy storage system for electric, hybrid, and plug-in hybrid electric vehicles," *IEEE Transactions on Power Electronics* , vol. 27, no. 1, pp. 122-132, 2012.
- [35] M. Zolot and B. Kramer, "Hybrid Energy Storage Studies Using Batteries and Ultracapacitors for Advanced Vehicles," in *12th International Seminar on Double Layer Capacitors and Similar Energy Storage Devices*, Deerfield Beach, FL, December, 2002.
- [36] S. K. Kim and S. H. Choi, "Development of Fuel Cell Hybrid Vehicle by Using Ultra-Capacitors as a Secondary Power Source," *SAE Technical Paper*, 2005.
- [37] M. Ortúzar, J. Moreno and J. Dixon, "Ultracapacitor-based auxiliary energy system for an electric vehicle: Implementation and evaluation.," *IEEE*

Transactions on Industrial Electronics, vol. 54, no. 4, pp. 2147-2156, 2007.

- [38] A. Khaligh, A. Miraoui and D. Garret, "Guest editorial: Special section," *IEEE Transactions on Vehicular Technology*, vol. 58, no. 8, p. 3879–3881, Oct. 2009..
- [39] L. Gao, R. A. Dougal and S. Liu, "Power enhancement of an actively controlled battery/ultracapacitor hybrid," *IEEE Transactions on Power Electronics*, vol. 20, no. 1, p. 236–243, Jan., 2005.
- [40] W. Lhomme, P. Delarue, P. Barrade, A. Bouscayrol and A. Rufer, "Design and control of a supercapacitor storage system for traction applications," in *IEEE 14th IAS Annual Meeting on Industry Applications Conference*, 2005.
- [41] R. M. Schupbach and J. C. Balda, "The role of ultracapacitors in an energy storage unit for vehicle power management," in *IEEE 58th Vehicular Technology Conference*, 2003.
- [42] J. Moreno, M. E. Ortúzar and L. W. Dixon, "Energy-management system for a hybrid electric vehicle, using ultracapacitors and neural networks.," *IEEE Transactions on Industrial Electronics*, vol. 53, no. 2, pp. 614-623, 2006.
- [43] J. B. Cao and B. G. Cao, "Neural network sliding mode control based on on-line identification for electric vehicle with ultracapacitor-battery hybrid power," *International Journal of Control Automation and Systems*, vol. 7, no. 3, pp. 409-418, 2009.
- [44] Z. Li, O. Onar, A. Khaligh and E. Schaltz, " Design, control, and power management of a battery/ultra-capacitor hybrid system for small electric vehicles," *SAE Technical Paper.*, 2009.
- [45] L. Solero, A. Lidozzi and J. A. Pomilio, "Design of multiple-input power converter for hybrid vehicles," *IEEE Transactions on Power Electronics*, vol. 20, no. 5, p. 1007–1016, Sep. 2005..

- [46] C. Romaus, J. Bocker, K. Witting, A. Seifried and O. Znamenshchykov, "Optimal energy management for a hybrid energy storage system combining batteries and double layer capacitors," in *IEEE Energy Conversion Congress and Exposition*, 2009.
- [47] R. Halvgaard, "Model Predictive Control for Smart Energy Systems," Technical University of Denmark, 2014.
- [48] Z. Li, O. Onar, A. Khaligh and E. Schaltz, "Design and control of a multiple input dc/dc converter for battery/ultra-capacitor based electric vehicle power system,," in *IEEE 24th Applied Power Electronics Conference and Exposition*, Feb. 2009.
- [49] B. G. Dobbs and P. L. Chapman, "A multiple-input DC-DC converter topology," *IEEE Power Electronics Letters*, vol. 1, no. 1, pp. 6-9, 2003.
- [50] J. Bauman and M. Kazerani, "A comparative study of fuel-cell–battery, fuel-cell–ultracapacitor, and fuel-cell–battery–ultracapacitor vehicles.," *IEEE Transactions on Vehicular Technology*, vol. 57, no. 2, pp. 760-769, 2008.
- [51] A. Ravey, R. Roche, B. Blunier and A. Miraoui, "Combined optimal sizing and energy management of hybrid electric vehicles," in *IEEE Transportation Electrification Conference and Expo (ITEC)*, Dearborn, MI, 2012.
- [52] R. de Castro, C. Pinto, R. E. Araujo, P. Melo and D. Freitas, "Optimal sizing and energy management of hybrid storage systems," in *IEEE Vehicle Power and Propulsion Conference (VPPC)*, Seoul, Korea, 2012.
- [53] R. M. Schupbach, J. C. Balda, M. Zolot and B. Kramer, "Design methodology of a combined battery-ultracapacitor energy storage unit for vehicle power management," in *IEEE 34th Annual In Power Electronics Specialist Conference*, 2003.
- [54] E. Schaltz, A. Khaligh and P. O. Rasmussen, " Influence of

- battery/ultracapacitor energy-storage sizing on battery lifetime in a fuel cell hybrid electric vehicle," *IEEE Transactions on Vehicular Technology*, vol. 58, no. 8, pp. 3882-3891, 2009.
- [55] J. Lopes, J. A. Pomilio and P. A. V. Ferreira, "Optimal sizing of batteries and ultracapacitors for fuel cell electric vehicles," in *IEEE 37th Annual Conference on Industrial Electronics Society*, Nov., 2011.
- [56] R. Esteves Araujo, R. de Castro, C. Pinto, P. Melo and D. Freitas, "Combined Sizing and Energy Management in EVs With Batteries and Supercapacitors," *IEEE Transactions on Vehicular Technology*, vol. 63, no. 7, pp. 3062-3076, 2014.
- [57] A. Ravey, N. Watrin, B. Blunier, D. Bouquain and A. Miraoui, "Energy-Source-Sizing Methodology for Hybrid Fuel Cell Vehicles Based on Statistical Description of Driving Cycles," *IEEE Transactions on Vehicular Technology*, vol. 60, no. 9, pp. 4164-4174, Nov., 2011.
- [58] N. Jalil, N. A. Kheir and M. Salman, "A rule-based energy management strategy for a series hybrid vehicle," in *IEEE American Control Conference*, 1997.
- [59] H. Banvait, S. Anwar and Y. Chen, "A rule-based energy management strategy for plug-in hybrid electric vehicle (PHEV)," in *American Control Conference*, 2009.
- [60] R. Carter, A. Cruden and P. Hall, "Optimizing for efficiency or battery life in a battery/supercapacitor electric vehicle," *IEEE Transactions on Vehicular Technology*, vol. 61, no. 4, p. 1526–1533, May, 2012.
- [61] J. J. Awerbuch and C. R. Sullivan, "Filter-based power splitting in ultracapacitor-battery hybrids for vehicular applications," in *IEEE 12th Workshop on Control and Modeling for Power Electronics (COMPEL)*, June,

2010..

- [62] J. Shen, S. Dusmez and A. Khaligh, "Optimization of Sizing and Battery Cycle Life in Battery/UC Hybrid Energy Storage System for Electric Vehicle Applications," *IEEE Transactions on Industrial Informatics*, vol. 10, no. 4, pp. 2112-2121, 2014.
- [63] C. C. Lin, J. M. Kang, J. W. Grizzle and H. Peng, "Energy management strategy for a parallel hybrid electric truck," in *IEEE American Control Conference*,, 2001.
- [64] M. Salman, J. S. Niels and A. K. Naim, "Control strategies for parallel hybrid vehicles," in *IEEE American Control Conference*, Chicago, Illinois, 2000.
- [65] D. Gao, Z. Jin and Q. Lu, "Energy management strategy based on fuzzy logic for a fuel cell hybrid bus," *Journal of Power Sources*, vol. 185, no. 1, pp. 311-317, 2008.
- [66] A. A. Ferreira, J. A. Pomilio, G. Spiazzi and L. de Araujo Silva, "Energy management fuzzy logic supervisory for electric vehicle power supplies system," *IEEE Transactions on Power Electronics*, vol. 23, no. 1, pp. 107-115, 2008.
- [67] H. Hannoun, D. Diallo and C. Marchand, "Energy Management Strategy for a Parallel Hybrid Electric Vehicle Using Fuzzy Logic," in *IEEE International Symposium on Power Electronics, Electrical Drives, Automation and Motion*, 2006.
- [68] S. Dusmez and A. Khaligh, "A Supervisory Power Splitting Approach for a New Ultracapacitor-Battery Vehicle Deploying Two Propulsion Machines," *IEEE Transactions on Industrial Informatics*, vol. 10, no. 3, pp. 1960-1971, August, 2014.
- [69] S. G. Li, S. M. Sharkh, W. F. C. and C. N. Zhang, "Energy and battery

- management of a plug-in series hybrid electric vehicle using fuzzy logic," *IEEE Transactions on Vehicular Technology*, vol. 60, no. 8, pp. 3571-3585, 2011.
- [70] G. Wang, P. Yang and J. Zhang, "Fuzzy optimal control and simulation of battery-ultracapacitor dual-energy source storage system for pure electric vehicle," in *IEEE International Conference on Intelligent Control and Information Processing (ICICIP)*, August, 2010.
- [71] E. D. Tate and S. P. Boyd, "Finding ultimate limits of performance for hybrid electric vehicles," *SAE Paper 00FTT-50*, 1998.
- [72] D. P. Bertsekas, *Dynamic programming and optimal control* (Vol. 1, No. 2), Belmont, MA: Athena Scientific, 1995.
- [73] S. D. Cairano, W. Liang, I. V. Kolmanovsky, M. L. Kuang and A. M. Phillips, "Power smoothing energy management and its application to a series hybrid powertrain," *IEEE Transactions on Control Systems Technology*, vol. 21, no. 6, p. 2091–2103, 2012.
- [74] Y. Kim, S. Mohan, N. A. Samad, J. B. Siegel and A. G. Stefanopoulou, "Optimal power management for a series hybrid electric vehicle cognizant of battery mechanical effects," in *IEEE American Control Conference (ACC)*, June, 2014.
- [75] I. Kolmanovsky, S. Sivashankar and J. Sun, "Optimal control-based powertrain feasibility assessment: A software implementation perspective," in *IEEE American Control Conference*, June, 2005.
- [76] B. Wu, C. C. Lin, Z. Filipi, H. Peng and D. Assanis, "Optimization of power management strategies for a hydraulic hybrid medium truck," in *Proceedings of the 2002 Advanced vehicle control conference*, Sept., 2002.
- [77] C. C. Lin, H. Peng, J. W. Grizzle and J. M. Kang, "Power management strategy for a parallel hybrid electric truck," *IEEE Transactions on Control Systems*

Technology, vol. 11, no. 6, pp. 839-849, 2003.

- [78] M. Koot, J. T. Kessels, B. de Jager, W. P. M. H. Heemels, P. P. J. Van den Bosch and M. Steinbuch, "Energy management strategies for vehicular electric power systems," *IEEE Transactions on Vehicular Technology*, vol. 54, no. 3, pp. 771-782, 2005.
- [79] L. V. Pérez, G. R. Bossio, D. Moitre and G. O. García, "Optimization of power management in an hybrid electric vehicle using dynamic programming.," *Mathematics and Computers in Simulation*, vol. 73, no. 1, pp. 244-254, 2006.
- [80] A. Brahma, Y. Guezennec and G. Rizzoni., "Optimal energy management in series hybrid electric vehicles," in *IEEE American Control Conference*, 2000.
- [81] G. Q., L. Y. and P. Z., "Trip Based Power Management of Plug-in Hybrid Electric Vehicle with Two-Scale Dynamic Programming," in *IEEE Vehicle Power and Propulsion Conference*, Sept., 2007.
- [82] C. C. Lin, H. Peng and J. W. Grizzle, "A stochastic control strategy for hybrid electric vehicles," in *IEEE American Control Conference*, 2004.
- [83] I. Kolmanovsky, I. Siverguina and B. Lygoe, "Optimization of powertrain operating policy for feasibility assessment and calibration: Stochastic dynamic programming approach.," in *IEEE American Control Conference*, 2002.
- [84] P. Rutquist, "Optimal control for the energy storage in a hybrid electric vehicle.," in *19th International Battery, Hybrid and Fuel Cell Electric Vehicle Symposium and Exhibition (EVS19)*, 2002.
- [85] L. Johannesson, M. Asbogard and B. Egardt, "Assessing the potential of predictive control for hybrid vehicle powertrains using stochastic dynamic programming.," *IEEE Transactions on Intelligent Transportation Systems*, vol. 8, no. 1, pp. 71-83, 2007.

- [86] S. J. Moura, H. K. Fathy, D. S. Callaway and J. L. Stein, "A stochastic optimal control approach for power management in plug-in hybrid electric vehicles.," *IEEE Transactions on Control Systems Technology*, vol. 19, no. 3, pp. 545-555, 2011.
- [87] R. Kumar, A power management strategy for hybrid output coupled power-split transmission to minimize fuel consumption(Doctoral dissertation), Purdue University, 2010.
- [88] F. R. Salmasi, "Control strategies for hybrid electric vehicles: Evolution, classification, comparison, and future trends," *IEEE Transactions on Vehicular Technology*, vol. 56, no. 5, pp. 2393-2404, 2007.
- [89] T. Leroy, J. Malaizé and G. Corde, "Towards real-time optimal energy management of hev powertrains using stochastic dynamic programming," in *IEEE Vehicle Power and Propulsion Conference (VPPC)*, Seoul, Korea, Oct.,2012.
- [90] E. F. Camacho and C. B. Alba., *Model Predictive Control*, London: Springer, 2007.
- [91] J. Maciejowski, *Predictive control: with constraints.*, Predictive control: with constraints., 2002.
- [92] H. K. Wook and H. H. Soo, *Receding Horizon Control: Model Predictive Control for State Models*, Springer, 2005.
- [93] J. Shen and A. Khaligh, "Predictive Control of a Battery/Ultracapacitor Hybrid Energy Storage System in Electric Vehicles," in *IEEE Transportation Electrification Conference and Exposition*, Dearborn, MI., 2016.
- [94] H. Borhan, A. Vahidi, A. Phillips, M. Kuang and I. Kolmanovsky, "Predictive energy management of a power-split hybrid electric vehicle," in *American Control Conference*, St. Louis, MO, USA, 2009.

- [95] H. Borhan and A. Vahidi, "Model predictive control of a power-split Hybrid Electric Vehicle with combined battery and ultracapacitor energy storage," in *American Control Conference (ACC)*, Baltimore, MD, USA, 2010.
- [96] H. Borhan, C. Zhang, A. Vahidi, A. Phillips, M. Kuang and S. Di Cairano, "Nonlinear Model Predictive Control for power-split Hybrid Electric Vehicles," in *IEEE Conference on Decision and Control (CDC)*, Atlanta, GA, 2010.
- [97] A. Santucci, A. Sorniotti and C. Lekakou, "Model Predictive Control for the Power-Split between Supercapacitor and Battery for Automotive Applications,," in *IEEE International Electric Vehicle Conference (IEVC)*, Oct. 2013.
- [98] B. Hredzak, V. Agelidis and M. Jang, "A Model Predictive Control System for a Hybrid Battery-Ultracapacitor Power Source," *IEEE Transactions on Power Electronics*, vol. 29, no. 3, pp. 1469 - 1479, March, 2014.
- [99] M. Choi, J. Lee and S. Seo, "Real-time Optimization for Power Management Systems of a Battery/Supercapacitor Hybrid Energy Storage System in Electric Vehicles,," *IEEE Transactions on Vehicular Technology*, vol. 63, no. 8, pp. 3600-3611, Oct. 2014.
- [100] M. E. Choi and S. W. Seo, "Robust energy management of a battery/supercapacitor Hybrid Energy Storage System in an electric vehicle,," in *IEEE International Electric Vehicle Conference (IEVC)*, 2012.
- [101] M. E. Choi, S. W. Kim and S. W. Seo, "Energy management optimization in a battery/supercapacitor hybrid energy storage system," *IEEE Transactions on Smart Grid*, vol. 3, no. 1, pp. 463-472, 2012.
- [102] Y. L. Murphey, J. Park, Z. Chen, M. L. Kuang, M. A. Masrur and A. M. Phillips, "Intelligent hybrid vehicle power control—Part I: Machine learning of optimal vehicle power,," *IEEE Transactions on Vehicular Technology*, vol. 61,

no. 8, pp. 3519-3530, 2012.

- [103] Y. L. Murphey, J. Park, L. Kiliaris, M. L. Kuang, M. A. Masrur, A. M. Phillips and Q. Wang, "Intelligent Hybrid Vehicle Power Control—Part II: Online Intelligent Energy Management.," *IEEE Transactions on Vehicular Technology*, vol. 62, no. 1, pp. 69-79, 2013.
- [104] Z. Chen, C. Mi, J. Xu, X. Gong and C. You, "Energy management for a power-split plug-in hybrid electric vehicle based on dynamic programming and neural networks," *IEEE Transactions on Vehicular Technology*, vol. 63, no. 4, p. 1567–1580, May, 2014.
- [105] J. Shen and A. Khaligh, "A Supervisory Energy Management Control Strategy for a Battery/ Ultracapacitor Hybrid Energy Storage System," *IEEE Transactions on Transportation Electrification*, vol. 1, no. 3, pp. 223-231, Oct. 2015.
- [106] "Technical Datasheet of K2 Series Ultracapacitors," Maxwell Technologies Inc., 2013.
- [107] M. Grant, S. Boyd and Y. Ye, "CVX: Matlab software for disciplined convex programming," 2008.
- [108] S. Boyd and L. Vandenberghe, *Convex Optimization*, Cambridge University Press, 2004.
- [109] ArgonneNationalLaboratory, "Autonomie (Version 1.0), Computer Software," <http://www.autonomie.net>, Argonne, IL, 2009.
- [110] J. Shen, A. Hasanzadeh and A. Khaligh, "Optimal Power Split and Sizing of Hybrid Energy Storage System for Electric Vehicles," in *IEEE Transportation Electrification Conference and Expo*, Dearborn, MI, June 2014.
- [111] R. W. Erickson and D.Maksimovic, *Fundamentals of power electronics*, Springer Science & Business Media, 2001.

- [112] Mathworks, "Neural Networks Toolbox: User's Guide (R2012b)," 2012.
- [113] A. Fadel and Z. Biao, "An experimental and analytical comparison study of power management methodologies of fuel cell–battery hybrid vehicles," *Journal of Power Sources*, vol. 196, no. 6, pp. 3271-3279., 2011.
- [114] A. Sciarretta, L. Serrao, P. C. Dewangan, P. Tona, E. Bergshoeff, C. Bordons and L. Charmpa., "A control benchmark on the energy management of a plug-in hybrid electric vehicle," *Control Engineering Practice*, vol. 29, pp. 287-298, 2014.
- [115] J. Shen, S. Dusmez and A. Khaligh, "An Electro-Thermal Cycle-Lifetime Estimation Model for LiFePO₄ Batteries," in *IEEE Transportation Electrification Conference and Expo*, Dearborn, MI, 2013.
- [116] W. Waag, C. Fleischer and D. U. Sauer, "Critical review of the methods for monitoring of lithium-ion batteries in electric and hybrid vehicles," *Journal of Power Sources* , vol. 258 , pp. 321-339, 2014.
- [117] J. Wang, P. Liu, J. Hicks-Garner, E. Sherman, S. Soukiazian, M. Verbrugge, H. Tataria, J. Musser and P. Finamore, "Cycle-life model for graphite-LiFePO₄ cells," *Journal of Power Sources*, vol. 196, no. 8, p. 3942–3948, 2011.
- [118] H. J. Ploehn, P. Ramadass and R. E. White, "Solvent diffusion model for aging of lithium-ion battery cells," *Journal of The Electrochemical Society* , vol. 151, no. 3, pp. A456-A462, 2004.
- [119] M. Safari, M. Morcrette, A. Teysot and C. Delacourt, "Multimodal physics-based aging model for life prediction of li-ion batteries," *Journal of The Electrochemical Society*, vol. 156, no. 3, pp. A145-A153, 2009.
- [120] I. Bloom, B. Cole, J. Sohn, S. Jones, E. Polzin, V. Battaglia, G. Henriksen, C. Motloch, R. Richardson, T. Unkelhaeuser, D. Ingersoll and H. Case, "An accelerated calendar and cycle life study of Li-ion cells," *Journal of Power*

Sources, vol. 101, no. 2, pp. 238-247, Oct., 2001..

- [121] P. Ramadass, B. Haran, P. Gomadam, R. White and B. Popov, "Development of first principles capacity fade model for Li-ion cells," *Journal of the Electrochemical Society*, vol. 151, no. 2, pp. 196-203, 2004.
- [122] R. Spotnitz, "Simulation of capacity fade in lithium-ion batteries," *Journal of Power Sources*, vol. 113, no. 1, pp. 72-80, Jan., 2003..
- [123] M. Dubarry, V. Svoboda, R. Hwu and B. Liaw, "Capacity Loss in Rechargeable Lithium Cells During Cycle Life Testing: The Importance of Determining State Of Charge," *Journal of Power Sources*, vol. 174, no. 2, pp. 1121-1125, 2007.
- [124] S. Ebbesen, P. Elbert and L. Guzzella, "Battery state-of-health perceptive energy management for hybrid electric vehicles," *IEEE Transactions on Vehicular Technology*, vol. 61, no. 7, p. 2893–2900, Sept. 2012.
- [125] K. Smith, M. Earleywine, E. Wood, J. Neubauer and A. Pesaran, "Comparison of plug-in hybrid electric vehicle battery life across geographies and drive cycles," *SAE Technical Paper*, Vols. No. 2012-01-0666, 2012.
- [126] D. U. Sauer and H. Wenzl, "Comparison of different approaches for lifetime prediction of electrochemical systems using lead-acid batteries as example," *Journal of Power Sources*, vol. 176, no. 2, p. 534–546, 2008.
- [127] "Autonomie (Version 1.0), Computer Software, Argonne, IL, 2009, <http://www.autonomie.net>," Argonne National Laboratory.
- [128] P. Sharer, R. Aymeric, N. Paul and S. Pagerit, "Vehicle simulation results for plug-in HEV battery requirements," Argonne National Laboratory, 2006.
- [129] "xPC Target For Use with the Real-Time Workshop," The Mathworks Inc., Nov. 2000.
- [130] National Instruments, "NI 6070E/6071E Family Specifications," 2003.

- [131] BK Precision, "User Manual:8500 Series DC Electronic Loads," 2009.
- [132] Linear Technology, "80V VIN and VOUT Synchronous 4-Switch Buck-Boost DC/DC Controller," LinearTechnology, Milpitas, 2013.
- [133] S. Verma, S. K. Singh and A. G. Rao, "Overview of control Techniques for DC-DC converters," *Research Journal of Engineering Sciences*, no. ISSN 2278 (2013): 9472, 2013.
- [134] S. Lee, "Practical Feedback Loop Analysis for Current-Mode Boost Converter," Texas Instruments, Jan. 2014.
- [135] Analog Devices Inc., "Nonvolatile Memory, Dual 1024-Position Digital Potentiometer," 2012.
- [136] H. Yavasoglu, J. Shen, C. Shi and A. Khaligh, "Power Split Control Strategy for An EV Powertrain with Two Propulsion Machines," *IEEE Transaction on Transportation Electrification*, vol. 1, no. 4, pp. 382-390, Dec. 2015.